Chapter One
Introduction

1.1. Epidemiology of Brain Tumors:

Primary tumours of the central nervous system (CNS) are relatively uncommon, accounting for only 2% of cancer deaths. However, the effect on the individual with a primary CNS tumour is frequently devastating, and brain tumours lead, on average, to a greater loss of life per patient than any other adult tumour. Primary CNS tumours affect patients of all ages, from childhood to old age, with a rising incidence from middle age onwards. In childhood, they are the commonest solid tumours (as opposed to leukaemias). The overall annual incidence is around 7 per 100 000 population, giving approximately 4400 people newly diagnosed with a brain tumour in the UK each year. (Symonds et.al (2012)).

An incidence of the brain tumors according to its tissue type as; an adult primary CNS tumors: 30–35% meningioma, 20% GBM, 10% pituitary, 10% nerve sheath, 5% low-grade glioma, <5% anaplastic astrocytoma, <5% primary CNS lymphoma. Of adult gliomas, ~80% are high-grade and ~20% are low-grade. Children: 20% of all pediatric tumors (second to ALL). Twenty percent JPA, 15–20% malignant glioma/GBM, 15% medulloblastoma, 5–10% pituitary, 5–10% Ependymoma, <5% optic nerve glioma. Possible etiologic associations: rubber compounds, polyvinyl chloride, N-nitroso compounds, and polycyclic hydrocarbons. Prior ionizing RT has been associated with new meningiomas, gliomas, and sarcomas (~2% at 20-year), Charlotte et.al (2010). There is a huge range in outcome for patients with primary CNS tumours, from almost guaranteed cure in some conditions (e.g. germinoma) to almost guaranteed fatality in others (e.g. glioblastoma (GBM)). (Kubicky, et.al (2010)).

1.2. Genetics Aspect of Brain Cancer:

NF-1: von Recklinghausen, chromosome 17q11.2, 1/3,500 live births, NF1 encodes neurofibromin, autosomal dominant, 50% germline, 50% new mutations, peripheral nerve sheath neurofibromas, café au lait spots, optic and intracranial gliomas, and bone abnormalities. NF-2: chromosome 22, 1/50,000 live births, NF2 encodes merlin, autosomal dominant, bilateral acoustic neuromas, gliomas, ependymomas, and meningiomas. Von Hippel-Lindau: chromosome 3, autosomal dominant, renal clear cell carcinoma, pheochromocytoma, hemangioblastoma, pancreatic tumors, and renal cysts. Tuberous sclerosis (Bourneville's disease): TSC1 on chromosome 9, TSC2 on chromosome 16, autosomal dominant, subependymal giant cell astrocytoma, retinal and rectal hamartomas. Retinoblastoma: Rb tumor suppressor gene, chromosome 13. Li-Fraumeni syndrome: germline p53 mutation = breast, sarcoma, and brain CA. Turcot's syndrome: primary brain tumors with colorectal CA. Neuroblastoma: N-myc implications commonly seen and serves as a prognostic factor. Kubicky, et.al (2010).

1.3. WHO Classification of Brain Tumors:

Astrocytic Tumours: Pilocytic astrocytoma (WHO grade I); A relatively circumscribed, slowly growing, often cystic astrocytoma occurring in children and young adults, histologically characterized by a biphasic pattern with varying proportions of compacted bipolar cells associated with Rosenthal fibers and loose-textured multipolar cells associated with microcysts and eosinophilic granular bodies/hyaline droplets. Subependymal giant cell astrocytoma (WHO grade I); a benign, slowly growing tumour typically arising in the wall of the lateral ventricles and composed of large ganglioid astrocytes. Pleomorphic xanthoastrocytoma (WHO grade II); With a relatively favorable prognosis, typically encountered in children and young adults, with superficial location in the cerebral hemispheres and involvement of the meninges; characteristic histological

features include pleomorphic and lipidized cells expressing GFAP and often surrounded by a reticulin network as well as eosinophilic granular bodies. Diffuse astrocytoma (WHO grade II); a diffusely infiltrating astrocytoma that typically affects young adults and is characterized by a high degree of cellular differentiation and slow growth; the tumour occurs throughout the CNS but is preferentially located supratentorial and has an intrinsic tendency for malignant progression to anaplastic astrocytoma and, ultimately, glioblastoma. Anaplastic astrocytoma (WHO grade III): a diffusely infiltrating malignant astrocytoma that primarily affects adults, is preferentially located in the cerebral hemispheres, and is histologically characterized by nuclear atypia, increased cellularity and significant proliferative activity. The tumour may arise from diffuse astrocytoma WHO grade II or de novo, i.e. without evidence of a less malignant precursor lesion, and has an inherent tendency to undergo progression to glioblastoma. Glioblastoma (WHO grade IV); the most frequent primary brain tumour and the most malignant neoplasm with predominant astrocytic differentiation; histopathological features include nuclear atypia, cellular pleomorphism, mitotic activity, vascular thrombosis, microvascular proliferation and necrosis. It typically affects adults and is preferentially located in the cerebral hemispheres. Most glioblastomas manifest rapidly de novo, without recognizable precursor lesions (primary glioblastoma). Secondary glioblastomas develop slowly from diffuse astrocytoma WHO grade II or anaplastic astrocytoma (WHO grade III). Due to their invasive nature, glioblastomas cannot be completely resected, and despite progress in radio/chemotherapy, less than half of patients survive more than a year, with older age as the most significant adverse prognostic factor and Gliomatosis cerebri; a diffuse glioma (usually astrocytic) growth pattern consisting of exceptionally extensive infiltration of a large region of the central nervous system, with involvement of at least three cerebral lobes, usually with bilateral involvement of the cerebral hemispheres and/or deep gray matter, and frequent extension to the

brain stem, cerebellum, and even the spinal cord. Gliomatosis cerebri most commonly displays an astrocytic phenotype, although oligodendrogliomas and mixed oligoastrocytomas can also present with the gliomatosis cerebri growth pattern, (Kleihues et.al (2007)).

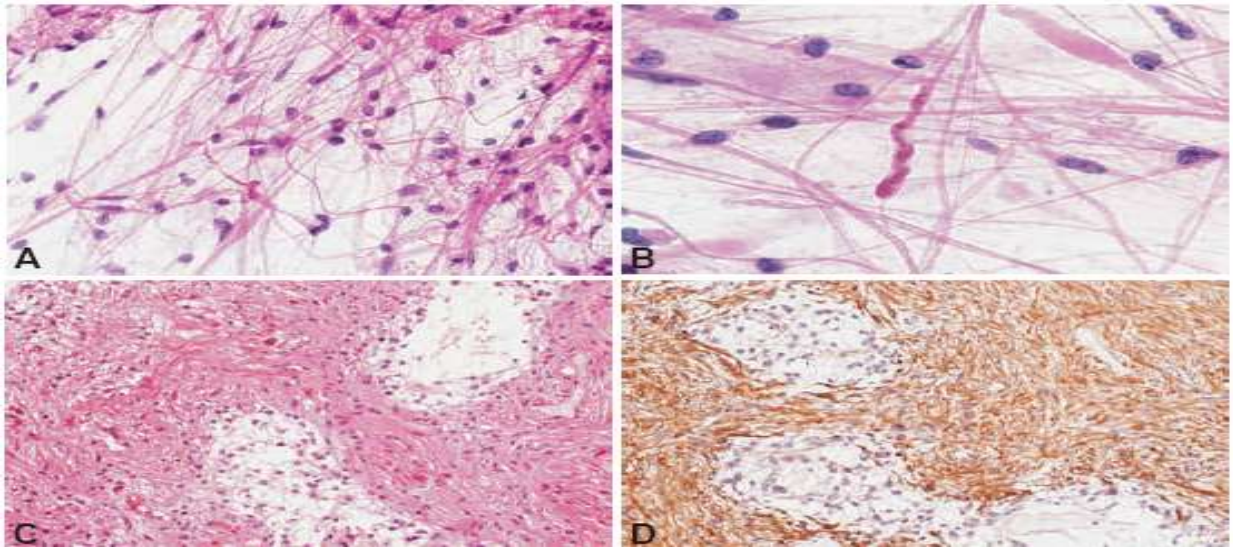

Fig. 1.1. Intraoperative squash preparations of pilocytic astrocytoma showing (A) long, bipolar tumour cells and (B) a Rosenthal fiber. (C), (D) Typical biphasic pattern of compact, fiber-rich, GFAP-expressing areas and hypocellular areas with microcysts, lacking GFAP immunoreactivity. (Scheithauer et.al (2007)).

Oligodendroglial Tumours: Oligodendroglioma (WHO grade II); a diffusely infiltrating, well-differentiated glioma of adults, typically located in the cerebral hemispheres, composed of neoplastic cells morphologically resembling oligodendroglia and often harboring deletions of chromosomal arms 1p and 19q. Anaplastic oligodendroglioma (WHO grade III); an oligodendroglioma with focal or diffuse histological features of malignancy and a less favorable prognosis. Oligoastrocytoma (WHO grade II); a diffusely infiltrating glioma composed of a conspicuous mixture of two distinct neoplastic cell types morphologically resembling the tumour cells in oligodendroglioma and diffuse astrocytoma of WHO grade II. And Anaplastic

Oligoastrocytoma (WHO grade III); an oligoastrocytoma with histological features of malignancy, such as increased cellularity, nuclear atypia, pleomorphism and increased mitotic activity. (Reifenberger et.al (2007)).

Ependymal Tumours: Subependymal (WHO grade I); A slowly growing, benign neoplasm, typically attached to a ventricular wall, composed of glial tumour cell clusters embedded in an abundant fibrillary matrix with frequent microcytic change. Myxopapillary ependymoma (WHO grade I); a slowly growing ependymal glioma with preferential manifestation in young adults and almost exclusive location in the region of the conus medullaris, cauda equina and filum terminale of the spinal cord; typically characterized histologically by tumour cells arranged in a papillary manner around vascularized myxoid stromal cores. Ependymoma (WHO grade II) a generally slowly growing tumour of children and young adults, originating from the wall of the ventricles or from the spinal canal and composed of neoplastic ependymal cells. And Anaplastic Ependymoma (WHO grade III); a malignant glioma of ependymal differentiation with accelerated growth and unfavorable clinical outcome, particularly in children; histologically characterized by high mitotic activity, often accompanied by microvascular proliferation and pseudopalisading necrosis. (Lendon et.al (2007)).

Choroid Plexus Tumours: Choroid plexus papilloma (WHO grade I); a benign, ventricular papillary neoplasm derived from choroid plexus epithelium. Atypical choroid plexus papilloma (WHO grade II); a choroid plexus papilloma with increased mitotic activity and greater likehood of recurrence. Choroid plexus carcinoma (WHO grade III); a frankly malignant choroid plexus neoplasm. (Paulus and Brandner (2007)).

Other Neuroepithelial Tumours: (a) Astroblastoma; A rare glial neoplasm mainly affecting children, adolescents and young adults, composed of GFAP-positive cells with broad, non- or

slightly-tapering processes radiating towards central blood vessels that often demonstrate sclerosis. (b) Chordoid glioma of the third ventricle (WHO grade II); a rare, slowly growing, non-invasive, glial tumour located in the third ventricle of adults, histologically characterized by clusters and cords of epithelioid, GFAP-expressing tumour cells within a variably mucinous stroma typically containing a lympho-plasmacytic infiltrate. (c) Angiocentric glioma (WHO grade I); An epilepsy-associated, stable or slowly growing cerebral tumour primarily affecting children and young adults; histopathologically characterized by an angiocentric pattern of growth, monomorphous bipolar cells and features of ependymal differentiation. (Aldape and Rosenblum (2007)).

Tumours of the Pineal Region*:* (a) Pineocytoma (WHO grade I); A rare, slowly growing, grossly demarcated pineal parenchymal neoplasm occurring mainly in adults and composed of relatively small, uniform, mature-appearing pineocytes often forming large pineocytomatous rosettes. (b) Pineal parenchymal tumour of intermediate differentiation (WHO grades II or III); A pineal parenchymal neoplasm of intermediate-grade malignancy, affecting all ages and composed of diffuse sheets or large lobules of uniform cells with mild to moderate nuclear atypia and low to moderate level mitotic activity. (c) Pineoblastoma (WHO grade IV); A highly malignant primitive embryonal tumour of the pineal gland, preferentially affecting children, frequently associated with CSF dissemination, and composed of dense, patternless sheets of small cells with round to somewhat irregular nuclei and scant cytoplasm. (d) Papillary tumour of the pineal region: A rare neuroepithelial tumour of the pineal region in adults, characterized by papillary architecture and epithelial cytology, immunopositivity for cytokeratin and ultrastructural features suggesting ependymal differentiation. (Nakazato et.al (2007)).

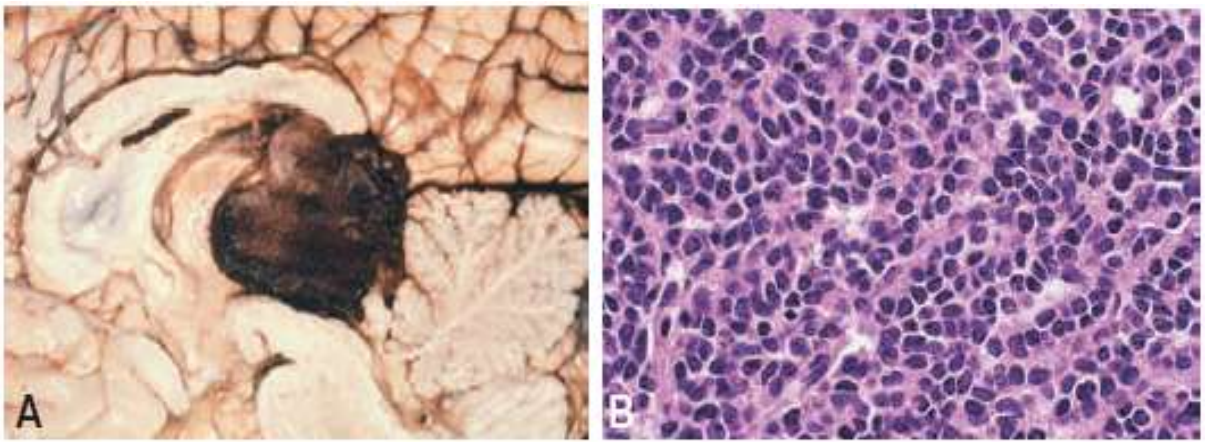

Fig. 1.2. (A) Large, haemorrhagic pineoblastoma. (B) Highly cellular pineoblastoma showing undifferentiated small cell histology. (Nakazato et.al (2007)).

Embryonal Tumours: (a) Medulloblastoma (WHO grade IV); a malignant, invasive embryonal tumour of the cerebellum with preferential manifestation in children, predominantly neuronal differentiation, and an inherent tendency to metastasize via CSF pathways. (b) Central nervous system primitive neuroectodermal tumours (WHO grade IV); a heterogeneous group of tumours occurring predominantly in children and adolescents. They may arise in the cerebral hemispheres, brain stem or spinal cord, and are composed of undifferentiated or poorly differentiated neuroepithelial cells which may display divergent differentiation along neuronal, astrocytic, and ependymal lines. CNS/ supratentorial PNET is an embryonal tumour composed of undifferentiated or poorly differentiated neuroepithelial cells. Tumours with only neuronal differentiation are termed cerebral neuroblastomas or, if ganglion cells are also present, cerebral ganglioneuroblastomas. Tumours that recreate features of neural tube formation are termed medulloepitheliomas. Tumours with ependymoblastic rosettes are termed ependymoblastomas. Features common to all CNS PNET variants include early onset and aggressive clinical behavior. (c)Atypical teratoid/rhabdoid tumour (WHO grade IV); a highly malignant CNS tumour predominantly manifesting in young children, typically containing rhabdoid cells, often with

primitive neuroectodermal cells and with divergent differentiation along epithelial, mesenchymal, neuronal or glial lines; associated with inactivation of the INI1/hSNF5 gene in virtually all cases. (Giangaspero et.al (2007)).

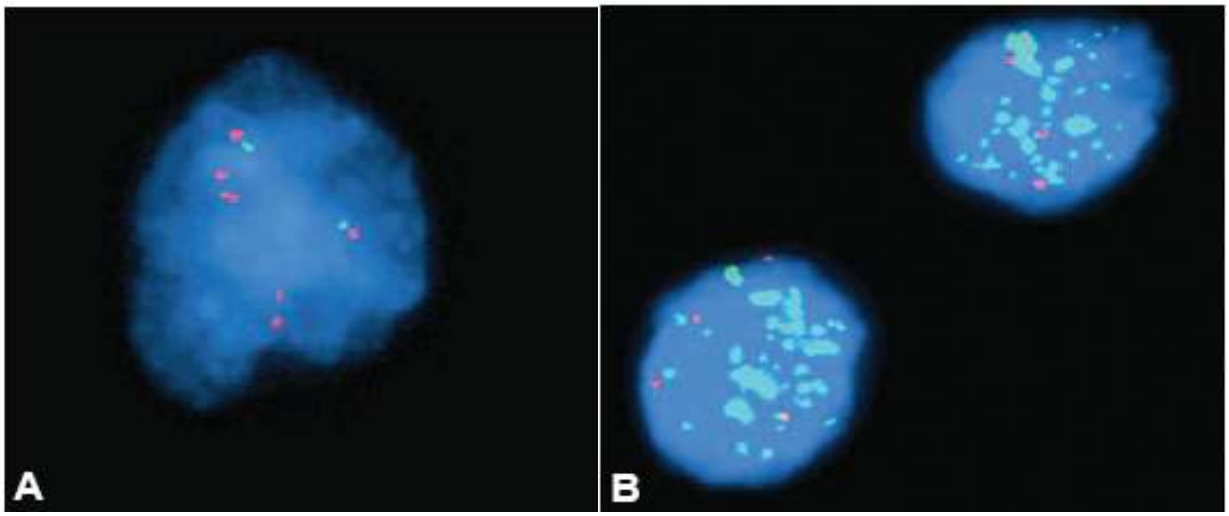

Fig 1.3. An Isochromosome 17q. This nucleus shows two sets of 3:1 (17q - red: 17p - green) signal Profiles indicating loss of 17p and gain of 17q. B MYC amplification. These nuclei show multiple clumped MYC signals (green). The red signals from centromere probes indicate chromosome 8 copy number. Giangaspero et.al (2007).

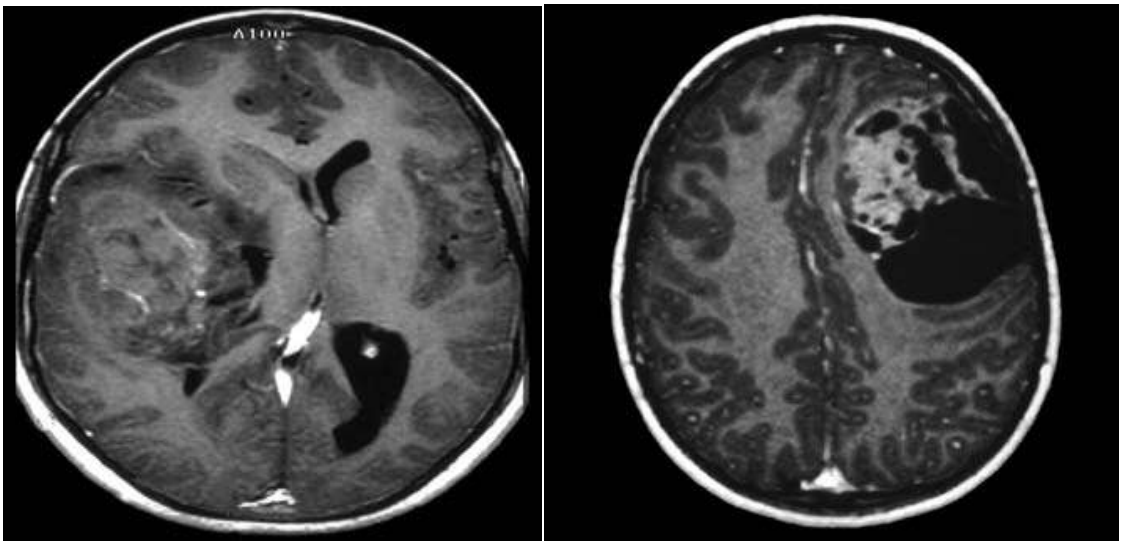

Fig 1.4. T1-weighted MRI of a large, hemispheric PNET with advanced neuronal differentiation (neuroblastoma). (Left) T1-weighted gadolinium-enhanced MRI of a cystic medulloepitheliomas in the frontal lobe. (Right). (Giangaspero et.al (2007)).

Germ Cell Tumours: Morphological and immunophenotypic homologues of gonadal and other extra-neuraxial germ cell tumours; Germinoma, Mature teratoma, immature teratoma, Teratoma with malignant transformation, Yolk sac tumour (endodermal sinus tumour), embryonal carcinoma and Choriocarcinoma. (Rosenblum et.al (2007)).

1.4. Assessment of Primary Disease:

Gliomas may present with symptoms of raised intracranial pressure, including headache, nausea and vomiting, cognitive or behavioral problems, focal neurological deficits or epilepsy. Spinal cord gliomas can cause pain, weakness, or numbness in the extremities, and glioma of the optic nerve may present with visual loss. A full general and neurological examination is needed to detect extent of impairment. PS should be recorded. Early discussion is needed between neurologist, radiologist, neurosurgeon and oncologist to agree an appropriate plan for each individual. Since neurosurgical services are often located in specialized centers, videoconferencing can be very helpful. Whole brain or spinal CT will reveal the site of the tumour and show areas of low density (necrosis) or calcification. However, MRI with gadolinium enhancement is the investigation of choice. T1-weighted sequences show low signal density and T2-weighted a high signal density in comparison with the rest of the brain. For grade III tumours, a contrast enhanced CT will show a low density tumour with ring enhancement. There is heterogeneity within the tumour and associated oedema. For grade IV tumours, oedema will be seen outside the ring enhancement.

Grade cannot be predicted accurately by imaging and 40 per cent of tumours diagnosed as LGG will be HGG after biopsy. PET and various functional MRI approaches may give additional information. Postoperative MRI is used to assess completeness of resection. If EBRT is given in a different hospital, good liaison between surgeon and oncologist following resection is important to maintain continuity of care for the patient. (Barrett et.al (2009)).

1.5. Imaging of Brain Tumors:

Brain scan using Magnetic resonance imaging may require to diagnose variety of the brain disease including: MS, Primary tumour assessment and/or metastatic disease, AIDS (toxoplasmosis), Infarction (cerebral vascular accident (CVA) versus transient ischemic attack (TIA)), Haemorrhage, Hearing loss, Visual disturbances, Infection, Trauma, Unexplained neurological symptoms or deficit, Preoperative planning, Radiation treatment planning, Follow-up (surgical or treatment). MRI: T1 pre and post gadolinium, T2, and FLAIR (fluid attenuation inversion recovery, removes increased CSF signal on T2). Tumor Enhancement with gadolinium correlates with breakdown of the blood–brain barrier (BBB). Tumor: high grade–increased signal on T1 postgadolinium and T2 (T2 also shows edema). Low grade – increased signal on T2/FLAIR. Acute blood = increased signal on T1 pregadolinium. Post-op MRI should be performed within 48 h to document any residual disease after surgical intervention. JPA: enhancing nodule, highly vascular, 50% associated with cysts, high uptake on PET. Grade 2 glioma: nonenhancing, hypointense on T1, hyperintense on T2/FLAIR, well-circumscribed, solid, round, calcifications associated with oligodendroglioma. Grade 3 glioma: enhancing with gadolinium, infiltrative, less well-defined borders, mass effect (sulcal effacement, midline shift, ventricular dilatation, and vasogenic edema). GBM: rim enhancing, central necrosis, irregular borders, and mass effect. Dural tail sign: this could represent tumor or increased vascularity, linear meningeal thickening and enhancement associated with some tumors adjacent to meninges, reported in 60% of meningioma, also seen in chloroma, lymphoma, and sarcoidosis. MR spectroscopy: NAA = neuronal marker, choline = marker of cellularity and cellular integrity, creatine = marker of cellular energy, lactate = marker of anaerobic metabolism. Tumor = increased choline, decreased creatine, decreased NAA. Necrosis = increased lactate, decreased choline, creatine, and NAA. Dynamic MR Perfusion:

astrocytoma = increased relative cerebral blood volume (CBV), generally increasing with grade. Oligodendroglioma = even low-grade, may have high CBV due to hypervascularity. Radiation necrosis and tumefactive demyelinating lesions = low CBV. The use of gadolinium-based MR contrast has been associated with development of nephrogenic systemic fibrosis (NSF) in patients with chronic kidney disease maintained on dialysis. For patients with GFR < 30, gadolinium-based MR contrast should be avoided. For patients with GFR of 30-100, use of contrast is determined on a case by case basis, based on institutional protocols. (Kuo et.al (2007)).

1.6. Radiotherapy Treatment of Brain Tumors:

The patient lies supine with the head immobilized in an individual Perspex or thermoplastic shell. More rigorous immobilization with a stereotactic frame and mouth bite is possible. It's more important to use the CT scan for planning but MRI is more sensitive than CT scanning for demonstrating tumour extent. Tumours are non-enhancing with low signal intensity on T1-weighted and high signal on T2. Active tumour lies mainly within areas of T2 hyperintensity but can extend up to 2 cm from it. Since MRI cannot be used for planning treatment alone, CT planning scans using intravenous contrast are taken with 1–3 mm slices from the vault to the base of the skull. Pre-and postoperative MR images are then co-registered with the CT planning scans and the target volumes delineated. (Barrett et.al (2009)).

1.6.1. Target Volume Definition:

GTV: Grade I–II: The initial preoperative GTV seen on T2-weighted MRI is outlined on fused MR/CT planning images and includes areas of peritumoural oedema shown as low density on CT scan.

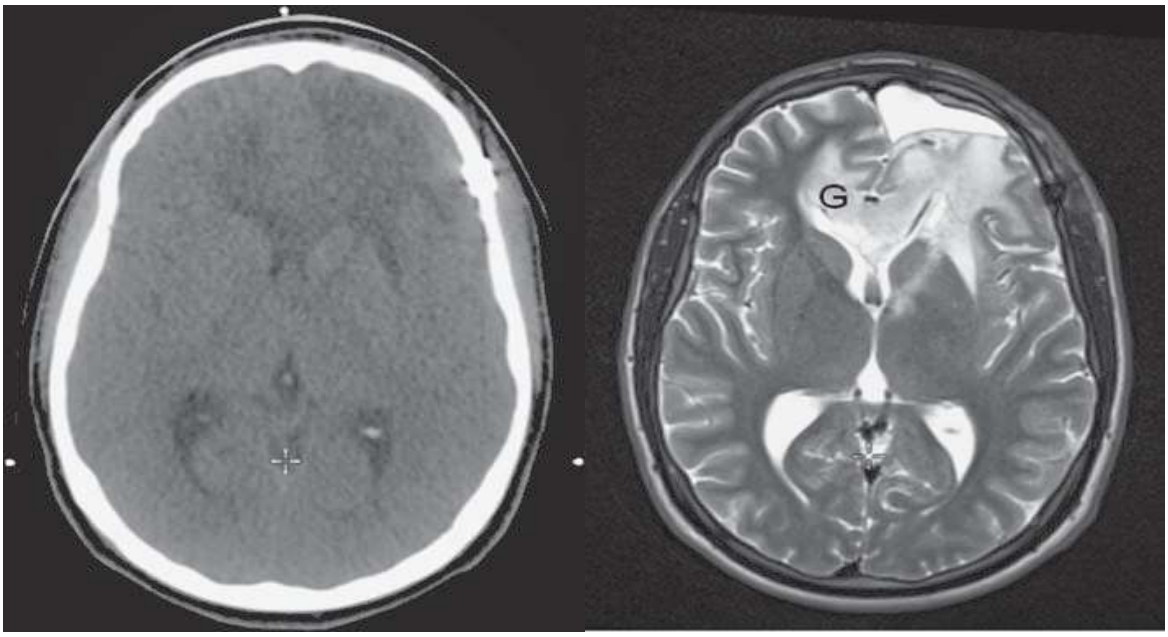

Fig 1.5. Comparison of (left) CT and (right) fused T2-weighted MR/CT images for low grade glioma (G) to illustrate value of fusion. Note fluid in postoperative cavity anteriorly. (Barrett et.al (2009)).

Grade III–IV: The GTV is delineated at the contrast-enhancing edge of the tumour (not oedema) on postsurgical gadolinium enhanced T1-weighted MRI scans fused with planning CT

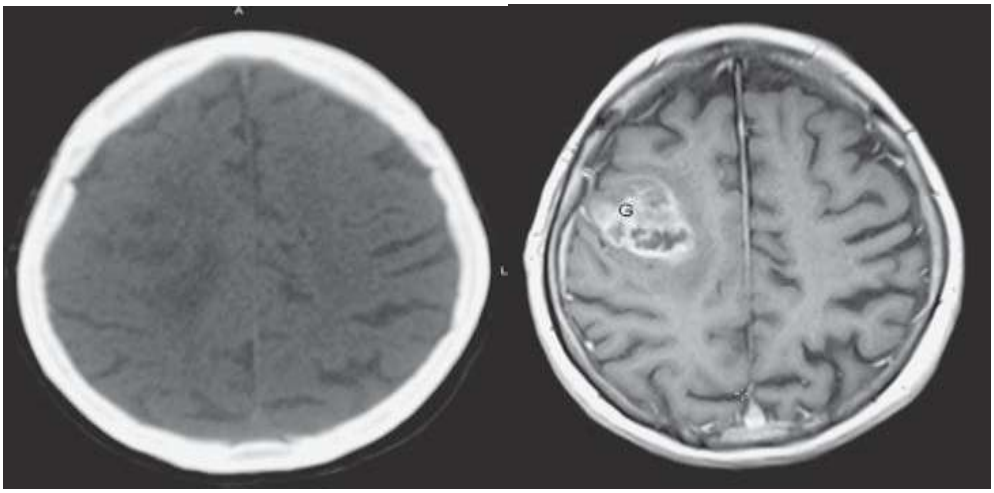

Fig 1.6. Comparison of (left) CT and (right) fused T1-weighted contrast-enhanced MR/CT images for high grade glioma (G) to illustrate value of fusion. (Barrett et.al (2009)).

For palliative treatment, the GTV includes gross visible tumour as seen on a CT planning scan. CTV: Two CTVs are defined according to dose to be delivered and reflect degree of infiltration dependent on tumour grade: Grade II: CTV54= GTV+15mm, Grade III: CTV45= GTV+ 25mm, CTV54= GTV+15mm. Grade IV: CTV50= GTV+25mm, CTV 60=GTV+15mm. For palliative treatments a single phase CTV margin of 15 mm is added. PTV= A 5 mm margin is added to the CTV taking into account departmental measurements of set-up accuracy. Volumes must be tailored to minimize dose to OAR, such as optic chiasm, and take account of natural barriers to spread such as bone and flax. OAR: These will vary according to the site of the primary tumour. They should be outlined and a PRV added. A clinical decision about relative risks and benefits is needed if PTVs and PRVs volumes overlap. Dose solutions: Conventional; simple coplanar beam arrangements or opposing beams defined on the simulator using 6 MV photons may be appropriate for palliative treatments, but CT scanning is needed to define the GTV. ***Conformal:*** Using CT scanning and MLCs, volumes are tailored to avoid as much normal tissue as possible. Three beam arrangements are often used which may be noncoplanar and should be wedged as appropriate to obtain a satisfactory dose distribution. Complex; Better dose homogeneity across the tumour may be achieved using forward planning IMRT with segmentation or 'field in field' arrangements. Full IMRT may produce optimal plans to meet normal tissue dose constraints if these would limit effective doses to tumour when long-term survival is expected (such as treatment of optic glioma in children). Dose-fractionation: Grade II/III; CTV 45=45 Gy in 25 daily fractions of 1.8 Gy given in 5 weeks, CTV 54= 9 Gy in 5 daily fractions of 1.8 Gy given in 1 week. Grade IV; CTV 50= 50 Gy in 25 daily fractions given in 5 weeks. CTV 60= 10 Gy in 5 daily fractions given in 1 week. Adjustments to this treatment approach may be made in the light of known prognostic factors: Grade IV, PS 0–1 age <70, as above (60 Gy) with temozolomide 75mg/m2 daily throughout

treatment. Grade IV, PS 0–1 Age <65. 40 Gy in 15 daily fractions gives equivalent control rates to higher dose radiotherapy without temozolomide and may be preferred. Grade IV, PS 2 or age >70 or any palliative treatment 30 Gy in 6 fractions over 2 weeks. Other glial tumours Oligodendrogliomas are treated as described above, according to prognostic factors. Choroid plexus carcinomas may be treated palliatively with short-term improved control. With a dose of 54 Gy, symptoms of gliomatosis cerebri may be improved for about 6 months. Medulloblastoma and infratentorial primitive neuroepithelial tumour; ***Data acquisition:*** Conventional immobilization by formerly the patient was treated prone with an individual facial support and a shell down over the shoulders to immobilise the head, neck and shoulders. And for Conformal immobilization; improved technology has now made it possible to treat the patient in the supine position and this is preferred as it is more comfortable and reproducible and is safer if general anaesthesia is required. The patient lies on a carbon-fibre couch top with neck extended with a vacuum molded bag to support the head and shoulders. An individually made Perspex or thermoplastic shell covers the face and shoulders and is attached onto the couch top. Indexed knee rests are used to ensure that the spine is straightened and hips are also fixed in a foam form. The sides of these hip rests act as arm rests to lift the arm above the spine. Anterior and lateral tattoos are placed at the point of hip fixation. (Barrett et.al (2009)).

CT scanning: With the patient in the supine treatment position, whole body images are obtained with 5 mm slices from the vault of the skull to the bottom of the sacrum, with 3 mm slices through the primary tumour. Simulator: The initial volume includes the whole brain and extends to the inferior border of the third or fourth cervical vertebra to allow an adequate margin below the primary tumour in the posterior fossa, to facilitate the matching of the spinal beam and to avoid

the spinal beam exiting through the mouth. For Spine: The spine is treated from the fourth or fifth cervical vertebra to the fourth sacral foramina to include the theca and sacral nerve roots.

Primary tumour: The volume is reduced to cover the primary tumour. Target volume definition Using CT scanning with co-registration of MR images, the GTV-T (preoperative extent of primary tumour and any residual disease after surgery) is outlined. Two CTVs are defined: CTV35 whole brain and spine. CTV54 posterior fossa, or GTV-T +1 cm margin. PTV is determined according to departmental protocols, usually: PTV =CTV +3–5 mm. All OAR for both CTV35 and 54 such as the ear, optic chiasm, pituitary, thyroid, lungs, kidneys, ovaries or testes are outlined for DVH evaluation. Conventional: For conventional treatment, opposing lateral beams with the lower border at C3–4 are applied to cover the whole brain, with a collimator rotation of 7–10° to match the divergence of the posterior spinal beam. A template is made to facilitate lead shielding of extracranial structures (such as eyes, teeth, etc.) or MLC shielding is designed. It is important to check that cribriform plate, anterior and temporal lobes are adequately treated. The lower border of the cranial field is tattooed. Lateral and postero-anterior simulator films of the vertebral column are then taken. The position of the spinal cord is marked on the lateral film and the dose at its central axis calculated over its entire length, which extends from the junction with the cranial field to the fourth sacral foramina. A wax compensator may be required to improve homogeneity over this length. The width of the spinal beam ranges from 4 cm in small children to 6 cm in adults (to cover the lateral spinal roots). For the second phase of treatment, the anterior border passes behind the posterior clinoid process avoiding the pituitary gland. The inferior border lies at the bottom of the first cervical vertebra, and the superior and posterior borders are set to cover the contents of the posterior fossa. (Barrett et.al (2009)).

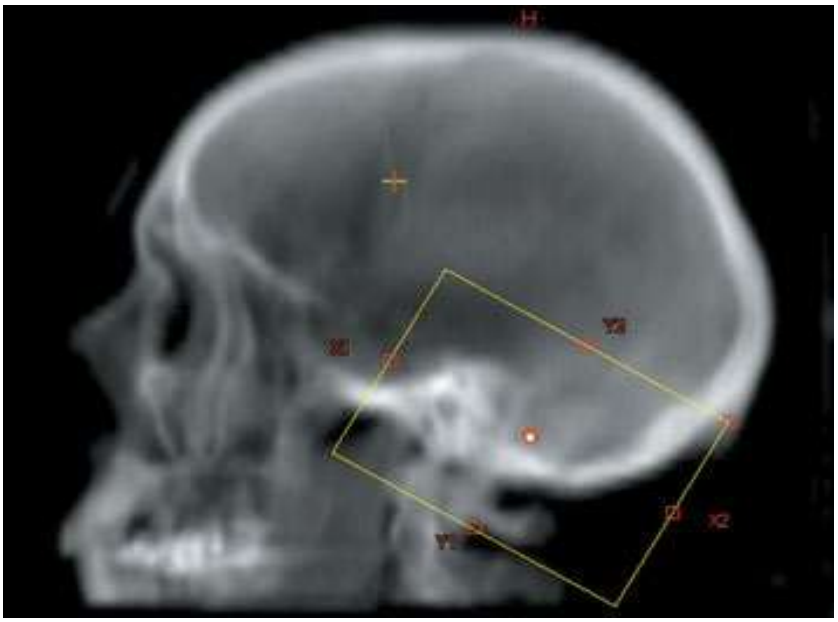

Fig 1.7. Showed the tumor bed irradiation for in medulloblastoma radiotherapy treatment and its field margin, (Barrett et.al (2009)).

Dose solutions: Complex: Beams are designed to cover first the whole brain and spine (CTV_{35}) (Fig. 1.9) and then the posterior fossa (CTV_{54}) defined on axial CT scans and are angled posteriorly to avoid the external auditory meatus and cochlea. MLC is used to shield the face. Multiple segmented beams are used to ensure a homogeneous dose throughout the length of the spine and to prevent overdose at sites of beam junction between skull and spine. Using beam segments, forward planned IMRT, asymmetrical jaws and dynamic wedges, several boost fields can be added to the posterior spine to top up areas of underdose. Tomotherapy™ may improve sparing of critical structures but there is concern about whole body dose, especially in children. Conformal: Whole brain irradiation is delivered using opposing lateral beams. By using MLC with 5 mm leaves if available, the face is shielded from the lateral beams and the Kidneys from the posterior spinal beam. Use of posterior oblique beams, rather than opposing laterals, for treatment to the posterior fossa, makes it possible to avoid the ears to reduce the likelihood of deafness. Barrette et.al (2009).

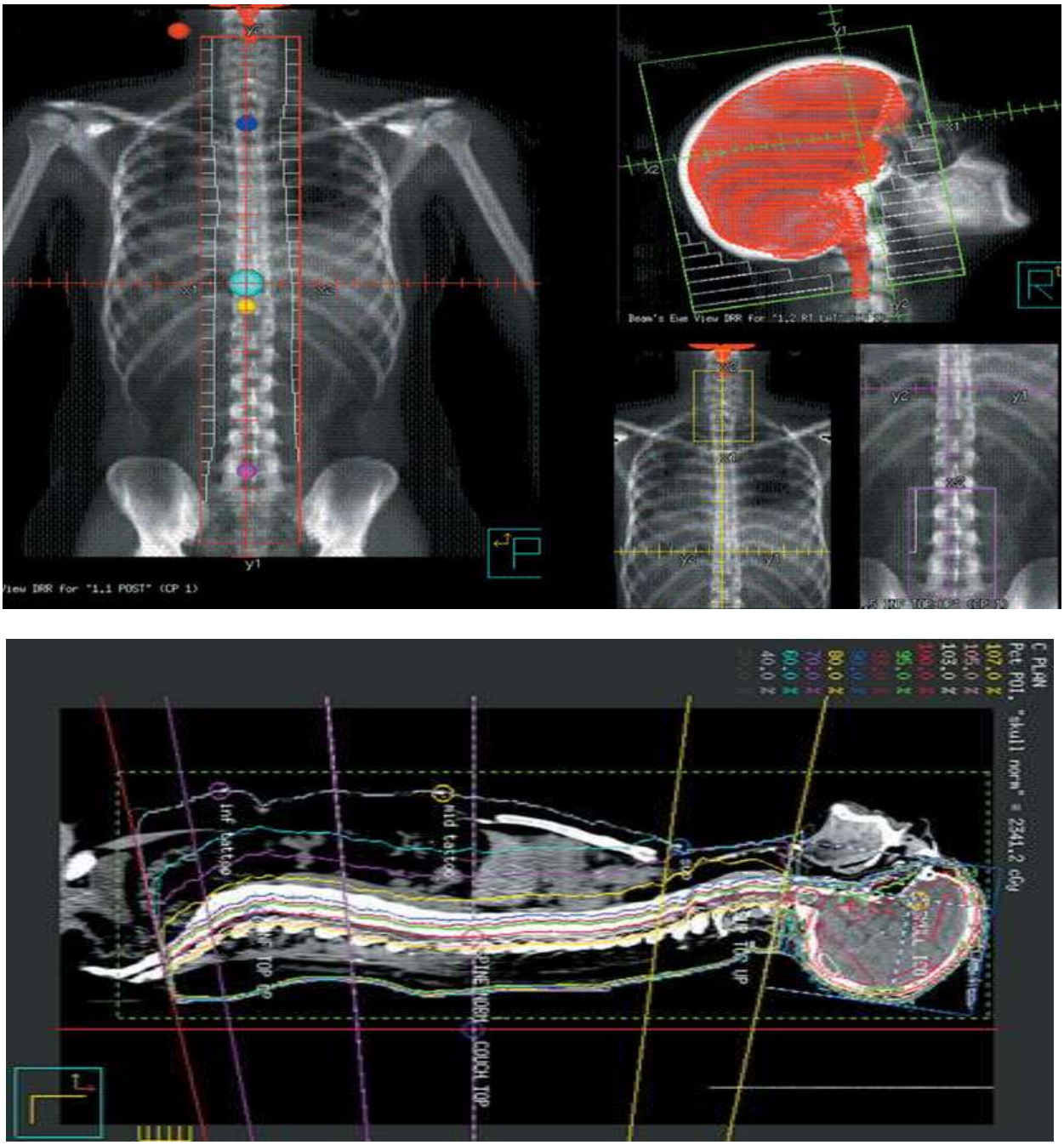

Fig 1.8. (upper left) image showed the spinal filed margin in 3DCRT, (upper right) image plain radiograph for lateral skull demonstrate the cranial filed borders, and lateral whole body CT reconstruction in the (lower) image demonstrate the filed irradiation in case of CSRT 3DCRT with border separation. (Barrett et.al (2009)).

Compensation may be applied at the skull vault and neck. If the uncompensated distribution of dose over the length of the spine exceeds the ICRU recommended limits of _7 per cent/_5 per cent, a physical compensator of aluminium, wax or Perspex may be used to even out the overdose superiorly and the underdose inferiorly.

Conventional: Whole brain and posterior fossa; Treatment is given isocentrically using a linear accelerator and opposing lateral beams as defined in the simulator. The position of the lower cranial border is shifted by 1cm every seven treatments to change the level of the junction with the spinal field. Spinal field; Despite the use of an FSD extended up to 140 cm, two adjacent fields are commonly required to cover the spinal cord in adults and older children. Both this and the craniospinal beam junction are moved caudally every seven treatments. Using a 6 MV linear accelerator it is not possible to spare anterior abdominal structures but shielding can be used to cover the kidneys.

Dose-fractionation; the doses in both phases of the cranial treatment are prescribed to the midplane of the posterior fossa volume. Doses received at the midplane of the whole brain volume are also documented. If there is a variation of more than _5 per cent between the two central doses, compensators must be used with the conventional technique. The spinal dose is prescribed to the central spinal axis (the middle of the spinal cord). 35 Gy to whole brain and spine in 21 daily fractions of 1.66 Gy given in 4½ weeks. 19 Gy boost to posterior fossa in 12 daily fractions of 1.6 Gy given in 2½ weeks.

***Meningioma: CT scanning*;** With the patient immobilized, CT scans are obtained from the skull vault to the base of brain or the first cervical vertebra depending on site of origin of the tumour, with 1–3 mm slice thickness for fusion with MR images. Target volume definition: If surgery is not performed, the whole tumour with any spread along the meninges or through bone must be

encompassed within the GTV. Gadolinium-enhanced T2-weighted MR images are co-registered with CT planning scans and GTV delineated by contouring areas of enhancement. CTV is created by adding a 5mm margin. Normal barriers to spread (such as bone) may in fact be invaded and this must be taken into account if any editing of volumes is done. After macroscopic surgical removal, information from surgeon and pathologist must be taken into account in designing volumes. CTV is defined using presurgical MR images fused with CT scans to identify areas at greatest risk of recurrence, which are the point of attachment to the dura and any meningeal extensions, and intravascular or bony involvement. Invasion into the brain is rare and therefore volume of brain tissue included in the CTV should be minimal. A variable margin (from 1 mm to 5 mm) which will increase with grade of tumour should be added around these areas to allow for microscopic spread. A PTV margin is added according to departmental protocols and measurements and is usually 5 mm. OAR are defined according to the primary site and a PRV created and edited as appropriate. (Barrett et.al (2009)).

Dose solutions: Conventional; Conventional planning and treatment with opposing beams only has a place in the palliative treatment of recurrent tumours where long-term control is not expected. And for Conformal; conformal planning and treatment delivery are essential because of the proximity of critical normal organs. An arrangement of three 6 MV beams is commonly used, chosen to avoid normal structures as much as possible with MLC shielding and wedges to improve dose distribution. Complex; Small meningiomas may be most appropriately treated by proton therapy or stereotactic techniques for which referral to a specialized treatment center may be necessary. For other tumours, a non-coplanar beam arrangement with appropriate MLC shielding and wedges should be used. The dose solution and treatment technique including: 60 Gy in 33

daily fractions of 1.8 Gy given in 61⁄2 weeks. Reduced doses of 51 Gy in 30 daily fractions of 1.7 Gy over 6 weeks may be used for tumours adjacent to optic nerves, chiasm or spinal cord.

1.7. Problem of the Study:

The understanding of the cognitive process of human vision is constantly expanding, much has been learn from the experiment of the visual perception of the image information (Bruce et. al, (2003)) although the use of CT and MRI in detection, diagnosis and treatment planning of brain tumor is widely used in modern radiotherapy technology in determination of TV. The main issue is the detection of the microscopic tumor cell around its mass; which in general not change the signal intensity but it can change the textural pattern; therefore the use of texture analysis technique will make GTV and CTV definition very accurate to be used in treatment of brain tumor and also prevent recurrence.

1.8. Objectives of the Study:

1.8.1. General Objective:

The general objective of this study was to characterize the brain tumors in MRI images by using of image texture analysis in order to recognize the tumor and its surroundings by its texture feature.

1.8.2. Specific Objectives:

- ✓ To identify the region of interest (ROI).
- ✓ To classify the extracted feature using k-mean and discriminate analysis.
- ✓ To develop classification Map for brain tumors relative to the rest of brain tissue.
- ✓ To delineate the radiotherapy GTVs based on selected feature for the brain glioma**.**

1.9. Significant of the Study:

This study highlighted and evaluated the application of texture analysis of brain tumor using image processing programs (IDL) and its techniques, once it need faster and accurate diagnostic modalities in this situation in order to have high diagnostic accuracy in assessing brain tumors and therefore using this scans to plan patient for radiotherapy procedure, which need very accurate delineation of tumor edges in case of CTV and planning target volume in order to deliver sufficient dose to the both volumes and increase therapeutic ratio.

1.10. Overview of the Study:

This study was consist of five chapters, with chapter one is an introduction; introduce briefly this thesis and contained (epidemiology, specified pathology for brain tumors, techniques used in MRI scan and for treatment, problem of study also contain general, specific objectives, significant of study and the overview of the study). Chapter two was literature review about textural analysis in case of brain CT and MRI using different image processing techniques. Chapter three was described the methodology (material, method) was used to achieve the thesis result. Chapter four included presentation (result) of final study; chapter five was discussion, conclusion and recommendation for future scope in addition to references and appendices.

Chapter Two

Literature Review

2.1. Texture Analysis:

Texture analysis refers to the branch of imaging science that is concerned with the description of characteristic image properties by textural features. However, there is no universally agreed-upon definition of what image texture is and in general different researchers use different definitions depending upon the particular area of application (Tuceryan & Jain, 1998). In this chapter texture is defined as the spatial variation of pixel intensities, which is a definition that is widely used and accepted in the field. The main image processing disciplines in which texture analysis techniques are used are classification, segmentation and synthesis. In image classification the goal is to classify different images or image regions into distinct groups (Pietikainen, 2000).

Texture analysis methods are well suited to this because they provide unique information on the texture, or spatial variation of pixels, of the region where they are applied. In image segmentation problems the aim is to establish boundaries between different image regions (Mirmehdi et al., 2008).

By applying texture analysis methods to an image, and determining the precise location where texture feature values change significantly, boundaries between regions can be established. Synthesizing image texture is important in three-dimensional (3D) computer graphics applications where the goal is to generate highly complex and realistic looking surfaces. Fractals have proven to be a mathematically elegant means of generating textured surfaces through the iteration of concise equations (Pentland, 1984). Conversely the ability to accurately represent a textured surface by a concise set of fractal equations has led to significant advances in image compression applications using fractal methods (Distani et al., 2006)

An example of image classification is presented in Fig. 2.1 in which it is possible to uniquely identify the two different textures (left, grass; right, water) by eye. In Fig. 2.2 the image on the left is a composite image formed from eight Brodatz textures, all of which are represented in approximately equal proportions. The right image is a grey-level texture map showing the ideal segmentation of the textures (Weber, 2004).

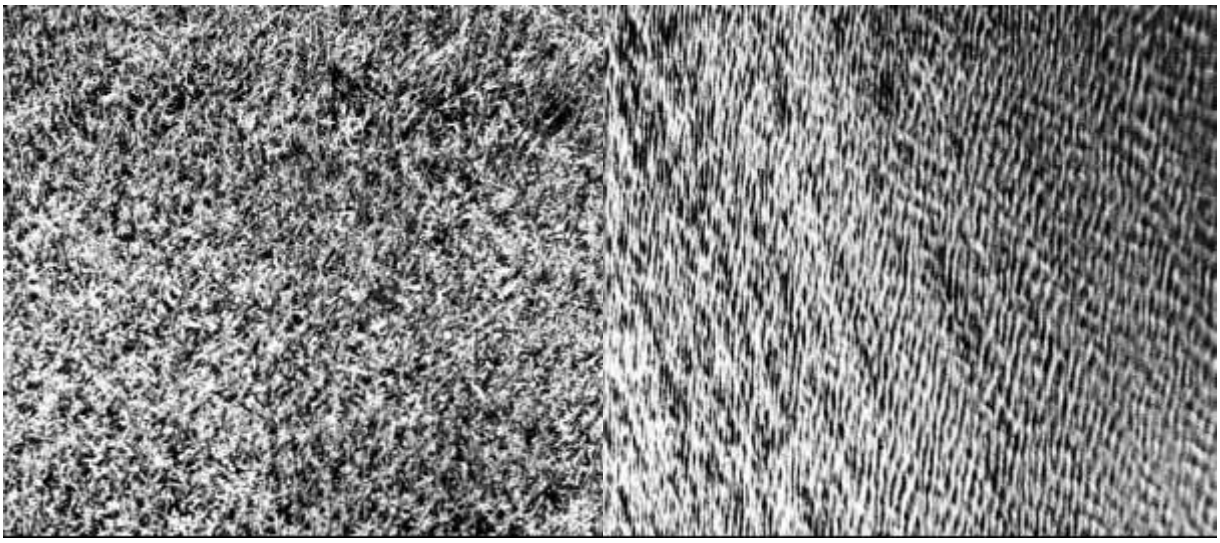

Fig. 2.1. Digital images of two visibly different textured regions extracted from the Brodatz texture database (Brodatz, 1966). Left, image of grass (1.2.01, D9 H.E.). Right, image of water (1.2.08, D38 H.E.) (Weber, 2004).

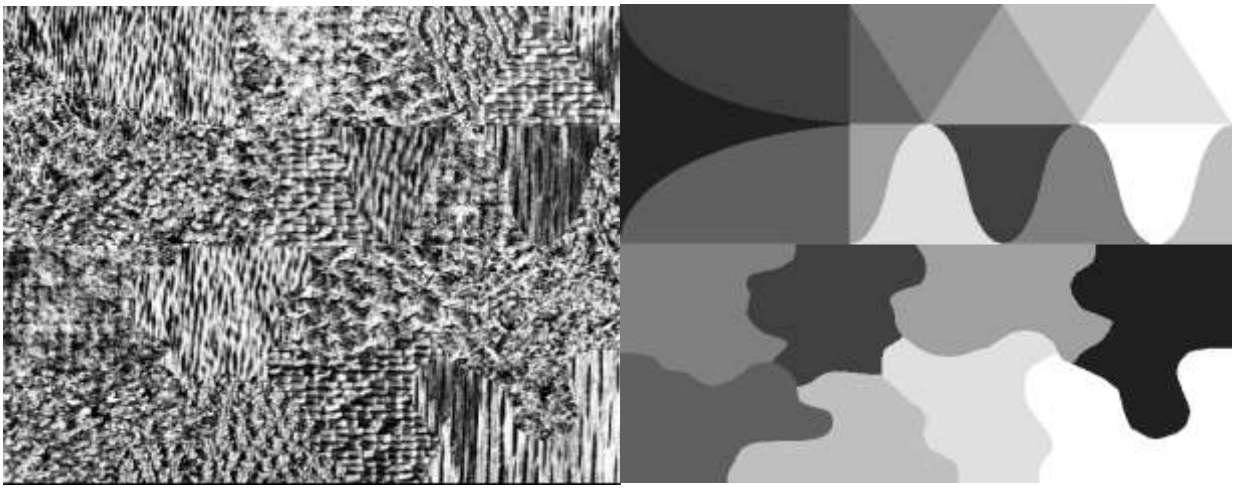

Fig. 2.2. Example of image segmentation using texture analysis to determine the boundary between distinct regions of texture. Left, mosaic image of eight Brodatz textures represented in approximately equal proportions. Right, grey-level texture map showing the ideal segmentation of the textures (Weber, 2004).

2.1.1. The Visual Perception of Texture:

Much of our understanding of machine vision algorithms is a result of attempts to overcome the failings of the human visual system to detect certain textured patterns. This understanding has proven vital in evaluating and comparing the performance of human vision against machine-based texture analysis approaches. Julesz, an experimental psychologist, was an early pioneer in the visual perception of texture (Julesz, 1975). He was responsible for establishing authoritative data on the performance of the human vision system at discriminating certain classes of texture. He verified that discriminating between two image textures depends largely upon the difference in the second-order statistics of the textures. That is, for two textures with identical second-order statistics a deliberate amount of effort is required to discriminate between them. In contrast little effort is required when the second-order statistics of the textures are different. However, this observation does not extend to textures that differ in third- or higher-order statistics, which are not readily discriminated by eye. This is illustrated in Fig. 2.3 in which each of the main textured images (left and right) has a smaller area of similar, but subtly different, texture embedded within it. In the image on the left both the main and embedded areas have identical first-order statistics, however, their second-order statistics are different making it straightforward to discriminate both regions. In the image on the right both textures have identical first- and second-order statistics and therefore it is only after careful scrutiny that the different textured regions become visible. (Julesz, (1975)).

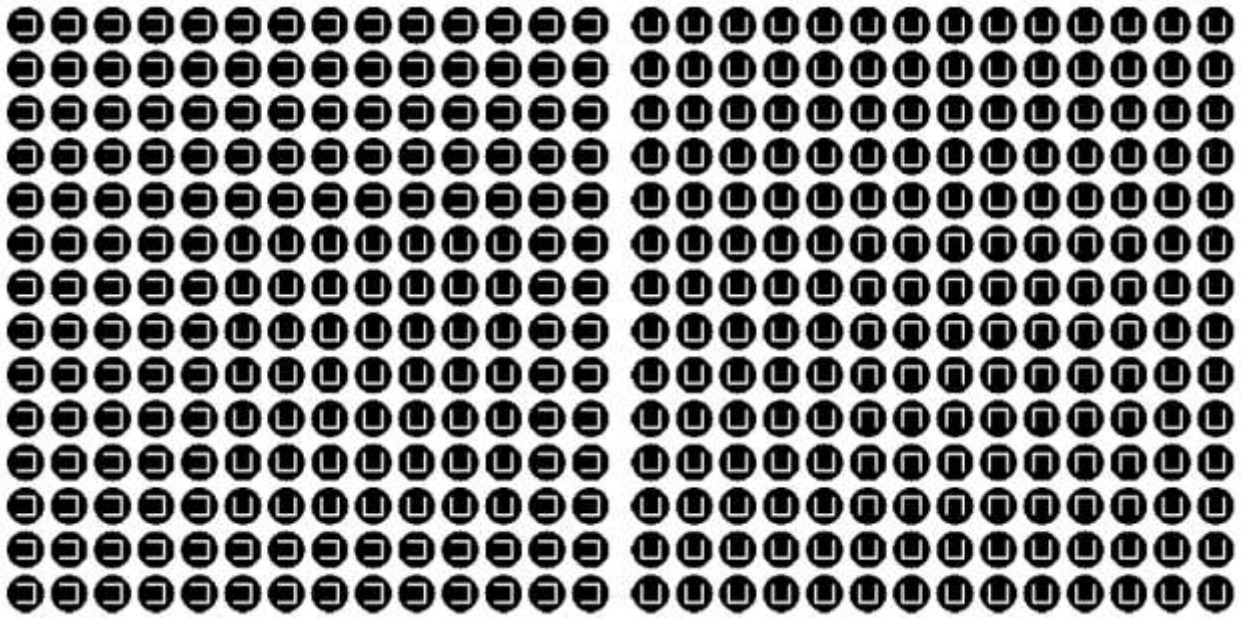

Fig. 2.3. The images on the left and right have a main area of texture embedded within which is a smaller area of similar, but subtly different, texture. In the left image both textures have the same first-order statistics and different second-order statistics, which makes it straightforward for an observer to distinguish between them. In the image on the right both textures have identical first- and second-order statistics and hence only after careful scrutiny are the different patterns visible (Julesz, 1975).

Although our understanding of the cognitive process of human vision is constantly expanding much has been learned from experiments in the visual perception of digital image information (Bruce et al, 2003). Such work is vital, particularly in medical imaging where the misinterpretation of image information can have a serious impact on health (ICRU, 1999). This is particularly apparent in radiotherapy, the treatment of cancer by ionizing radiation, where the aim is to deliver as high a radiation dose as possible to diseased tissue whilst limiting the radiation dose to healthy tissue. Delineation of the tumour volume is based primarily on visual assessment of computerized tomographic (CT) and magnetic resonance (MR) image data by a radiation oncologist. Accurately defining the tumour, and potential areas of tumour involvement, on CT and MR data is a complex image interpretation process requiring considerable clinical experience. As a result significant

inter- and intra-clinician variability has been reported in the contouring of tumours of the lung, prostate, brain and esophagus (Weltens et al., 2001; Steenbakkers et al., 2005).

This variability has been shown to be significant and heavily correlated with the digital imaging modality used and the image settings applied during the assessment. Texture analysis is presented here as a useful computational method for discriminating between pathologically different regions on medical images because it has been proven to perform better than human eyesight at discriminating certain classes of texture. (Julesz, (1975)).

2.1.2. Statistical Approaches for Texture Analysis

To examine an image using texture analysis the image is treated as a 3D textured surface. This is illustrated in Fig. 2.4 which shows the textured intensity surface representation of a (2D) medical image. In first-order statistical texture analysis, information on texture is extracted from the histogram of image intensity. This approach measures the frequency of a particular grey-level at a random image position and does not take into account correlations, or co-occurrences, between pixels. In second-order statistical texture analysis, information on texture is based on the probability of finding a pair of grey-levels at random distances and orientations over an entire image. Extension to higher-order statistics involves increasing the number of variables studied.

Many conventional approaches used to study texture have concentrated on using 2D techniques to compute features relating to image texture. This traditional approach has been used extensively to describe different image textures by unique features and has found application in many disparate fields such as: discrimination of terrain from aerial photographs (Conners & Harlow, 1980); in vitro classification of tissue from intravascular ultrasound (Nailon, 1997); identification of prion protein distribution in cases of Creutzfeld-Jakob disease (CJD) (Nailon & Ironside, 2000); classification of pulmonary emphysema from lung on high-resolution CT images (Uppaluri et al.,

1997; Xu et al., 2004; Xu et al., 2006); and identifying normal and cancerous pathology (Karahaliou et al., 2008, Zhou et al., 2007; Yu et a., 2009). Higher-order approaches have been used to localise thrombotic tissue in the aorta (Podda, 2005) and to determine if functional vascular information found in dynamic MR sequences exists on anatomical MR sequences (Winzenrieth, 2006). Extension of these approaches to 3D is continuing to develop within the machine vision community. Several authors have reported the application of 2D texture analysis methods on a slice-by-slice basis through volumetric data, however, it has been reported that with this approach information may be lost (Kovalev et al., 2001; Kurani et al., 2004). Findings reported by Xu et al., on the use of 3D textural features for discriminating between smoking related lung pathology, demonstrate the power of this approach for this particular application (Xu et al., 2006). Kovalev et al., showed that an extended 3D co-occurrence matrix approach can be used for the classification and segmentation of diffuse brain lesions on MR image data (Kovalev et al., 2001).

Texture analysis has also been used to identify unique pathology on multi-modality images of cancer patients. Using the local binary operator to analyze the weak underlying textures found in transrectal ultrasound images of the prostate, Kachouie and Fieguth demonstrated that the approach was suitable for segmentation of the prostate (Kachouie & Fieguth, 2007). In another cancer-related study of 48 normal images and 58 cancer images of the colon, Esgiar et al., demonstrated that by adding a fractal feature to traditional statistical features the sensitivity of the classification improved (Esgiar et al., 2002).

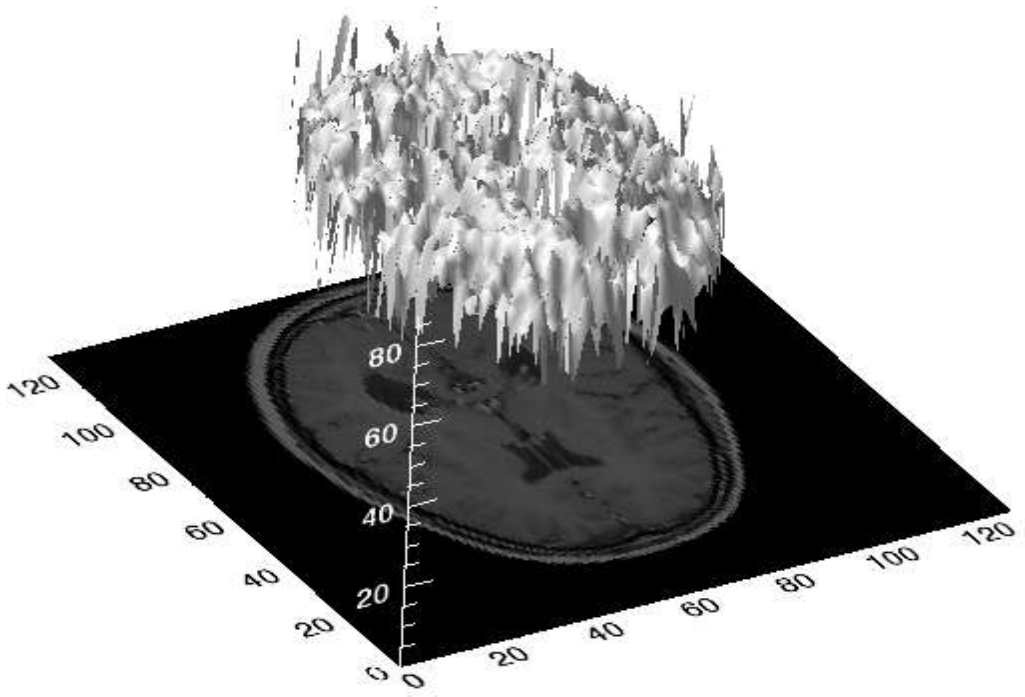

Fig. 2.4. Three-dimensional textured intensity surface representation of a medical image. A: Two-dimensional MR image of the brain. B: Pixel values of the MR image plotted on the vertical axis to produce a 3D textured surface.

With the proliferation of 3D medical image data of near isotropic quality there is an increasing demand for artificial intelligence methods capable of deriving quantitative measures relating to distinct pathology. The remaining sections of this chapter provide a review of statistical and fractal texture analysis approaches in the context of medical imaging and provide comprehensive real-world examples, in the form of two case studies, on the use of these approaches in clinical practice. In case study 1 texture analysis is presented as a means of classifying distinct regions in cancer images, which could be developed further towards automatic classification. In case study 2 texture analysis is presented as an objective means of identifying the different patterns of prion protein found in variant CJD (vCJD) and sporadic CJD. Two contrasting methods are presented in the case studies for evaluating the performance of the texture analysis methodologies. (Nailon et.al (2010))

2.1.2.1. First-Order Statistical Texture Analysis:

First-order texture analysis measures use the image histogram, or pixel occurrence probability, to calculate texture. The main advantage of this approach is its simplicity through the use of standard descriptors (e.g. mean and variance) to characterize the data (Press, 1998). However, the power of the approach for discriminating between unique textures is limited in certain applications because the method does not consider the spatial relationship, and correlation, between pixels. For any surface, or image, grey-levels are in the range $0 \leq i \leq Ng - 1$, where Ng is the total number of distinct grey-levels. If N (i) is the number of pixels with intensity i and M is the total number of pixels in an image, it follows that the histogram, or pixel occurrence probability, is given by,

$$P(i) = \frac{N(i)}{M}.$$

In general seven features commonly used to describe the properties of the image histogram, and therefore image texture, are computed. These are: mean; variance; coarseness; skewness; kurtosis; energy; and entropy.

2.1.2.2. Second-Order Statistical Texture Analysis

The human visual system cannot discriminate between texture pairs with matching second order statistics (Julesz, 1975). The first machine-vision framework for calculating second-order or pixel co-occurrence texture information was developed for analyzing aerial photography images (Haralick et al., 1973).

In this technique pixel co-occurrence matrices, which are commonly referred to as grey-tone spatial dependence matrices (GTSDM), are computed. The entries in a GTSDM are the probability of finding a pixel with grey-level *i* at a distance *d* and angle α from a pixel with a grey-level *j*. This

may be written more formally as P (i, j: d,α). An essential component of this framework is that each pixel has eight nearest-neighbors connected to it, except at the periphery. As a result four GTSDMs are required to describe the texture content in the horizontal ($H_p = 0^0$), vertical ($P_v=90^0$) right- ($P_{RD}=45^0$) and left diagonal ($P_{LD}= 135^0$) directions. This is illustrated in Fig. 5.

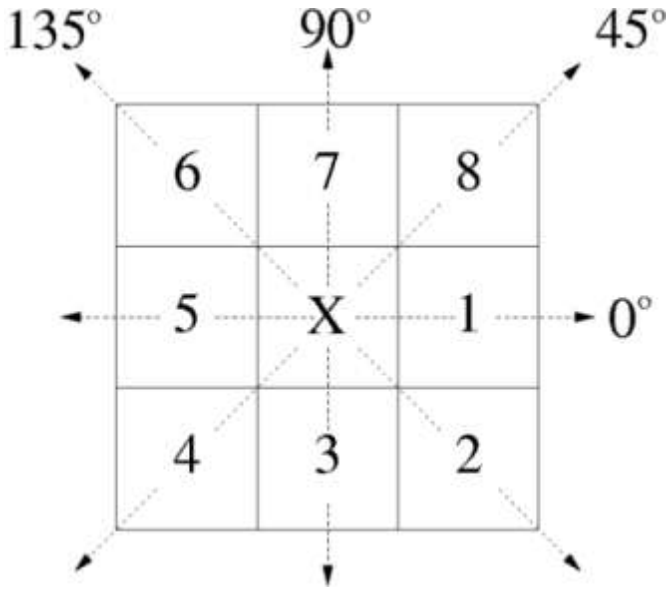

Fig. 2.5. Eight nearest-neighbor pixels used in the GTSDM framework to describe pixel connectivity. Cells 1 and 5 show the horizontal (H_p), 4 and 8 the right-diagonal (P_{RD}), 3 and 7 the vertical (P_v) and 2 and 6 the left-diagonal (P_{LD}) nearest-neighbors. Haralick et al., 1973.

An example of the calculation of a horizontal co-occurrence matrix ($\boldsymbol{H_p}$) on a 4x4 image containing four unique grey-levels is shown in Fig. 2.6. A complete representation of image texture is contained in the co-occurrence matrices calculated in the four directions. Extracting information from these matrices using textural features, which are sensitive to specific elements of texture, provides unique information on the structure of the texture being investigated. Haralick et al., proposed a set of 14 local features specifically designed for this purpose (Haralick et al., 1973).

In practice the information provided by certain features may be highly correlated or of limited practical use. A feature selection strategy is therefore useful with this approach to take account of redundant, or irrelevant, information. It is also interesting to note that prior to any processing the

GTSDMs, which are symmetric, can provide some useful information on the characteristics of the image being studied. For example, the co-occurrence matrix entries for a coarse texture will be heavily focused along the diagonals relative to the distance d between the pixels studied.

0	2	2	2
0	3	2	2
1	2	2	2
3	0	3	0

(P_H)

Grey-Level	0°	0	1	2	3
	0	0	0	1	4
	1	0	0	1	0
	2	1	1	10	1
	3	4	0	1	0

Fig. 2.6. Simple example demonstrating the formation of a co-occurrence matrix from an image. Left, 4x4 image with four unique grey-levels. Right, the resulting horizontal co-occurrence matrix (P_H).

To illustrate the computational requirements of this framework, three of the 14 features proposed by Haralick et al., 1973, are presented in equations 2 to 4.

Angular second moment,

$$f_1 = \sum_{i=1}^{N_q} \sum_{j=1}^{N_q} p'(i,j)^2. \tag{2}$$

Contrast,

$$f_2 = \sum_{i=0}^{N_q-1} n^2 \left[\sum_{i=1}^{N_q} \sum_{j=1}^{N_q} p'(i,j) \right]_{i-j=n} \tag{3}$$

Correlation,

$$f_3 = \sum_{i=1}^{N_q} \sum_{j=1}^{N_q} \frac{(i-\mu_x)(j-\mu_y)p'(i,j)}{\sigma_x \sigma_y}, \tag{4}$$

Where, Nq is the number of distinct grey-levels in the input and μ_x, μ_y, σ_x and σ_y are the means and standard deviations of p' (i, j). Throughout, p' (i, j) P' (i, j)/R, where P (i, j) is the average of (P_H, P_V, P_{LD} and P_{RD}) and R is the maximum number of resolution cells in a GTSDM. (Nailon et.al (2010)).

2.1.2.3. Higher-Order Statistical Texture Analysis:

The grey-level run length method (GLRLM) is based on the analysis of higher-order statistical information (Galloway, 1975). In this approach GLRLMs contain information on the run of a particular grey-level, or grey-level range, in a particular direction. The number of pixels contained within the run is the run-length. A coarse texture will therefore be dominated by relatively long runs whereas a fine texture will be populated by much shorter runs. The number of runs *r´* with gray-level *i*, or lying within a grey-level range *i*, of run length *j* in a direction α is denoted by {*R* (α) = *r´ (i, j|* α)}. This is analogous to the GTSDM technique (Haralick et al., 1973) as four GTRLMs are commonly used to describe texture runs in the directions (0^0, 45^0,90^0 and 135^0) on linearly adjacent pixels. An example of the calculation of a horizontal GLRLM is shown in Fig. 2.7.

0	1	2	2
0	3	2	2
1	2	2	2
3	0	3	0

		Run-Length			
	0^0	1	2	3	4
Grey-Level	0	4	0	0	0
	1	2	0	0	0
	2	0	2	1	0
	3	3	0	0	0

Fig. 2.7. Simple example demonstrating the formation of a GLRLM. Left, 4 x4 image with four Unique grey-levels. Right, the resulting GLRLM in the direction 0^0.

A set of seven numerical texture measures are computed from the GTRLMs. Three of these measures are presented here to illustrate the computation of feature information using this framework.

Short Run Emphasis,

$$f_{SR} = \frac{1}{T_R} \sum_{i=0}^{N_g-1} \sum_{j=1}^{N_r} \frac{r'(i,j \mid \alpha)}{j^2}. \quad (5)$$

Long Run Emphasis,

$$f_{LR} = \frac{1}{T_R} \sum_{i=0}^{N_g-1} \sum_{j=1}^{N_r} j^2 r'(i,j \mid \alpha). \quad (6)$$

Grey-Level Distribution,

$$f_{GD} = \frac{1}{T_R} \sum_{i=0}^{N_g-1} \left[\sum_{j=1}^{N_r} r'(i,j \mid \alpha) \right]^2, \quad (7)$$

Where *g N* is the maximum number of grey-levels, *r N* is the number of different run lengths in the matrix and, *T* serves as a normalizing factor in each of the run length equations.

$$T_R = \sum_{i=0}^{N_g-1} \sum_{j=1}^{N_r} r'(i,j \mid \alpha). \quad (8)$$

2.1.2.4. Fourier Power Spectrum:

Two-dimensional transforms have been used extensively in image processing to tackle problems such as image description and enhancement (Pratt, 1978). Of these, the Fourier transform is one of the most widely used (Gonzalez and Woods, 2001). Fourier analysis can be used to study the properties of textured scenes, for example the power spectrum reveals information on the coarseness/fineness (periodicity) and directionality of a texture. Texture directionality is preserved

in the power spectrum because it allows directional and non-directional components of the texture to be distinguished (Bajscy, 1973).

These observations have given rise to two powerful approaches for extracting texture primitives from the Fourier power spectrum, namely, ring and wedge filters. Working from the origin of the power spectrum the coarseness/fineness is measured between rings of inner radius $r_1$and r_2. The size of the rings can be varied according to the application. The directionality of the texture is found by measuring the average power over wedge-shaped regions centered at the origin of the power spectrum. The size of the wedge $\phi_w=\phi_1-\phi_2$ depends upon the application. Fig. 2.8. illustrates the extraction of ring and wedge filters from the Fourier power spectrum of a 32x32 test image consisting of black pixels everywhere except for a 3x3 region of white pixels centered at the origin.

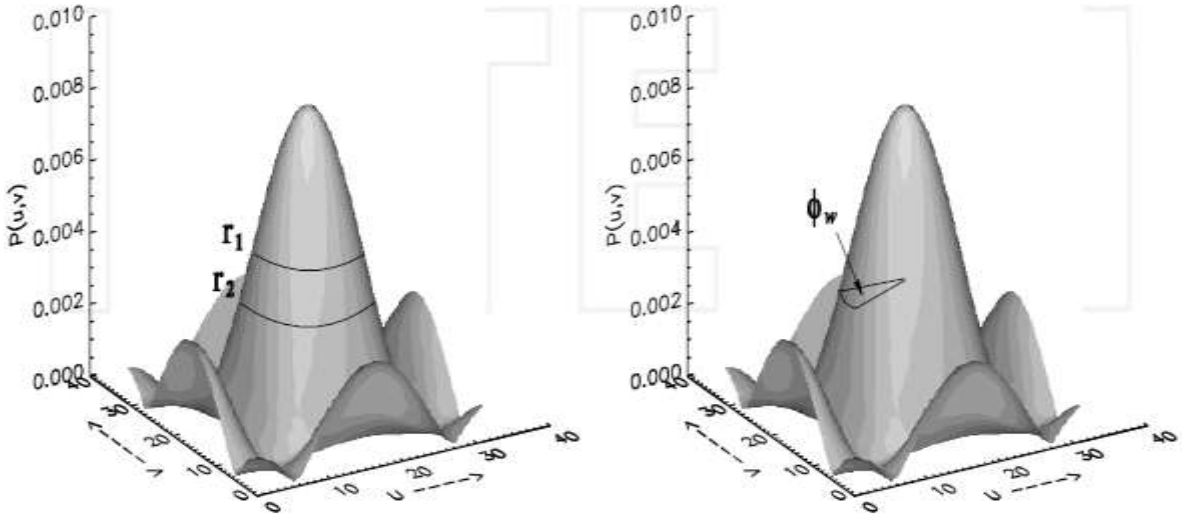

Fig. 2.8. Fourier power spectrum showing the extraction of ring and wedge filters. The spectrum was generated on a 32x32 test image consisting of black pixels everywhere except for a 3x3 region of white pixels cantered at the origin.

In image analysis the Fourier transform $F(u, v)$ is considered in its discrete form and the power spectrum $P(u, v)$ is calculated from,

$$P(u,v) = \left|F(u,v\right|^2. \quad (9)$$

The average power contained in a ring centered at the origin with inner and outer radii R1 and R2 respectively, is given by the summation of the contributions along the direction ϕ,

$$P(r) = 2\sum_{\phi=0}^{\pi} P(r,\phi). \quad (10)$$

The contribution from a wedge of size ϕ_w is found from summation of the radial components within the wedge boundaries. That is,

$$P(\phi_w) = \sum_{r=0}^{n/2} P(r,\phi), \quad (11)$$

Where *n* is the window size.

2.1.2.5. Fractal Texture Analysis:

Until the introduction of fractals it was difficult to accurately describe, mathematically, complex real-world shapes such as mountains, coastlines, trees and clouds (Mandelbrot, 1977). Fractals provide a succinct and accurate method for describing natural objects that would previously have been described by spheres, cylinders and cubes. However, these descriptors are smooth, which makes modelling irregular natural scenes, or surfaces, very difficult. The popularity of fractals has grown considerably over the past three decades since the term was first coined by Mandelbrot to describe structures too complex for Euclidean geometry to describe by a single measure (Mandelbrot, 1977). The fractal dimension describes the degree of irregularity or texture of a surface. With this approach rougher, or more irregular, structures have a greater fractal dimension (Feder, 1988; Peitgen & Saupe, 1988; Peitgen et al., 1992). The property of self-similarity is one of the central concepts of fractal geometry (Turcotte, 1997).

An object is self-similar if it can be decomposed into smaller copies of itself. This fundamental property leads to the classification of fractals into two distinct groups, random and deterministic. A good example of self-similarity is exhibited by an aerial image of an irregular coastline structure that has the same appearance within a range of magnification factors. At each magnification the coastline will not look exactly the same but only similar. This particular feature is common to many classes of real-life random fractals, which are not exactly self-similar. These are referred to as being statistically self-similar. In contrast, objects that do not change their appearance when viewed under arbitrary magnification are termed strictly self-similar. These are termed deterministic fractals due to their consistency over a range of magnification scales. The fractal dimension describes the disorder of an object numerically, which in a sense is similar to the description of objects using standard Euclidean geometry. That is, the higher the dimension the more complicated the object. However, fractal descriptors allow the description of objects by non-integer dimensions. A variety of techniques are used to estimate the fractal dimension of objects which, despite providing the same measure, can produce different fractal dimension values for analysis of the same object. This is due to the unique mechanism used by each technique to find the fractal dimension (Peitgen et al., 1992; Turcotte, 1997).

Two approaches commonly used to calculate the fractal dimension of an image are discussed. The first is the box-counting approach (Peitgen et al., 1992). The second, which treats the input as a textured surface by plotting the intensity at each *x* and *y* position in the *z* plane, calculates the fractal dimension using the Korcak method (Russ, 1994).

2.1.2.6. Fractal Dimension from Box-Counting:

The box-counting dimension is closely related to the concept of self-similarity where a structure is sub-divided into smaller elements, each a smaller replica of the original structure. This sub-

division characterizes the structure by a self-similarity, or fractal, dimension and is a useful tool for characterizing apparently random structures. This approach has been adopted in a variety of applications, for example in the characterization of high resolution satellite images (Yu et al., 2007) and in the detection of cracks in CT images of wood (Li & Qi, 2007).

The box-counting dimension *b D* of any bounded subset of *A* in **R n** , which is a set in Euclidean space, may be formally defined as follows (Stoyan & Stoyan, 1994; Peitgen & Saupe, 1988). Let *N* (*A*) *r* be the smallest number of sets of *r* that cover *A*.

$$D_b(A) = \lim_{r \to 0} \frac{\log N_r(A)}{\log(1/r)}, \tag{12}$$

Then, provided that the limit exists. Subdividing $\mathbf{R}^n$ into a lattice of grid size ***r*x*r*** where *r* is continually reduced, it follows that $N'_R(\mathrm{A})$ is the number of grid elements that intersect *A* and D_b (*A*) is,

$$D_b(A) = \lim_{r \to 0} \frac{\log N'_r(A)}{\log(1/r)}, \tag{13}$$

Provided that the limit exists. This implies that the box counting dimension D_b (*A*) and $N'_R(\mathrm{A})$ are related by the following power law relation,

$$N_r(A) = \frac{1}{r^{D_b(A)}}. \tag{14}$$

Proof of this relation can be obtained by taking logs of both sides of equation (14) and rearranging to form equation (15),

$$\log N_r(A) = D_b(A) \log(1/r). \tag{15}$$

From equation (15) it is possible to make an analogy to the equation of a straight line,

$Y = mx + c$, where m is the slope of the line and c is the y intersect. The box-counting dimension is implemented by placing a bounded set A, in the form of a medical image, on to a grid formed from boxes of size ***rxr***. Grid boxes containing some of the structure, which in the case of a medical image is represented by the grey-levels within a certain range, are next counted. The total number of boxes in the grid that contain some of the structure is $N'_R(A)$. The algorithm continues by altering r to progressively smaller sizes and counting $N'_R(A)$. The slope of the line fitted through the plot of log $(1/r)$ against log $(N'_R(A))$ is the fractal, or box-counting, dimension of the medical image region under investigation.

2.1.2.7. Korcak Fractal Analysis:

This approach uses the idea of a cross-section, or zeroset, through the surface or image to determine the fractal dimension (Russ, 1994). It is implemented by passing a horizontal plane through a 3 D surface in a vertical direction to produce an intersection profile. The points of the surface that lie above the horizontal plane are commonly referred to as islands and the remaining areas of the plane are lakes. This is equivalent to applying a threshold and measuring the area of the islands and lakes that lie above or below the surface. This is illustrated in Fig. 2.9 which shows the result of repeated thresholding on an image of the cerebellum for a case of vCJD. A log-log plot of the number of islands, or lakes, whose area exceeds A is fitted to a straight line (see Fig. 2.10). The slope of this line is used to calculate the fractal dimension. This approach is termed the Korcak method (Russ, 1994).

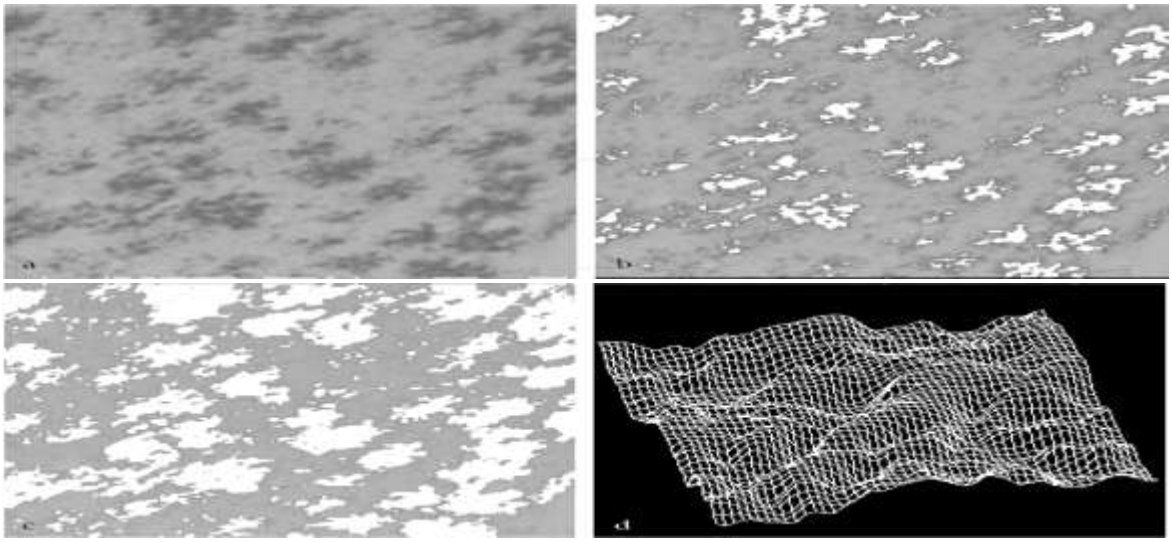

Figure 2.9. A. microscopic image showing the widespread deposition of prion protein in the cerebellum of the v CJD case. b. c. the result of gray-level thresholding. D. the image surface cut by plain or zeroset. Repeating the thresholding at many level and constructing the korcak plot of the cumulative number of island provide a measure of the fractural dimension.

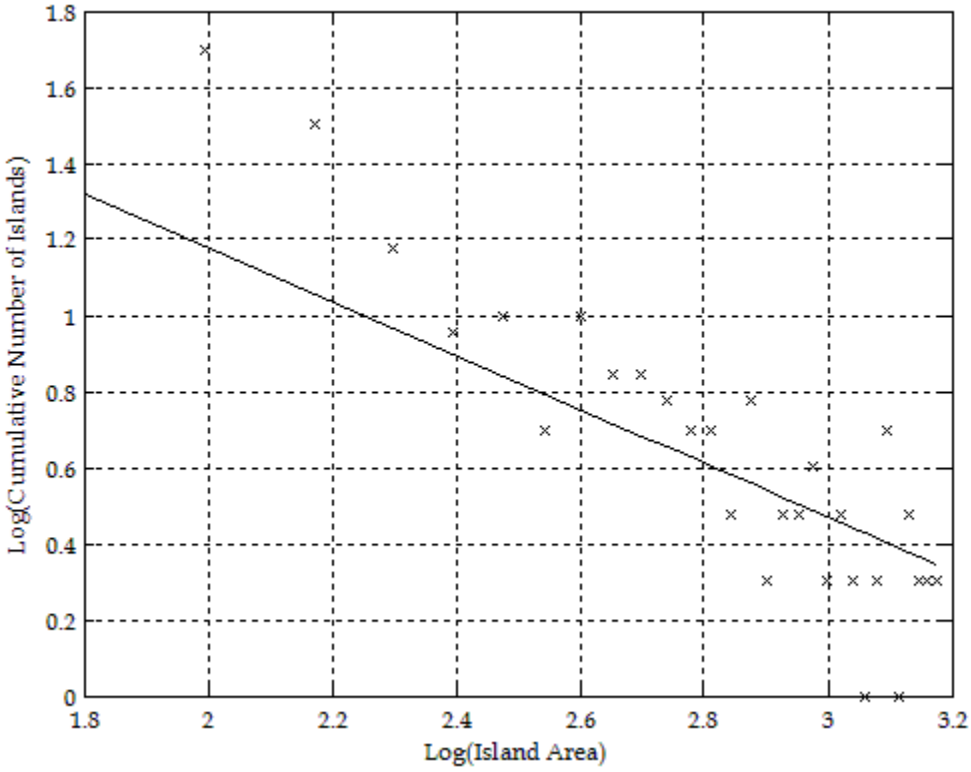

Fig. 2.10. Plot of fractal island area against cumulative number of islands acquired within the area. The slope of the straight line plotted through the data is used to determine the fractal dimension.

2.1.3. Feature Selection, Reduction and Classification:

The texture analysis approaches presented in the preceding sections calculate features that describe properties of the image, or region, being studied. This information is next used in a pattern recognition system to classify the objects, or texture patterns of interest, into an appropriate number of categories or classes (Therrien, 1989). However, some of the features calculated may be highly correlated and some may contain irrelevant information. Feature selection is used to select a subset of features p $\boldsymbol{s}$ from a given set of $\boldsymbol{p}$ features such that $\boldsymbol{S}_p \leq \boldsymbol{p}$ and there is no significant degradation in the performance of the classification system (Therrien, 1989; Zongker & Jain, 1996; Stearns, 1976). The reduction of the feature set reduces the dimensionality of the classification problem and in some cases can increase the performance of the classification accuracy due to finite sample size effects (Jain & Chandrasekaran, 1982). Two powerful methods for reducing the number of features are presented. These are the sequential forward search (SFS) algorithm and its backward counterpart the sequential backward search (SBS) algorithm (Devijver & Kittler, 1982). The pattern recognition system must also be capable of partitioning, or clustering, the reduced feature set into classes of similar observations. The *K*-means algorithm belongs to the collection of multivariate methods used for classifying, or clustering, data and is presented because of its general applicability in classification problems (Therrien, 1989).

2.1.3.1. Feature Selection Using the Sequential Forward Search Algorithm:

The SFS algorithm is a bottom-up strategy for removing redundant or irrelevant features from the feature matrix (Devijver & Kittler, 1982). At each successive iteration the feature that produces the largest value of the selection criterion function *J* is added to the current feature set. Given a set of candidate features $Y \epsilon \boldsymbol{R}$, a subset $X \epsilon \boldsymbol{R}$ is selected without significant degradation to the classification system (Jain & Zongker, 1997). The best subset *X*,

$$X = \{x_i \mid i = 1,2,\ldots,d, \quad x_i = Y\}, \tag{16}$$

Of d features where ($d \leq D$) is selected from the set,

$$Y = \{y_1 \mid j = 1,2,\ldots,D\}, \tag{17}$$

By optimizing the criterion function J, chosen here to be the estimated minimum probability of error. For the set of measurements taken from Y, ideally the probability of correct classification (ר), with respect to any other combination, is given by,

$$\Xi = \{\xi_i \mid i = 1,2,\ldots,d\}. \tag{18}$$

It follows that the minimum probability of error for the space spanned by ξ, for each class ω_i is defined as,

$$E(\Xi) = \int [1 - \max(P(\omega_i \mid \xi))] p(\xi) d(\xi), \tag{19}$$

and the desired criterion function,

$$J(X) = \min(E(\Xi)). \tag{20}$$

One of the disadvantages of the SFS approach is that it may suffer from nesting. That is, because features selected and included in the feature subset cannot be removed, already selected features determine the course of the remaining selection process. This has noticeable hazards since after further iterations a feature may become superfluous. Another limitation of the SFS approach is that in the case of two feature variables, which alone provide little discrimination but together are very effective, the SFS approach may never detect this combination. To overcome this problem it is useful to start with a full set of available features and eliminate them one at a time. This is the method adopted by the SBS approach. (Nailon et.al (2010)).

2.1.3.2. Feature Selection Using the Sequential Backward Search Algorithm:

The SBS is a top down approach, which starts with the complete feature set and removes one feature at each successive iteration (Devijver & Kittler, 1982). The feature that is chosen to be removed is the feature that results in the smallest reduction in the value of the selection criterion function when it is removed. In general, the SBS algorithm requires more computation than the SFS algorithm because initially it considers the number of features in the complete set as forming the subset. Although the SBS overcomes some of the difficulties of the SFS approach the resulting feature subset is not guaranteed to be optimal. Furthermore, like its counterpart the SBS algorithm suffers from nesting because once a feature is selected it cannot be disregarded. Implementation of the SBS approach is analogous to the SFS approach detailed in SFS section. The SBS algorithm is computationally more expensive than the SFS algorithm, however, their performance is comparable. Despite the shortcomings of the SFS and SBS techniques they are powerful techniques for reducing the feature set of real-world pattern recognition problems (Nouza, 1995).

2.1.4. Classification Using the *K*-means Algorithm:

The general clustering problem is one of identifying clusters, or classes, of similar points. For the specific problem presented in this chapter this would involve clustering the features calculated on a specific image region into a unique cluster. The number of classes may be known or unknown depending on the particular problem. The *K*-means algorithm belongs to the collection of multivariate methods used for clustering data (Therrien, 1989; Hartigan, 1975; Duda et al., 2001). The algorithm starts with a partition of the observations into clusters. At each step the algorithm moves a case from one cluster to another if the move will increase the overall similarity within clusters. The algorithm ceases when the similarity within clusters can no longer be increased. Assuming that the number of clusters c N is known in advance the *K*-means technique may be

defined by the following three stages. Assuming that the number of clusters *c N* is known in advance the *K*-means technique may be defined by the following three stages.

***Stage 1 – Initialization*:** For the set of observations $\{Y= y_1, y_2, \ldots\ldots y_N\}$ to be classified into the set of classes $\Omega = \{W_1, W_2, \ldots\ldots W_n\}$, the algorithm starts with an arbitrary partition of the observations into Nc clusters and computes the mean vector of each cluster (μ_1, μ_2, μ_{Nc}) using the Euclidean distance $\|y_i - \mu_k\|^2$ where μ_k is the sample mean of the *kth* cluster.

Stage 2 - Nearest Mean*:** Assign each observation in ***Y to the cluster with the closest mean.

***Stage 3 - Update and Repeat*:** Update the mean vector for each cluster and repeat *Stage 2* until the result produces no significant change in the cluster means.

2.1.5. Texture Analysis of Radiotherapy Planning Target Volumes:

Case study based information's: In the first, a texture analysis approach was used to classify regions of distinct pathology on CT images acquired on eight bladder cancer patients. In the second, texture analysis was used to study the distribution of abnormal prion protein found in the molecular layer of the cerebellum of cases of vCJD and sporadic CJD. The goal of radiotherapy, the treatment of cancer with ionizing radiation, is to deliver as high a dose of radiation as possible to diseased tissue whilst sparing healthy tissue. In curative (radical) radiotherapy planning, delineation of the gross tumour volume (GTV) is primarily based on visual assessment of CT images by a radiation oncologist (Meyer, 2007). The accuracy therefore of the GTV is dependent upon the ability to visualise the tumour and as a result significant inter- and intra-clinician variability has been reported in the contouring of tumours of the prostate, lung, brain and oesophagus (Weltons et al., 2001; Steenbakkers et al., 2005).

The aim of the work presented in this case study was to develop a texture analysis methodology capable of distinguishing between the distinct pathology of the GTV and other clinically relevant

regions on CT image data. For eight bladder patients (six male and two female), CT images were acquired at the radiotherapy planning stage and thereafter at regular intervals during treatment. All CT scans were acquired on a General Electric single slice CT scanner (IGE HiSpeed Fx/I, GE Medical Systems, Milwaukee, WI, USA). Seven patients were scanned with a 3 mm slice thickness and one patient with a 5 mm slice thickness. The repeat CT scans were registered against the corresponding planning reference CT scan to allow comparison of the same region on each image. Image features based on: the first-order histogram (N=7); second-order GTSDM (N=14); higher-order GLRLM (N=5); and a bespoke box-counting fractal approach (N=1) were calculated on preidentified regions of the CT images of each patient (Nailon et al., 2008). Two classification environments were used to assess the performance of the approach in classifying the bladder, rectum and a region of multiple pathology on the axial, coronal and sagittal CT image planes. These were, in the first using all of the available features (N=27) and in the second using the best three features identified by the SFS approach. The classification results achieved are presented in Fig. 11. No significant discrimination was observed between the bladder, rectum and the region of multiple pathology on the axial, coronal and sagittal CT data using all of the available features (N=27). On the contrary, using the three best features identified by the SFS feature reduction approach, significant discrimination between the three pathological groups was possible. These results demonstrate the significant improvement in classification that can be achieved by removing features with little discriminatory power. Moreover the results demonstrate the effectiveness of texture analysis for classifying regions of interest, which may be difficult for the human observer to interpret. The features that were found to work best were all from the GTSDM approach. The feature produced by the bespoke box-counting fractal approach was not found to have significant discriminatory power. However, more research is required into the use of fractal methods in this

application area, particularly because assigning a single dimension to a whole region may not be appropriate (Mandelbrot, 1977).

Furthermore, the fractal dimension calculation may have been influenced by the different distribution of grey-levels in the images due to variations in the amount of urine in the bladder and air in the rectum. Nailon et.al (2010)

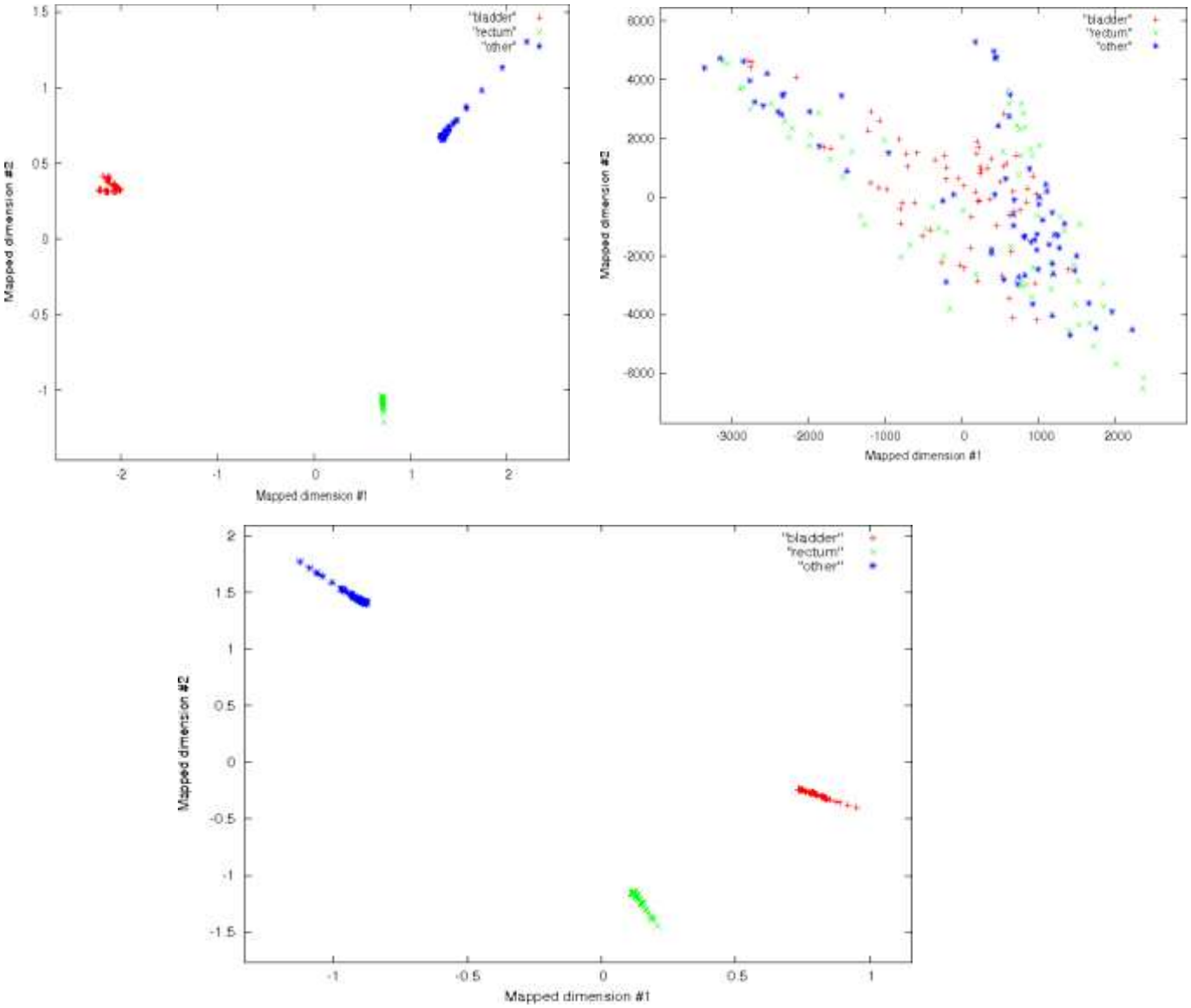

Fig. 2.11. Classification of the bladder, rectum and a region of multiple pathology identified as other on axial CT images through the pelvis using a texture analysis approach. Left (top: axial,

middle: coronal, bottom: sagittal) plots showing the result of using all available features to classify the bladder, rectum and other. Right (top: axial, middle: coronal, bottom: sagittal) plots showing classification of the bladder, rectum and other using the best three features identified by the SFS approach. Sammon mapping was used to generate 2D representations of the multi-dimensional feature space and aid visualization (Sammon, 1969).

The approach was also found to be insensitive to CT resolution and slice thickness for the data set studied. It was also noticed that discrimination of the bladder, rectum and other region in the coronal and sagittal image planes was comparable to the discrimination obtained in the axial plane. This is encouraging given that the coronal and sagittal data sets were produced from the axial data and suffer a loss of resolution because of finite CT slice thickness in the axial data acquisition procedure.

2.2. Previous Study

Abdallah and Hassan, (2014) aims to study the segmentation of brain in MRI images Using Watershed-based Technique and they stated that this was experimental study conducted to study segmentation of brain in MRI images using edge detection and morphology filters. For brain MRI images each film scanned using digitizer scanner then treated by using image processing program (MatLab), where the segmentation was studied. The scanned image was saved in a TIFF file format to preserve the quality of the image. Brain tissue can be easily detected in MRI image if the object has sufficient contrast from the background. We use edge detection and basic morphology tools to detect a brain. The segmentation of MRI images steps using detection and morphology filters were image reading, detection Entire brain, Dilation of the image, filling interior gaps inside the image, removal connected objects on borders and smoothen the object (brain). The results of this study were that it showed an alternate method for displaying the segmented object would be to place an outline around the segmented brain. Those filters approaches can help in removal of unwanted background information and increase diagnostic information of Brain MRI.

Qurat-ul-ain et.al (1996) he stated that the brain tumor diagnosis is a very crucial task. This system provides an efficient and fast way for diagnosis of the brain tumor. Proposed system consists of multiple phases. First phase consists of texture feature extraction from brain MR images. Second phase classify brain images on the bases of these texture feature using ensemble base classifier. After classification tumor region is extracted from those images which are classified as malignant using two stage segmentation process. Segmentation consists of skull removal and tumor extraction phases. Quantitative results show that our proposed system performed very efficiently and accurately. We achieved accuracy of classification beyond 99%. Segmentation results also show that brain tumor region is extracted quite accurately.

Al-Kadi (2009) stated that medical imaging represents the utilization of technology in biology for the purpose of noninvasively revealing the internal structure of the organs of the human body. It is a way to improve the quality of the patient's life through a more precise and rapid diagnosis, and with limited side-effects, leading to an effective overall treatment procedure. The main objective of this thesis is to propose novel tumour discrimination techniques that cover both micro and macro-scale textures encountered in computed tomography (CT) and digital microscopy (DM) modalities, respectively. Image texture can provide significant information on the (ab) normality of tissue, and this thesis expands this idea to tumour texture grading and classification. The fractal dimension (FD) as a texture measure was applied to contrast enhanced CT lung tumour images in an aim to improve tumour grading accuracy from conventional CT modality, and quantitative performance analysis showed an accuracy of 83.30% in distinguishing between advanced (aggressive) and early stage (non-aggressive) malignant tumours. A different approach was adopted for subtype discrimination of brain tumour DM images via a set of statistical and model-based texture analysis algorithms. The combined Gaussian Markov random field and run-length matrix texture measures outperformed all other combinations, achieving an overall class assignment classification accuracy of 92.50%. Also two new histopathological multiresolution approaches based on applying the FD as the best bases selection for discrete wavelet packet transform, and when fused with the Gabor filters' energy output improved the accuracy to 91.25% and 95.00%, respectively. While noise is quite common in all medical imaging modalities, the impact of noise on the applied texture measures was assessed as well. The developed lung and brain texture analysis techniques can improve the physician's ability to detect and analyse pathologies leading for a more reliable diagnosis and treatment of disease.

Multi-feature class assignment for histopathological meningioma tumour images, and he stated that providing an improved technique which can assist pathologists in correctly classifying meningioma tumours with significant accuracy is our main objective. The proposed technique, which is based on optimum texture measure combination, inspects the separability of the RGB colour channels and selects the channel which best segments the cell nuclei of the histopathological images. The morphological gradient is applied to extract the region of interest for each subtype and for elimination of possible noise (e.g. cracks) which might occur during biopsy preparation. Meningioma texture features are extracted by four different texture measures (two model-based and two statistical-based) and then corresponding features are fused together in different combinations after excluding highly correlated features, and a Bayesian classifier was used for meningioma subtype discrimination. The combined Gaussian Markov random field and run-length matrix texture measures outperformed all other combinations in terms of quantitatively characterising the meningioma tissue, achieved an overall classification accuracy of 92.50%, improving from 83.75% which is the best accuracy achieved if the texture measures are used individually. ***Al-Kadi (2009)***

Al-Kadi (2009) also he was applying of multiresolution via wavelet transform and Gabor filters he was stating that with the heterogeneous or non-stationary nature of medical texture, using a single resolution approach for optimum classification might not suffice. In contrast a multiresolution wavelet packet analysis approach can decompose the input signal into a set of frequency subbands giving the opportunity to characterize the texture structure at the appropriate frequency channel. We propose an adaptive best bases algorithm for optimal bases selection for meningioma histopathological images, applying the fractal dimension (FD) as the bases selection criterion in a tree-structured manner. Thereby, the most significant subband that better identifies texture

discontinuities will only be chosen for further decomposition, and its fractal signature would represent the extracted feature vector for classification. The best basis selection using the FD outperformed the energy based selection approach, achieving an overall classification accuracy of 91.25% as compared to 83.44% and 73.75% for the co-occurrence matrix and energy texture signatures; respectively. Another multiresolution approach was used as well, applying this time Gabor filters for feature extraction. The Gabor filter energy output of each magnitude response was combined with four other mono-resolution texture signatures ─ half model based and the other half statistical based ─ with and without cell nuclei segmentation. The highest classification accuracy of 95.00% was reached when combining the Gabor filters' energy and the meningioma subimage fractal signature as a feature vector without performing any prior segmentation. This shows that the use of the FD with wavelet packet transform and Gabor filters assists in achieving an optimum classification.

Georgiadis et.al (2006) stated that three dimensional texture analysis of volumetric brain MR images have been identified as an important indicator for discriminating among different brain pathologies. The aim of the present study was to evaluate the efficiency of three dimensional textural features using a pattern recognition system in the task of discriminating primary from metastatic brain tissues on T1 post-contrast MRI series. Employing a Siemens Sonata 1.5 Tesla MRI Unit (Siemens, Erlangen, Germany), 67 MR series were obtained from the Hellenic Air force Hospital with verified untreated intracranial tumors. The dataset comprised 21 cases with metastasis, 19 cases with meningioma, and 27 cases with glioma. From each case, only T1-weighted post-contrast (Gadolinium) series, with Spin Echo (SE) sequence, Echo Time (TE = 15ms), Repetition Time (TR = 500ms) and Slice Thickness (ST = 1.5mm), were used for further analysis. The reason for employing T1 post-contrast series is the increased diagnostic information

that they encapsulate in comparison to pre-contrast T1 or T2 weighted series. More specifically, contrast administration assists in the separation of tumor from oedema improving visualization, localization and tumor margin delineation. Contrast enhancement is intense because of the hi-degree of Blood Brain Barrier (BBB) disruption. The pattern recognition system was designed employing a probabilistic neural network classifier, specially modified in order to integrate the non-linear least squares feature transformation logic in its discriminant function. The latter, in conjunction with using three dimensional textural features, enabled boosting up the performance of the system in discriminating primary from metastatic with accuracy of 95.52%. The proposed system might be used as an assisting tool for brain tumor characterization on volumetric MRI series.

Mustaqeem et.al (2012) stated that an Efficient Brain Tumor Detection Algorithm Using Watershed & Thresholding Based Segmentation, and he was aims to During past few years, brain tumor segmentation in magnetic resonance imaging (MRI) has become an emergent research area in the field of medical imaging system. Brain tumor detection helps in finding the exact size and location of tumor. An efficient algorithm is proposed in this paper for tumor detection based on segmentation and morphological operators. Firstly quality of scanned image is enhanced and then morphological operators are applied to detect the tumor in the scanned image. The method used in this thesis was; Images are obtained using MRI scan and these scanned images are displayed in a two dimensional matrices having pixels as its elements. These matrices are dependent on matrix size and its field of view. Images are stored in MATLAB and displayed as a gray scale image of size 256*256. The entries of a gray scale image are ranging from 0 to 255, where 0 shows total black color and 255 shows pure white color. Entries between this ranges vary in intensity from black to white. The result of threshold segmentation applied on the images. This is basically the

area with the intensity values higher than the defined threshold. High intensity areas mostly comprises of tumors. So through threshold segmentation we can specify the location of tumor.

Our future work is to extend our proposed method for color based segmentation of 3D images. For this purpose we need a classification method to organize three dimensional objects into separate feature classes, whose characteristics can help in diagnosis of brain diseases.

Lalitha et.al (2013) study A Survey on Image Segmentation through Clustering Algorithm, the goal of this survey on different clustering techniques is to achieve image segmentation. Clustering can be termed here as a grouping of similar images. The purpose of clustering is to get meaningful result, effective storage and fast retrieval in various areas. The goal is to provide a self-contained review of the concepts and the mathematics underlying clustering techniques. Then the clustering methods are presented, divided into: hierarchical, partitioning, density-based, model-based, grid-based, and soft-computing methods. The goal of this survey is to provide a comprehensive review of different clustering and image segmentation techniques. Due to the importance of image segmentation and clustering a number of algorithms have been proposed but based on the image that is inputted the algorithm should be chosen to get the best results.

Karuna and Joshi (2013), Automatic detection and severity analysis of brain tumors using GUI in MATLAB and he was stated that Medical image processing is the most challenging and emerging field now a day's processing of MRI images is one of the parts of this field. The quantitative analysis of MRI brain tumor allows obtaining useful key indicators of disease progression. This is a computer aided diagnosis systems for detecting malignant texture in biological study. This paper presents an approach in computer-aided diagnosis for early prediction of brain cancer using Texture features and neuro classification logic. This paper describes the proposed strategy for detection; extraction and classification of brain tumour from MRI scan

images of brain; which incorporates segmentation and morphological functions which are the basic functions of image processing. Here we detect the tumour, segment the tumour and we calculate the area of the tumour. Severity of the disease can be known, through classes of brain tumour which is done through neuro fuzzy classifier and creating a user friendly environment using GUI in MATLAB. In this research cases of 10 patients is taken and severity of disease is shown and different features of images are calculated.

Bahl et.al (2014) He aims to evaluation of Yarn Quality in Fabric using Image Processing Techniques and he stated that the yarn quality estimate is a tough task in textile industries. In most of the cases, the task is accomplished by manual system. However, it is the classical problem in yarn based research where exact yarn quality production is ascertained based on mathematical yarn qualities like yarn diameter and length etc. In the existing work, it is observed that the yarn quality has been deduced based on yarn length and diameter only. But merely these parameters do not provide much blending permutations and combinations in order to produce different quality variant yarn production. In the presented work, it is proposed to derive more yarn quality parameters like, uniformity of yarn along the axis, thickness profile of yarn along the horizontal axis along with length and diameter. Image processing tools are applied here in order to get the yarn image and extract the yarn features. Further, for yarn quality estimation, a microscopic analysis requires a lot of manual efforts and time and that on compromising on uniformity of quality judgment. The manual analysis does not provide the ease of on-line testing of yarn quality as it is normally off-line and not continuous. Therefore, in order to remove the difficulties in the existing system, a noval on-line testing of yarn quality using statistical analysis is proposed. In the presented work, it is proposed to derive yarn quality parameters like, uniformity of yarn along the axis, thickness profile of yarn along the horizontal axis along with length and diameter. A mathematical model is

proposed to be developed that could predict the fabric quality based on yarn quality determination. A global feature vector set of yarn quality is proposed to be compiled that can be standardized for yarn quality determination. By the method, a quantitative evaluation index is proposed for the yarn quality. The proposed work will provide the basis of further studies on quality of yarn evenness and evaluation of yarn appearance.

Jose (2014) aims to study Texture Feature Extraction for Mammogram Images Using Biorthogonal Wavelet Filter via Lifting Scheme Feature extraction is an important part in Content-based image retrieval (CBIR).It is an active research area over the past few decades. In this paper texture feature extraction of mammogram images are done. Biorthogonal wavelet filter via lifting scheme is used for the extraction of texture features. Maximum likelihood estimator (MLE) is used for texture feature estimation. Here Digital Database for Screening Mammography (DDSM) is used as the database. Here biorthogonal wavelets are used in the lifting scheme to get texture feature vectors of mammogram images. By using lifting scheme in all biorthogonal wavelets, predict and update filter coefficients are also got. These coefficients will be adapted later and thus we can find the optimal wavelet filter bank for increasing the retrieval performance of the retrieval system. By using lifting scheme methodology decomposition of images are done and thus got approximation and detail coefficients of image.

Deswal and Sharma (2014) was aimed to identify the perceived qualities of texture and color in an building mathematical models for object, an optimized and efficient algorithm 'A Fast HSV Image Color and Texture Detection Algorithm' based on color intensity using Artificial Intelligence is presented in this paper. We used color intensity method over conventional method. The 'Fast HSV Image Color and Texture Detection Algorithm' focuses to integrate the detection of image color with detection of texture using AI and Color detection has been among the widest

research area in the field of computer science. In computer vision, there are several pre-existing color models for describing the specification of the colors such as RGB, CMY and HSV. This paper presents detection of color using HSV-based (hue, saturation, value) color model since it greatly decreases the size of color and grey-scale information of an image .This paper can be treated as a reference for getting in depth knowledge of the Color detection and texture detection.

Wakchaure et.al (2014) aims to segment brain tumors on T2-Weighted MRI Images Using Multi-parameter Feature Blocks, on the brain components (edema and necrosis) and internal structures of the brain in 3D MR images. For tumor segmentation we propose a framework that is a combination of region-based and boundary-based paradigms. In this framework, segment the brain using a method adapted for pathological cases and extract some global information on the tumor by symmetry based histogram analysis .The objective of this paper is to present an analytical method to detect lesions or tumors in digitized medical images for 3D visualization. This research opens a new window in the field of image processing by 3D Volume Representation of tumor through the use of Magnetic Resonant Imaging and an integrated software tool called 3D Slicer. The authors developed a tumor detection method using three parameters; edge (*E*), gray (*G*), and contrast (*H*) values. The method proposed here studied the *EGH* parameters in a supervised block of input images. These feature blocks were compared with standardized parameters (derived from normal template block) to detect abnormal occurrences, e.g. image block which contain lesions or tumor cells. The proposed method shows more precision among the others. Processing time is less. This will help the physicians in analyzing the brain tumors accurately and efficiently.

Roy et.al (2012) studies the Detection and Quantification of Brain Tumor from MRI of Brain and its Symmetric Analysis and he stated that in this work a fully automatic algorithm to detect brain tumors by using symmetry analysis is proposed. Here we detect the tumor, segment the tumor and

calculate the area of the tumor. The quantitative analysis of MRI brain tumor allows obtaining useful key indicators of disease progression. The complex problem of segmenting tumor in MRI can be successfully addressed by considering modular and multi-step approaches mimicking the human visual inspection process. The tumor detection is often an essential preliminary phase to solve the segmentation problem successfully. The experiments showed good results also in complex situations. Segmentation of images embraces a significant position in the region of image processing. It becomes more and more significant while normally dealing with medical images; magnetic resonance (MR) imaging suggest more perfect information for medical examination than that of other medical images such as ultrasonic , CT images and X-ray. Tumor segmentation and area calculation from MRI data is an essential but fatigue, boring and time unbearable task when it completed manually by medical professional when evaluate with present day's high speed computing machines which facilitate us to visual study the area and position of unnecessary tissues.

Deepashree et.al (2014) Increasing use of World Wide Web and communication channels like mobile networking has increased the number of images used throughout the world. As processors become increasingly powerful, and memories become increasingly cheaper, the deployment of large image databases for a variety of applications have now become realizable. Databases of art works, satellite and medical imagery have been attracting more and more users in various professional fields; for example, geography, medicine, architecture, advertising, design, fashion, and publishing. Effectively and efficiently accessing desired images from large and varied image databases is now a necessity. Image mining is an extended branch of data mining that is concerned with the process of knowledge discovery concerning digital images. Image retrieval is the basic requirement task in the present scenario. Color Based Image Retrieval (CBIR) is the popular image

retrieval system by which the target image to be retrieved based on the useful features of the given image. The concepts of CBIR and Image mining combined to increase the speed of the image retrieval system.

Gopinath (2012) stated that Medical Image Processing is one of the most challenging and emerging topics in today's research field. Processing of Magnetic Resonance Imaging (MRI) is one of the parts in this field. In recent years, multispectral MRI has emerged as an alternative to Ultrasound (US) image modality for clear identification of cancer in Breast, Prostate and Liver etc,. In order to analyze a disease, Physicians consider MR imaging modality is the most efficient one for identification of cancer present in various organs. Therefore, analysis on MR imaging is required for efficient disease diagnosis. This paper describes the proposed strategy to detect and extraction of Prostate cancer cells from patient's MRI scan image of the Prostate organ. This proposed method incorporates with some noise removal functions, segmentation and morphological functions which are considered to be the basic concepts of Image Processing. Detection and extraction of cancer cells from MRI Prostate image is done by using the MATLAB software.

Laddha, and Ladhake (2014), A Review on Brain Tumor Detection Using Segmentation and Threshold Operations and they stated that the brain is the anterior most part of the central nervous system. The location of tumors in the brain is one of the factors that determine how a brain tumor effects an individual's functioning and what symptoms the tumor causes. Along with the Spinal cord, it forms the Central Nervous System (CNS). Brain tumor is an abnormal growth caused by cells reproducing themselves in an uncontrolled manner. Magnetic Resonance Imager (MRI) is the commonly used device for diagnosis. In MR images, the amount of data is too much for manual interpretation and analysis. During past few years, brain tumor segmentation in magnetic

resonance imaging (MRI) has become an emergent research area in the field of medical imaging system. Accurate detection of size and location of brain tumor plays a vital role in the diagnosis of tumor. An efficient algorithm is proposed for tumor detection based on segmentation and morphological operators. Firstly quality of scanned image is enhanced and then morphological operators are applied to detect the tumor in the scanned image. We also propose an efficient wavelet based algorithm for tumor detection which utilizes the complementary and redundant information from the Computed Tomography (CT) image and Magnetic Resonance Imaging (MRI) images. Hence this algorithm effectively uses the information provided by the CT image and MRI images there by providing a resultant fused image which increases the efficiency of tumor detection.

Padma and Sukanesh (2011), Tumor classification and segmentation from brain computed tomography image data is an important but time consuming task performed manually by medical experts. Automating this process is challenging due to the high diversity in appearance of tumor tissue among different patients and in many cases, similarity between tumor and normal tissue. This paper deals with an efficient segmentation algorithm for extracting the brain tumors in computed tomography images using Support Vector Machine classifier. The objective of this work is to compare the dominant grey level run length feature extraction method with wavelet based texture feature extraction method and SGLDM method. A dominant gray level run length texture feature set is derived from the region of interest (ROI) of the image to be selected. The optimal texture features are selected using Genetic Algorithm. The selected optimal run length texture features are fed to the Support Vector Machine classifier (SVM) to classify and segment the tumor from brain CT images. The method is applied on real data of CT images of 120 images with normal and abnormal tumor images. The results are compared with radiologist labeled ground truth.

Quantitative analysis between ground truth and segmented tumor is presented in terms of classification accuracy. From the analysis and performance measures like classification accuracy, it is inferred that the brain tumor classification and segmentation is best done using SVM with dominant run length feature extraction method than SVM with wavelet based texture feature extraction method and SVM with SGLDM method. In this work, we have attempted to improve the computing efficiency as it selects the most suitable feature extraction method that can used for classification and segmentation of brain tumor in CT images efficiently and accurately. An average accuracy rate of above 97% was obtained using this classification and segmentation algorithm.

Chapter Three
Methodology

This study was aims to characterize the brain tumors in magnetic resonance images using image texture analysis, the data were collected form Radiation Oncology Department, Radiation and Isotopes Center of Khartoum (RICK), for 50 patient with brain tumors (glioma) underwent MR examination of brain.

3.1. Material:

The study executed using magnetic resonance imaging scanner; Signa HDxt 1.5T provides with advanced technology, such as: A proven, homogeneous 1.5T magnet delivering a full 48cm field of view. 16-channel RF. HD gradients engineered for high-fidelity to produce high accuracy waveforms. HD Reconstruction engineered for real-time, high-performance image generation. Advanced, high-definition applications such as Cube and IDEAL that help deliver images with premium quality and clarity. High-Density coils engineered with coil elements that are optimized for the anatomy and exam. GE Signa HDx 1.5T Technical Specifications**;** magnet: 1.5 Tesla, Superconducting, Clinical Application: Whole Body, Configuration: Compact Short Bore, Power Requirements: 480 or 380/415, Cooling System: Closed-loop water-cooled gradient, Cryogen Use: Less than 0.03 L/hr liquid helium, Spectroscopy: Possible, Synchronization: ECG/peripheral, respiratory gating, (SmartPrep, SmartStep), Pulse Sequences (Standard): SE, IR, 2D/3D GRE and SPGR, Angiography: 2D/3D TOF, 2D/3D Phase Contrast; 2D/3D FSE, 2D/3D FGRE and FSPGR, SSFP, FLAIR, EPI, Pulse Sequences (Optional): 2D/3D Fiesta, FGRET, Spiral, Tensor , imaging Modes: 2D single slice, multi slice, and 3D volume images, multi slab, cine, FOV: 1cm to 48cm

continuous, Slice Thickness: 2D 0.7mm to 20mm; 3D 0.1mm to 5mm, Display Matrix: 1028 x 1024, Measuring Matrix: 128 x 512 steps 32 phase encode and Pixel Intensity 256 gray levels,

Also MDCT machine with 64-slice, detector array, fan beam shape, CT monitor in radiation oncology simulator. Image texture analysis programs, IDL Version 7.0.6, Microsoft Windows (Win32 x86 m32). (c) 2008, ITT Visual Information Solutions, Installation number: 20111111.Licensed for use by: TEAM TBE

Fig. (3.1) GE Signa HDx 1.5T that used to scan the patient with brain cancer

3.2. Method of data collection:

Technique: The patient under examination must perform MRI brain the technique performed to scan lesion; *Axial T2–W FLAIR*. The vast majority of intracranial lesions exhibit long *T*2 values. FLAIR is a similar sequence to STIR but in this case it uses a longer inversion time (approximately 2200ms) to suppress CSF and increase conspicuity of the lesion. The axial plane

is useful as it is comparable to CT (TE/TR/TI = 148 /9200ms /2200ms FOV = 22–25cm, Slice thickness/gap = 5/1mm). where the tumor appear to have relatively hypo intense area surround with hyper intense area due to pre-tumoral edema surround brain mass in case of T2 weighted images, also the flair axial T2, axial T1, coronal T2 and T1 AXIAL and sagittal with gadolinium contrast was done to assess the lesion and its surrounding structure and the multi-foculity of the tumors if existed. starting from the both with contrast images and without contrast images was used to determine tumor site and size and tumor relations was assessed using network and computer PACS system was used to visualize the images and patient diagnosis was extracted.

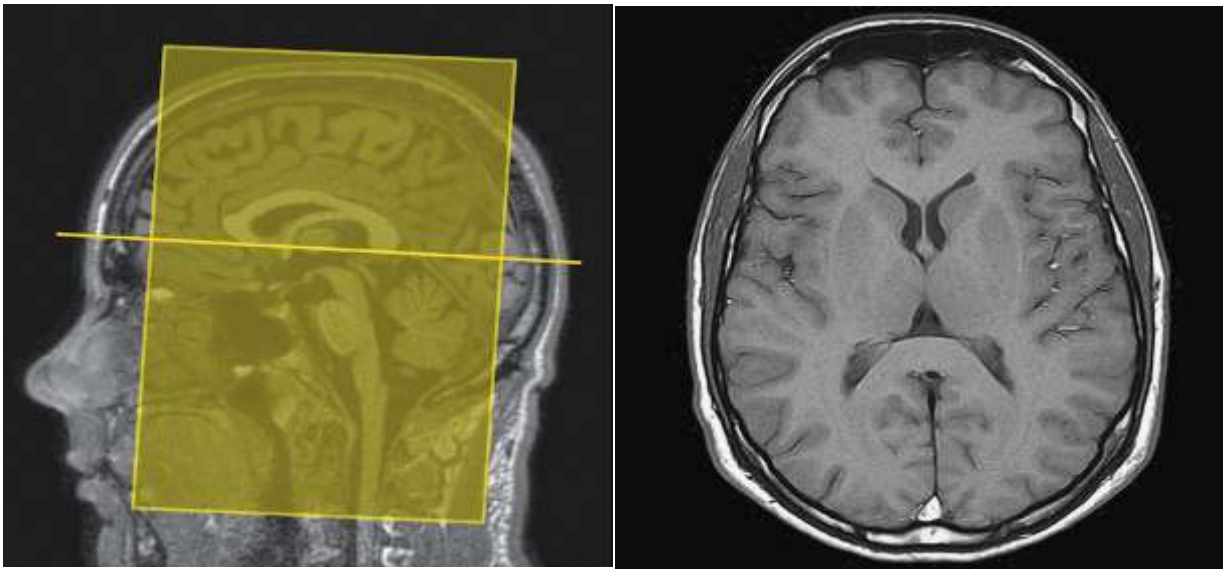

Fig. (3.2) Axial IR T1-weighted image using a TI of 700ms with the level of the cuts demonstrated in sagittal T1 weighted images (left).

Then the images prepared for the textural analysis throw DICOM viewer to select which images can be treated as IDL variable and then the processing can be achieved for classification purposes.

The following diagram showing the method of texture analysis and feature extraction programmatically performed with IDL:

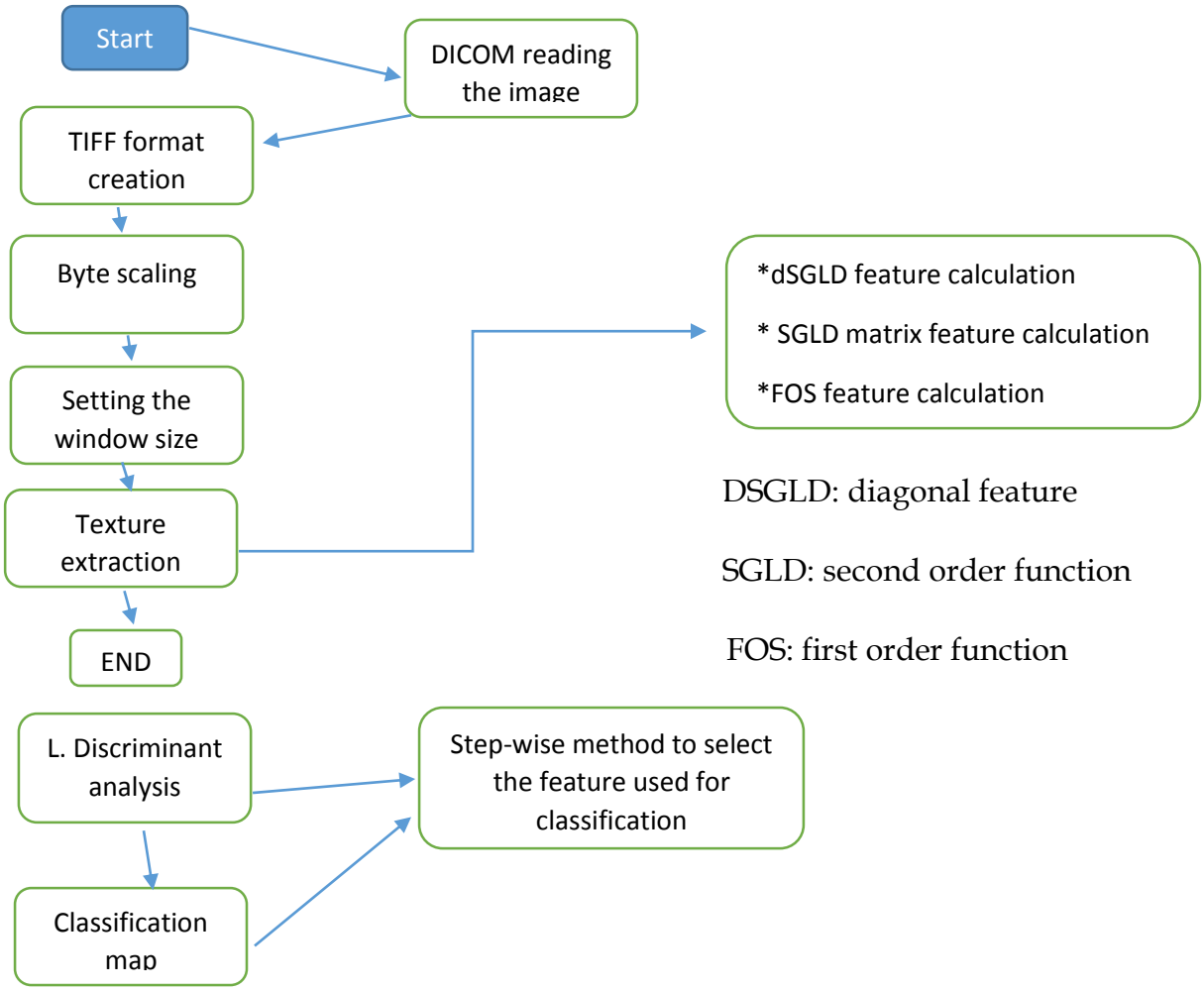

Fig. (3.3) block diagram demonstrating the steps used to classify the brain tissue using IDL.

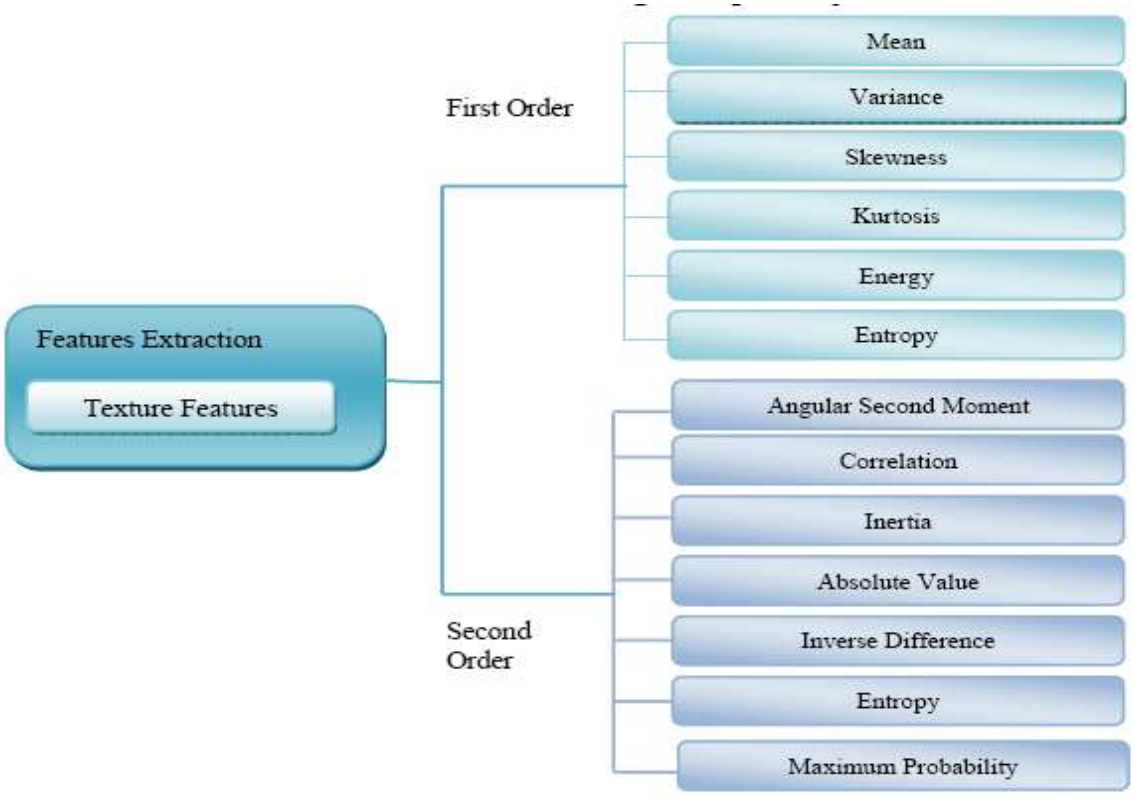

Fig. (3.4) a block diagram showed an example of extracted feature from brain images

3.2.1. Study Design:

A prospective, analytical case control study used to classify and to characterize the brain tissue in patient with brain glioma.

3.2.2. Area of the Study:

This study conducted at Khartoum state hospitals, cancer diagnostic studies and Radiation and Isotopes Center of Khartoum (RICK), Radiation Oncology Department (ROD).

3.2.3. Study Sample:

The study sample was consisted of 50 patients with brain cancer and same number of normal brain for classification purpose (control group).

3.2.4. Duration of the study:

This study conducted in period from January 2015 May 2016.

3.2.5. Population of the Study:

The population of this study was data set (brain MR Images), where the brain were free from disease for control cases and the test brain MRI images include patient diagnosed as having brain tumour. The study include both gender with their age ranged from 18 years to 83years old.

3.2.6. Inclusion Criteria:

All patient with brain cancer who have MRI scan, who have suspicion of brain glioma rather than other histological type.

3.2.7. Exclusion Criteria:

All patient with negative contrast enhancement and patient underwent a surgical procedure and those having tendency of other brain histopathological type were excluded.

3.2.8. Method of data analysis and presentation:

After that MRI images were stored in computer disk were viewed by the Radiant, Ant DICOM viewer in computer to selected the axial images that suit the criteria of research population then uploaded into the computer based software Interactive Data Language (IDL) where the DICOM image converted to TIFF format to suit IDL platform in order to preserve the quality of the image. Then the image were read by IDL in TIFF format and the user clicks on areas represents the background, grey matter, white matter, CSF and tumour in case of test group; in these areas a window 3×3, 5x5, 10x10, 15x15, and 20x20 pixel were generated and textural feature for the classes center were generated. These textural features includes FOS; (coefficient of variation, stander deviation, variance, signal, energy, and entropy), second order statistics; Inertia, Inverse Difference Mom, Correlation, Sum

Average, Sum Entropy, Difference Entropy, sum variance Difference, average, information Measure of correlation-1, information Measure of correlation-2, mean of SGLD and variance of SGLD, and diagonal feature extracted from Co-occurrence matrix (from diagonal one to 14) was used. These features were assigned as classification center used by the Euclidian distances to classify the whole image. The algorithm scans the whole image using a window; 3×3 pixels and computes the above mentioned textural features and then computes the distance (the Euclidean distance) between the calculated features during the scanning and the class's centers and assigns the window to the class with the lowest distance. Then the window interlaced one pixel and the same processes started over again till the entire image were classified and classification maps were generated. After all images were classified the data concerning the brain tissues (CSF, grey, and white matter) and tumour entered into SPSS with its classes to generate a classification score using stepwise linear discriminate analysis; to select the most discriminate features that can be used in the classification of brain tissues in MRI images. Where scatter plot using discriminate function were generated as well as classification accuracy and linear discriminate function equations to classify the brain tissues into the previous classes without segmentation process for unseen images in routine work. The delineation of brain tumour done by furthers processing of the classification using region label function to segment the brain tumour from the other classes and convert the segmented brain tumour from classification map with pseudo-color to binary image to extract (segment) the brain tumour from the whole original image. Then by applying Sobel function the outline of the binary image was generated and the spatial location of the pixels was used to delineate the brain tumor on the original image using read line.

3.2.9. Data collection variables:

All brain images was collected including all sequences in case of MRI and with –without contrast images in case of computed tomography (CT) scan. Which include the higher order

textural feature extracted using SGLD co-occurrence matrix, which are; Result: The calculated texture measures as described below (1 by 8 matrix, Double) Entropy, Energy, Inertia, Inverse Difference Moment, Correlation, Sum Average, Sum Entropy, Difference Entropy, sum variance Difference, average, information Measure of correlation 1, information Measure of correlation 2, mean of SGLD and variance of SGLD., also FOS texture (mean, energy, entropy, variance, Skewness and kurtosis) and diagonal feature exstracted from Co-ocurance matrix (from diagonal one to 14) was used.

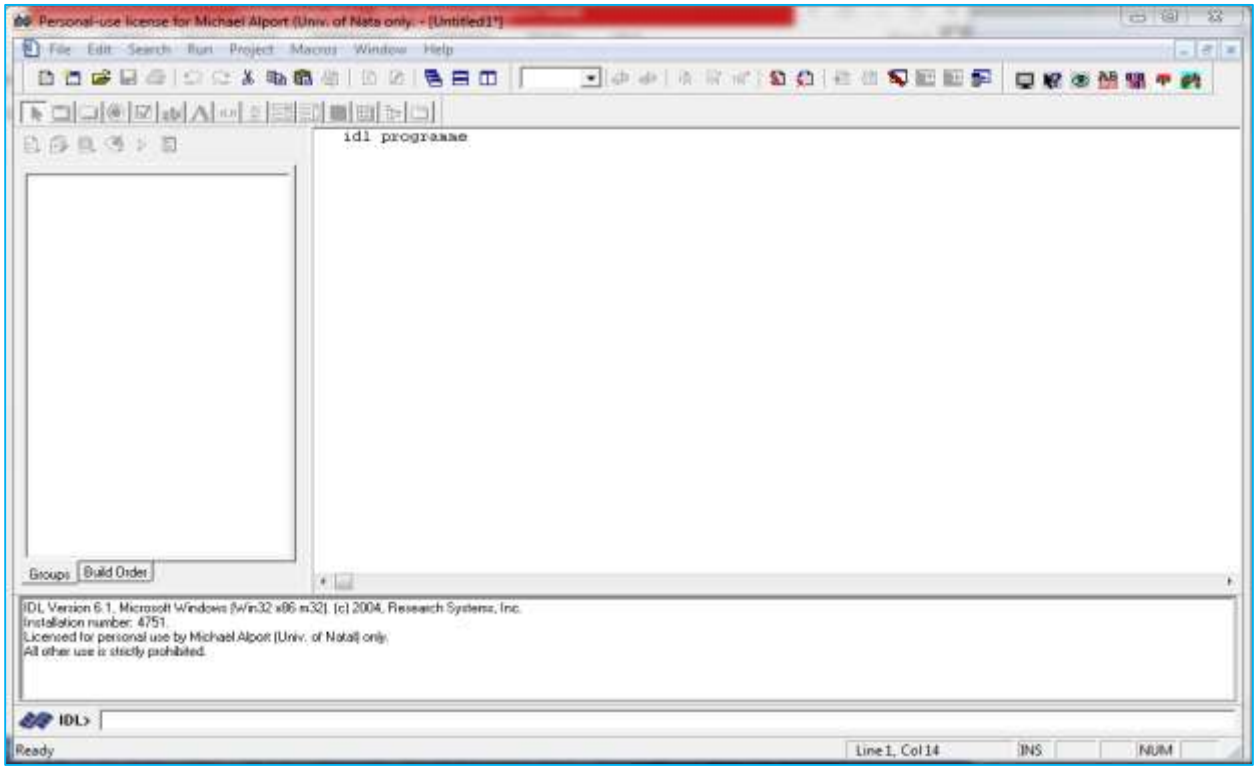

Fig. 3.5. Showed the disc-top home page for IDL image processing

3.2.10. **Ethical approval:**

- There was official written permission to Khartoum state diagnostic centers to take the data.
- No patient data will be disclose also the data was kept in personal computer with personal password.

Chapter Four

Result

This was an experimental study deals classification of brain tissue in patient with brain mass more closely related to brain glioma using image processing techniques by IDL, Interactive Data language program. The importance of this study was highlighted on evaluation of tumor extra marginal detection, increasing the diagnostic accuracy, therefore using this scans to plan patient for radiotherapy treatment and also delineation of GTV according to the intensity profile and the extracted feature.

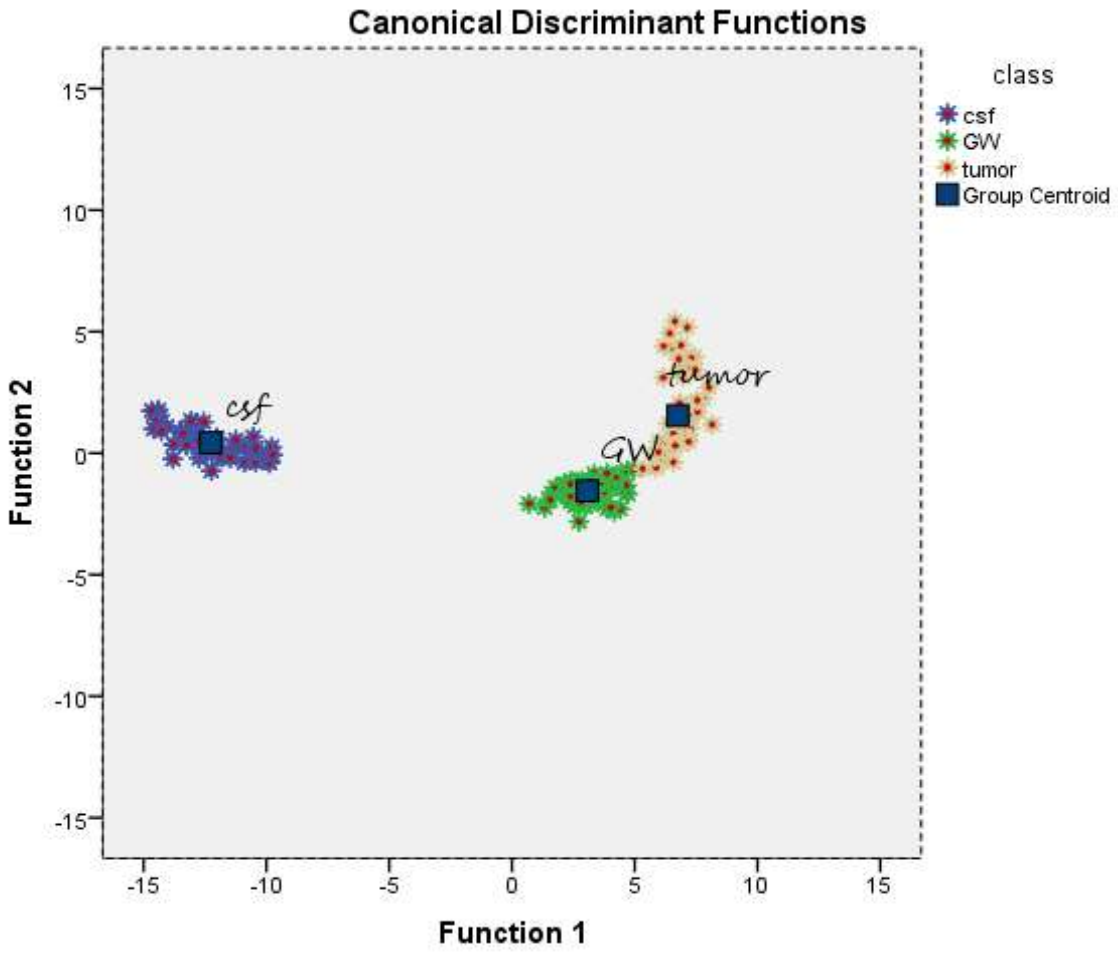

Fig 4.1. Classification scatter plot that created using linear discriminant analysis function

Table 4.1. Showed the window size related to its calcification accuracy and the test sensitivity and specificity.

Window size	Calcification accuracy	Sensitivity	Specificity
3x3	99.5	98.4%	100%
(5x5)	98.5	95.7%	100%
(10x10)	99.1	98.8%	99.3%
(15x15)	98.1	94.3%	100%
(20x20)	96.1	90.0%	98.8%

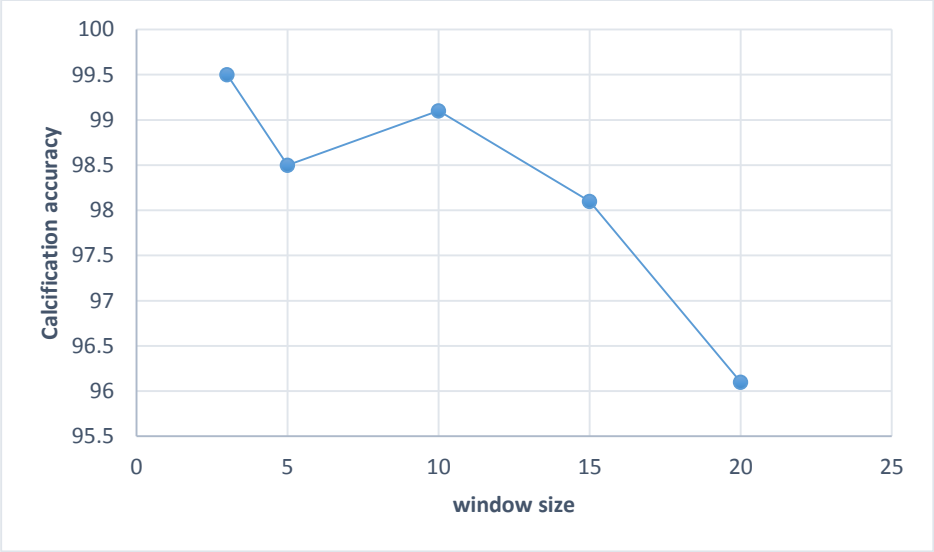

Fig 4.2. Showed the scatter plot for the window size relative to the classification accuracy of each window used for texture calculation.

Table 4.2. Showed the classification accuracy result using linear discriminant function, in which 99.5% of original grouped cases correctly classified.

Discriminant function and accuracy		Class	Predicted Group Membership			Total
			CSF	GW	Tumor	
Original	%	CSF	***100.0***	.0	0.0	100.0
		GW	0.0	***100.0***	0.0	100.0
		tumor	0.0	1.6	***98.4***	100.0
Cross-validated	%	CSF	***100.0***	.0	0.0	100.0
		GW	0.0	***98.7***	1.3	100.0
		tumor	0.0	4.7	***95.3***	100.0

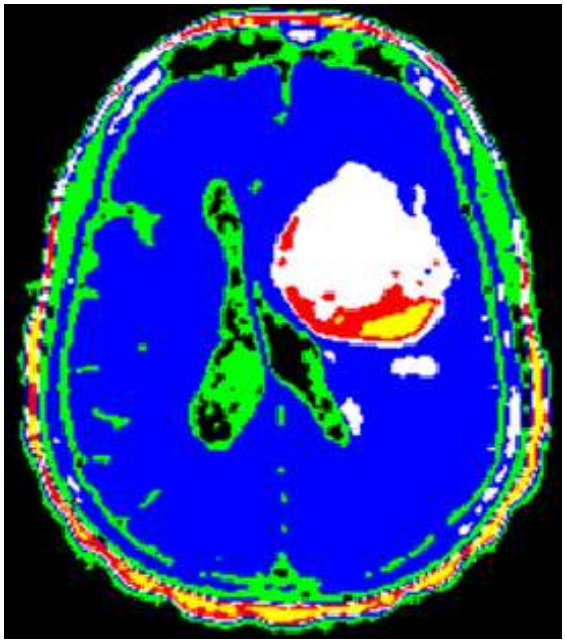

Figure 4.3. Showed the calcification map created using selected feature of each class (Brain tissue {Gray and White matter}, Brain Glioma, CSF and Bone).

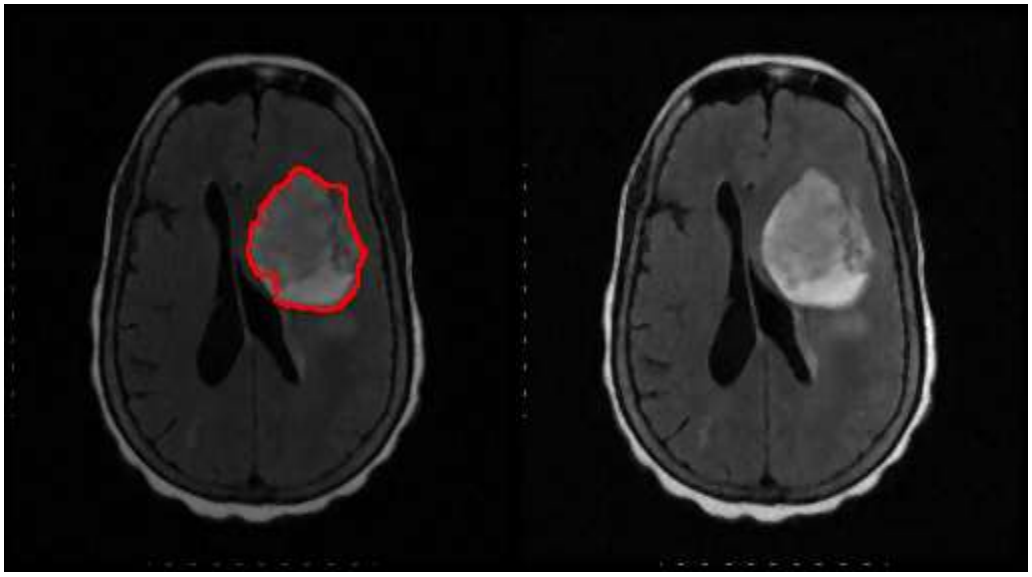

Fig 4.4. GTV of Brain Glioma Drawn at axial FLAIR images using intensity profile (left), also the volume encompasses the tumor associated edema according to (Barrette et.al (2009)).

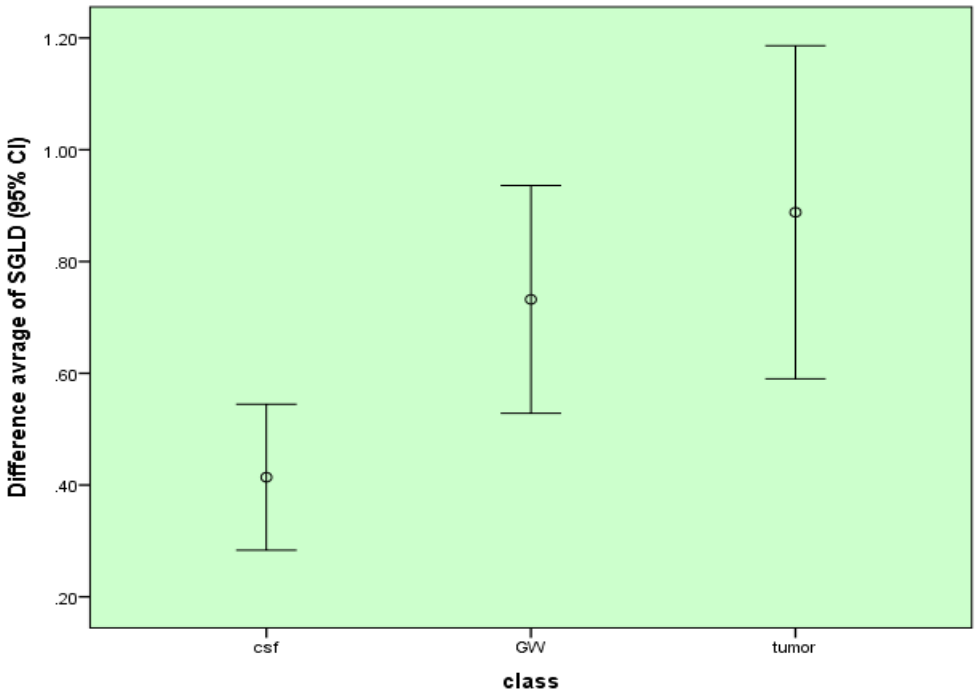

Fig 4.5. Simple error bar graph demonstrate the classification of brain tissue (gray and white matter, CSF and brain glioma) using difference average of SGLD

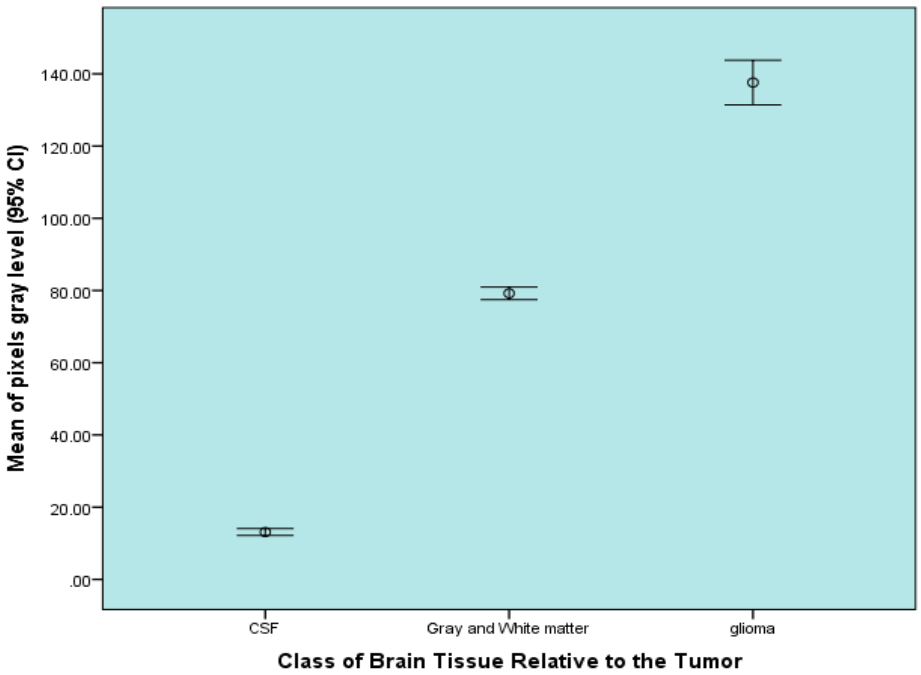

Fig 4.6. Simple error bar graph showed the classification of brain tissue (gray and white matter, CSF and brain glioma) using mean from the first order statistics.

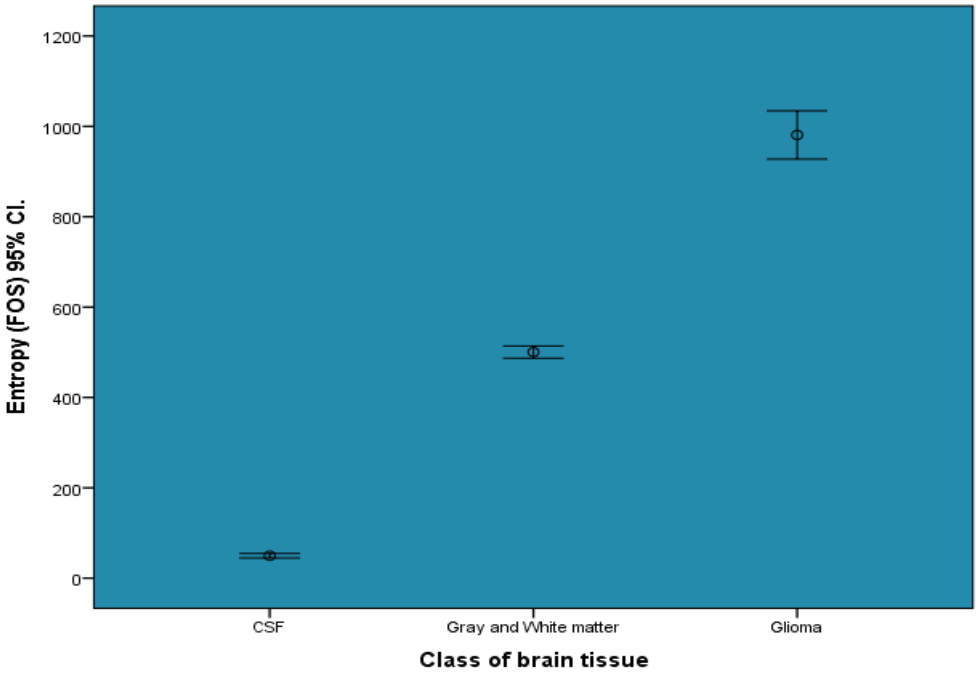

Fig 4.7. Simple error bar graph showed the classification of brain tissue (gray and white matter, CSF and brain glioma) using texture called entropy from FOS.

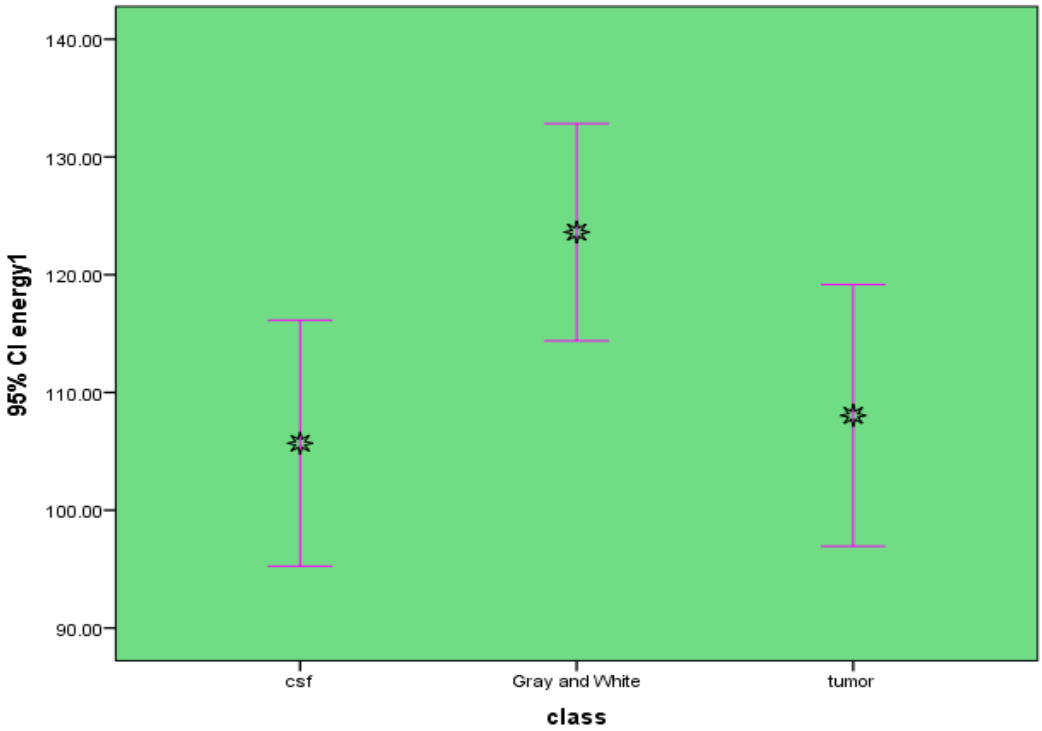

Fig 4.8. Simple error bar graph showed the classification of brain tissue (gray and white matter, CSF and brain glioma) using texture called energy from FOS.

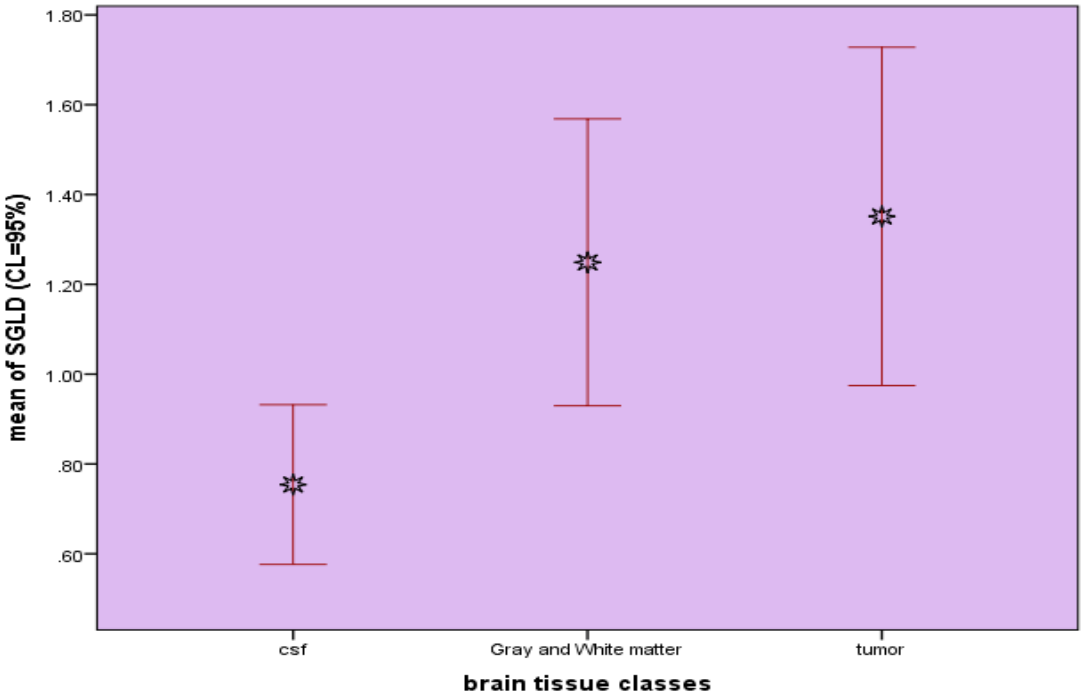

Fig 4.9. Simple error bar graph showed the classification of brain tissue (gray and white matter, CSF and brain glioma) using mean of SGLD.

Equations should be used for classification purpose:

CSF = (Difference average X 1.416) + (mean X 8.456) + (entropy X -0.993) -32.175____***Eq (1)***

Gray and white matter = (difference average X 2.532) + (mean X 23.582) + (entropy X -2.747) -

248.544 _____***Eq (2)***

Glioma = (difference average X 1.809) + (mean*25.716) + (entropy*-2.969) -315.083___***Eq (3)***

Chapter Five
Discussion, Conclusion and Recommendations

5.1 Discussion:

The main image processing disciplines in which texture analysis techniques are used are classification, segmentation and synthesis. In image classification the goal is to classify different images or image regions into distinct groups (Pietikainen, 2000). This methods are well suited to this classification purposes because they provide unique information on the texture, or spatial variation of pixels, of the region where they are applied. This study aimed to classify the brain tissue for patients with brain glioma and to identify the tumor related to its surrounding tissue using its texture feature, in order to draw the target volume for radiotherapy treatment, for the bulk of the tumor in Magnetic Resonance Images using Interactive data language program (IDL), rather than the use of visual perception of human vision: (Julesz, 1975), who was establishing authoritative data on the performance of the human vision system at discriminating certain classes of texture, in order to develop a computer image processing program that can help in brain tumor diagnosis.

Data were collected from Antalya Diagnostic Medical Center and cancer diagnostic center where the patients came to the clinic suffering from many cancer-associated morbidity which mainly include: headache, vision disturbance, sometimes with paralysis as well as associated syndromes. A successful clinical evaluation was carried out and laboratory investigation; including CBC and tumor marker were measured.

MRI has superior role on assessing brain tissue lesions rather than CT where it can be fused with CT data for purpose of radiotherapy planning as stated by barrette et.al (2009), which is the best imaging modality used to diagnose benign and malignant lesions which was performed using high

resolution SIGNA-GE MR scanner (1.5 tessla). For patient with known brain glioma, the protocol included: sagittal T1, axial T2, axial FLAIR, axial T1, coronal T2, DWI, and sagittal and axial T1 with gadolinium contrast enhancement which was used to scan and to characterize the brain glioma, then DICOM format image was extracted for all these sequences and the slices containing the tumor were selected for IDL analysis after creation of 'tiff format' IDL variable image. Then the program was written for purpose of texture calculation.

Firstly the images was displayed on gray scale manner in range of pixel values from 0 up to 255 (0 represent black region- 255 represent white region), image resizing was underwent, as well as image segmentation and background removal was took place also automatic image smoothing and filtering was done, this procedure was performed for all mentioned brain sequences, firstly in order to test which is better a histogram equalization function (where the pixels gray level was redistributed and the image sharpness and contrast increased) and we contentious with normal image enhancement and smoothing. Then the development of feature extraction program was undertaken for three type of texture feature as developed by Garelnabi et.al 2007.

Texture analysis was presented here as a useful computational method for discriminating between pathologically different regions on medical images because it has been proven to perform better than human eyesight at discriminating certain classes of texture (Julesz, 1975). Presents statistical texture analysis through first-, second-, and diagonal feature techniques. First order, second order and diagonal feature were used to calculate the texture which composed total from 34 texture extracted from the images for 6 selected brain MRI sequences in order to test which is better for classification and brain tumor characterization using different window sizes which were 3x3, 5x5, 10x10, 15x15, and 20x20 pixel window size.

These feature included: Entropy, Energy, Inertia, Inverse Difference Mom, Correlation, Sum Average, Sum Entropy, Difference Entropy, sum variance Difference, average, information Measure of correlation 1, information Measure of correlation 2, mean of SGLD and variance of SGLD., also FOS texture (mean, energy, entropy, variance, Skewness and kurtosis) and diagonal feature extracted from Co-occurrence matrix (from diagonal one to 14) were used. But the diagonal feature reveal much more similarity and it is not adequate for small window like (5x5, 3x3, 10x10) and it can be used for higher windows. These feature were calculated for four different classes which were: (brain white and gray matter, CSF, image background and brain glioma) for six sequence in selected images for every sequence.

This traditional approach has been used extensively to describe different image textures by unique features and has found application in many disparate fields such as: discrimination of terrain from aerial photographs (Conners & Harlow, 1980); in vitro classification of tissue from intravascular ultrasound (Nailon, 1997); identification of prion protein distribution in cases of Creutzfeld-Jakob disease (CJD) (Nailon & Ironside, 2000); classification of pulmonary emphysema from lung on high-resolution CT images (Uppaluri et al., 1997; Xu et al., 2004; Xu et al., 2006); and identifying normal and cancerous pathology (Karahaliou et al., 2008, Zhou et al., 2007; Yu et a., 2009). Higher-order approaches have been used to localize thrombotic tissue in the aorta (Podda, 2005) and to determine if functional vascular information found in dynamic MR sequences exists on anatomical MR sequences (Winzenrieth, 2006). The T2-weighted images revealed low classification accuracy (54.5%) of original group and it cannot give better classification for this lesion possibly due to associated edema and lipophilic nature of some tumors that interfere with classification score, from these survey looking for better sequence for characterization purpose A FLAIR images were selected and then using different sizes of windows the textures were calculated starting with 20x20; (34)

different features were underwent linear discriminant analysis with step-wise function and the test revealed that the classification accuracy was (96.1%), with (90%) sensitivity and (98.8%) specificity, four significant feature were selected for classification which are inertia, sum average of co-occurrence matrix, mean of pixel and image histogram (FOS), and energy (FOS).

Then the same process was repeated for (15x15) window and the result showed the classification accuracy equal to (98.1%), with sensitivity of (94.3%) and specificity of (100%), as demonstrated in (figure (4.2) table (4.1)). Where the most significant selected feature was; sum average of co-occurrence matrix, difference entropy, variance of SGLD, mean (FOS), skewness, kurtosis, and energy (FOS). Same process was repeated again for (10x10) window, with classification accuracy of (99.6%), sensitivity (98.1%), specificity of (99.3%), where the most selected feature were; sum entropy, mean, energy and entropy, as demonstrated in figure (4.2) table (4.1).

Also 5x5 pixel size was tested and the result showed that the classification accuracy was (98.5%), sensitivity of (95.7%), and specificity of (100%) as in figure ((4.2) table (4.1)).

Finally 3x3 pixel window revealed higher classification accuracy in this study for first order and second order statistics, where the diagonal features were excluded because of higher similarity noted within the images pixels relationship and the result showed that the classification accuracy equal to (99.5%) of original group classes was correctly classified for brain tissue and the brain glioma, with sensitivity of (98.4%) and specificity of 100% as in (figure (4.2) table (4.1)), and the most significant feature selected for classification was difference average of co- occurrence matrix, mean, and entropy from (FOS) ($p<0.05$, and CL=95%).

Figure (4.1) demonstrated the classification map created by linear discriminant analysis presented with group centroid for all images for three different classes (brain gray and white matter, brain glioma and cerebrospinal fluids) and it revealed that the brain glioma had distinct a feature rather

than the other classes. But there was small similarity noted between the glial tumor and the rest of brain tissue which is possible due to same tissue of origin and better tumor grade, which give similar signal in some instances.

A color map demonstrate each class with different color presented in figure (4.3) which was created using intensity profile function for four classes included background, for original images which were presented in figure (4.4), from this step the tumor margin and associated pre tumaral edema where clearly outlined and this can be used as GTV for radiotherapy treatment for further radiotherapy planning.

When the scattered microscopic cells don't change the signal intensity for visual perceptions but it can change the textural features (had its textural character) so that this process of outlining the marginal status of the tumor were considered more accurate from that drown by radiologist of radiation oncologist because it depend on the intensity of the received signal where the tumor irregularity was clearly and accurately outlined. From this result a simple error bar was used to demonstrate the classification result in figure (4.5). The difference average of co-occurrence matrix correlated with brain classes which differentiated the CSF form other brain tissue and tumor better than other features but there is no clear difference between the tumor and the rest of normal brain tissues. A distinct classifications were noted by the mean of the gray level of image histogram where the range of pixel value for each class was clearly separated, as in figure (4.6) same result noted for entropy from SOF which demonstrate border separation between these classes. As demonstrated in figure (4.7).

Finally this study revealed that the texture analysis method and techniques has an excellent classification properties in differentiations between the tissue of brain and brain glioma using small size pixel window because of small image dynamic range.

This study implies that 3x3 window gives a higher classification accuracy while the most significant features for classification included: Difference average of SGLD, Mean and entropy of FOS which can be used for estimation of class values by using of the following equations, which later can be developed as computer program facilitated to help in brain tumor detection and margin of GTV creation. The equations are:

5.2. Conclusion:

Brain tumors is one of the major health problem today that affect majority of both younger and adults people all over the world, this study were carried out to characterize the brain glioma in Sudanese population by introduction of new method of CAD which known as texture analysis technique which used for extracting the information from the images using different techniques using simple matrix with different sizes. Extracting the information from these matrices using textural features, which are sensitive to specific elements of texture, provides unique information on the structure of the texture being investigated. Haralick et al., proposed a set of local features specifically designed for this purpose (Haralick et al., 1973). An analytical case control study underwent MRI scan using SIGNA-GE MR scanner for 50 patient with brain glioma and 50 normal patient, in Radiation Oncology Department at Radiation and Isotopes Center of Khartoum (RICK); in period from January 2015-febriury 2016, different textural feature was extracted using (3x3, 5x5, 10x10, 15x15, 20x20) matrix window, which are FOS, SGLD feature, and diagonal feature for normal and cancerous samples, and the result showed that FOS and SGLD selected feature was used for classification using mentioned window sizes, discriminant analysis was used classify the brain tissue; the classification accuracy, sensitivity and specificity were (95.5%, 98.4% and 100%), (98.5%, 95.7% and 100%), (99.1%, 98.8% and 99.3%), (98.1%, 94.3% and 100%) and (96.1, 90.0% and 98.8%) respectively at ($P<0.05$, and CL=95%). The result showed that (3x3) having higher classification accuracy than the rest possible because of small dynamic range of useful MRI images, the feature selected for classification from 3x3 window; were difference average of SGLD, mean of gray level of image histogram, and entropy, the diff average classify the CSF while mean and entropy was give clear classification and differentiation of tumor and other brain classes.

5.3. Recommendation:

- The goal of image segmentation is a domain-independent decomposition of an image into distinct regions. Clustering concepts and image segmentation concepts have been analyzed. Image segmentation has become a very important task in today's scenario. In the present day world computer vision has become an interdisciplinary field and its applications can be found in any area. Thus, to find an appropriate segmentation algorithm and clustering algorithm based on your application and the type of inputted image is very important.
- Detection of cancer and its various type according to its textural feature may give an accurate differentiation between the tissue type and furthermore for grading and staging purposes.
- For future scope this study can be done for all type of histopathological disease of brain tumor in collaboration with the biopsy result in order to classify the textures based on the histopathology and related feature.
- Development of computer program that can be used in diagnosis of various tissue type of cancers it's quite important but that it doesn't mean forgetting the opinion of specialized persons in this filed but building up a new approaches that can help for accuracy of detection.
- Using and creation of 3D image series it's good for advance radiotherapy planning technique therefore application of texture feature for 3D images either created by the IDL or MRI or CT scanner it's quite important facilitating the process of computer planning for radiotherapy patient.

References:

Bastian, F.O. (1991). Creutzfeldt-Jakob disease and other transmissible human spongiform encephalopathies. St Louis: Mosby Year Book.

Bajscy, R. (1973). Computer description of textured surfaces, Proceedings of the Joint Conference on Artificial Intelligence, August, pp. 572-579.

Brodatz, P. (1966). Textures: a photographic album for artists and designers. Dover Publications,

ISBN 0-486-40699-7, New York.

Bruce, V.; Georgeson, M. & Green, P. (2003). Visual Perception: Psychology and Ecology.

Psychology Press Publications, ISBN 1841692387, UK.

Conners, R. & Harlow, C. (1980). Theoretical comparison of texture algorithms. IEEE Transactions on Pattern Analysis and Machine Intelligence, Vol. 2, No. 3, pp. 204-222.

Devijver, P.A. & Kittler, J. (1982). Pattern recognition: a statistical approach. Prentice Hall, 0-13-654236-0, London.

Distani, R.; Nappi, M. & Riccio, D. (2006). A range/domain approximation error-based approach for fractal image compression. IEEE Transactions on Image Processing, Vol. 15, No. 1, pp. 89-97.

Duda, R.; Hart, P. & Stork, D. (2001). Pattern Classification, John Wiley & Sons, ISBN 0-471-05669-3.

Esgiar, A.; Naguib, R.; Sharif, B.; Bennet, M. & Murray, A. (2002). Fractal analysis in the detection of colonic cancer images. IEEE Transactions on Information Technology in Biomedicine, Vol. 6, No. 1, pp 54-58.

Feder, J. (1988). Fractals. Plenum Press, ISBN 0-306-42851-2, New York. Galloway, M.M. (1975). Texture analysis using grey-level run lengths. Computer Graphics and Image Processing, Vol. 4, pp. 172-179.

Gonzalez, R.C. & Woods, R.E. (2001). Digital Image Processing, Prentice Hall, ISBN 0-201-18075-8.

Haralick, R.M.; Shanmugam K. & Dinstein, I. Texture features for image classification. IEEE Transactions on Pattern Analysis and Machine Intelligence, Vol. SMC-3, No. 6, Nov 1973, 610-621.

Hartigan, J. (1975). Clustering Algorithms. John Wiley & Sons, ISBN 0-471-35645-X. ICRU, (1999). International Commission on Radiation Units and Measurements. ICRU Report 62: Prescribing, Recording and Reporting Photon Beam Therapy (Supplement to ICRU 50), Oxford University Press.

Ironside, J.W. (1998). Neuropathological findings in new variant Creutzfeldt-Jakob disease and experimental transmission of BSE. FEMS Immunology & Medical Microbiology, Vol. 21, No. 2, pp. 91-95.

Ironside, J.W.; Head, M.W.; Bell, J.E.; McCardle, L. & Will, R.G. (2000). Laboratory diagnosis of variant Creutzfeldt-Jakob disease, Histopathology, Vol. 37, No. 1, pp. 1-9.

Jain, A.K. & Chandrasekaran. (1982). Dimensionality and sample size considerations. In: Pattern Recognition in Practice, Krishnaiah, P.R. & Kanal, L.N., Vol. 2, pp. 835-888. North Holland.

Jain, A.K. & Zongker, D. (1997). Feature selection: evaluation, application and small sample performance. IEEE Transactions on Pattern Analysis and Machine Intelligence, Vol. 2, No. 19, pp. 153-158.

Julesz, B. (1975). Experiments in the visual perception of texture. Scientific American, Vol. 232, pp 34-43.

Kachouie, N. & Fieguth, P. (2007). A medical texture local binary pattern for TRUS prostate segmentation, *Proceedings of the 29th International Conference of the IEEE Engineering and Biology Society*, Lyon, France, August 23rd – 26th.

Karahaliou, A.; Boniatis, I; Skiadopoulos, S. & Sakellaropoulos, F. (2008). Breast cancer diagnosis: analyzing texture of tissue surrounding microcalcifications. *IEEE Transactions on Information Technology in Biomedicine,* Vol. 12, No. 6, pp. 731-738.

Kovalev, V.; Kruggel, F.; Gertz, H. & von Cramon D. (2001). Three-dimensional texture analysis of MRI brain datasets. *IEEE Transactions on Medical Imaging,* Vol. 20, No. 5, pp. 424-433.

Kurani, A.; Xu, D.; Furst, J. & Raicu, D. (2004). Co-occurrence matrices for volumetric data, *Proceedings of 7th IASTED International Conference on Computer Graphics and Imaging*, Kauai, Hawaii, USA, August 17th – 19th.

Li, L. & Qi, D. (2007) Detection of cracks in computer tomography images of logs based on fractal dimension, *Proceedings of the IEEE International Conference on Automation and Logistics*, pp. 2259-2264, Jinan China, August 18th - 21st .

Mandelbrot, B.B. (1977). *Fractals: form, chance and dimension*. W.H. Freeman and Co., ISBN 0-716-70473-0, New York.

Mirmehdi, M.; Xie, X. & Suri, J. (eds) (2008). *Handbook of texture analysis,* Imperial College Press, 1-84816-115-8, UK.

Meyer, J.L. (ed) (2007). *Frontiers of radiation therapy and oncology (vol 40): IMRT, IGRT, SBRT, advances in the treatment planning and delivery of radiotherapy*, Karger, 978-3-8055-9188-9, Switzerland.

Nailon, W.H. (1997). *Tissue characterisation of intravascular ultrasound using texture analysis*. Ph.D. dissertation, The University of Edinburgh, School of Engineering.

Nailon, W.H.; Everington, D. & Ironside, J.W. (2000). *Prion protein characterisation by image analysis*. Internal communication, National CJD Surveillance Unit, Edinburgh, UK.

Nailon, W.H. & Ironside, J.W. (2000) Variant Creutzfeldt-Jakob disease: immunocytochemical studies and image analysis. *Microscopy Research & Technique*, Vol. 50, No. 1, pp. 2-9.

Nailon, W.H.; Redpath, A.T. & McLaren, D.B. (2008). Characterisation of radiotherapy planning volumes using textural analysis. *Acta Oncologica*, Vol. 47, pp. 1303-1308.

Nouza, J. (1995). On the speech feature selection problem: are dynamic features more important than static ones? *Proceedings of the European Conference on Speech Communication and Technology*, pp 917-921, Madrid, Spain, September.

Peitgen, H. & Saupe, D. (1988). *The science of fractal images.* Springer-Verlag, ISBN 0-387-96608-0, New York.

Peitgen, H.; Jurgen, H. & Saupe, D. (1992). *Chaos and fractals: new frontiers of science*. Springer-Verlag, ISBN 0-387-97903-4, New York.

Pietikainen, M.K. (ed) (2000). *Texture analysis in machine vision*, World Scientific Publishing, 981-02-4373-1, Singapore.

Pentland, P. (1984). Fractal-based description of natural scenes. *IEEE Transactions on Pattern Analysis and Machine Intelligence*, Vol. PAMI-6, No. 6, Nov, pp. 661-674.

Podda, B.; Zanetti, G. & Giachetti, A. (2005). Texture analysis for vascular segmentation from CT images, *Proceedings of Computer Assisted Radiology and Surgery (CARS)*, pp. 206-211, Berlin, Germany, 22nd-25th June, 2005.

Pratt, W.K. (1978). *Digital Image Processing*, John Wiley & Sons, 0-471-01888-0, New York.

Press, W.; Flannery, B.; Teulkolsky, S. & Vetterling, W. *Numerical recipes in C: the art of scientific computing*. Cambridge University Press, ISBN 0-521-35465-X, UK.

Russ, J.C. (1994). *Fractal surfaces*. Plenum Press, ISBN 0-306-44702-9, New York.

Sammon, J. (1969). A nonlinear mapping for data structure analysis. *IEEE Transactions on Computing*, Vol, C-18, pp. 401-409.

Steenbakkers, R.J.H.M.; Duppen, J.C.; Fitton, I.; Deurloo, K.E.I.; Zijp, L.; Uitterhoeve A.L.J.; Rodrigus P.T.R.; Kramer, G.W.P.; Bussink, J.; De Jaeger, K.; Belderbos, J.S.A.; Hart,

A.A.M.; Nowak, P.J.C.M.; van Herk, M. & Rasch, C.R.N. (2005). Observer variation in target volume delineation of lung cancer related to radiation oncologistcomputer interaction: a 'big-brother' evaluation. *Radiotherapy & Oncology,* Vol. 77, pp. 182-190.

Stearns, S.D. (1976). On selecting features for pattern classifiers. *In Proceedings of the 3rd International Conference on Pattern Recognition*, pp. 71-75, Colorado, USA.

Stoyan, D. & Stoyan, H. (1994). *Fractals, random shapes and point fields: methods of geometrica statistics*. John Wiley & Sons, ISBN 0-471-93757-6, New York.

Therrien, C.W. (1989). *Decision estimation and classification: an introduction to statistical pattern recognition and related topics*, John Wiley & Sons, 0-471-83102-6, New York.

Tuceryan, M. & Jain, A.K. (1998). Texture analysis. In: Chen, C.H; Pau, L.F. & Wang, P.S.P., (eds). *The handbook of pattern recognition and computer vision*. 2nd ed. World Scientific Publishing Co., ISBN 9-810-23071-0, Singapore.

Turcotte, D.L. (1992). *Fractals and Chaos in Geology and Geophysics*, Cambridge University Press, ISBN 0-521-56164-7, Cambridge, UK.

Uppaluri, R.; Mitsa, T.; Sonka, M.; Hoffman, E. & McLennan G. (1997). Quantification of pulmonary emphysema from lung computed tomography images. *American Journal of Respiratory Care in Medicine*, Vol. 156, No. 1, pp. 248-254.

Weber, A.G. (2004). The USC texture mosaics. *University of Southern California Viterbi School of Engineering*, http://sipi.usc.edu/ .

Weltons, C.; Menten, J.; Feron, M.; Bellon, E.; Demaerel, P.; Maes, F.; van den Bogaert, W. & van der Schueren, E. (2001). Interobserver variations in gross tumor volume delineation of brain tumours on CT and impact of MRI. Radiotherapy & Oncology, Vol. 60, No. 1, pp. 49-59.

Winzenrieth, R. & Claude, I. (2006). Is there functional vascular information in anatomical MR sequences? A preliminary in vivo study. *IEEE Transactions on Biomedical Engineering*, Vol. 53, No. 6, June 2006, pp.1190-1194.

Xu, D.; Kurani, A. & Raicu, D. (2004). Run-length encoding for volumetric texture, *Proceedings of 4th IASTED International Conference on Visualization, Imaging and Image Processing – VIIP*, Marbella, Spain, September 6th – 8th.

Xu, Y.; Sonka, G.; McLennan, G.; Junfeng, G. & Hoffman, E. (2006). MDCT-based 3D texture classification of emphysema and early smoking related pathologies. *IEEE Transactions on Medical Imaging*, Vol. 25, No. 4, pp. 464-475.

Yu, H.; Caldwell, C.; Mah, K. & Mozeg D. (2009). Co-registered FDG PET/CT based textural characterization of head and neck cancer in radiation treatment planning. *IEEE Transactions on Medical Imaging*, Vol. 28, No. 3, pp. 374-383.

Yu, Z.; Jixian, Z. & Haitao, L. (2007). Fractal characteristics of very high resolution satellite imagery, *Proceedings of Geoscience and Remote Sensing Symposium*, pp. 389-92, Barcelona, Spain, July 23rd-27th.

Zhou, B.; Xuan, J.; Zhao, H.; Chepko, M.; Freedman, M. & Yingyin, K. (2007). Polarization imaging for breast cancer diagnosis using texture analysis and svm, Proceedings of Life Sciences Systems and Applications Workshop, pp. 217-220, Bethesda, Maryland, USA.

Zonger, D. & Jain, A. (1996). Algorithms for feature selection: an evaluation. *Proceedings of the 13th International Conference on Pattern Recognition (ICPR'96)*, Vol. B, pp. 18-22, Vienna, Austria, August.

Appendix (A):

Table 5.1. Showed the calculated feature using 3x3 pixels window:

entropy	energy	enertia	IDM	correlation	sum avarage	sum entropy	difference entropy	sum variance	diff avrage
2.99145	0.14875	0.4	0.66	0.629791	1.9	1.83932	1.15486	2.068	0.3
3.23935	0.1625	9.05	0.636729	0.14488	6.55	2.62326	1.65485	12.2024	1.65
3.68418	0.0975	10.1	0.540362	0.256388	5.7	2.72535	1.90712	17.9855	1.9
3.82193	0.0875	3	0.585882	0.783405	12.6	2.85199	1.82877	27.364	1
3.36596	0.1225	0.75	0.605	0.559421	3.15	2.03932	1.32109	3.443	0.45
3.36596	0.1225	0.95	0.615	0.468824	3.45	2.07493	1.37493	3.46212	0.55
3.32193	0.12	6	0.498585	0.070244	2.8	1.99815	1.64717	7.384	1.4
3.3087	0.1425	8.15	0.47622	0.31267	8.95	1.61767	1.06669	28.4065	0.95
3.3087	0.1425	1.2	0.712941	0.642902	5.9	2.5765	1.33876	6.109	0.5
3.43418	0.10875	3.4	0.571765	0.359921	5.1	2.03932	1.15486	8.588	0.9
3.6087	0.0925	1.25	0.685	0.445558	3.15	2.6926	1.36229	3.43138	0.65
2.51997	0.2525	0.55	0.795	0.664765	3.65	2.00388	1.10294	2.76137	0.35
2.80161	0.185	0.6	0.72	0.401305	2.5	1.82668	1.23876	1.525	0.4
3.73418	0.08375	2.3	0.49	0.407617	3.5	2.65754	1.65754	5.6	0.9
3.58418	0.1025	3.05	0.664864	0.464692	5.45	2.67151	1.53876	9.37725	0.85
3.34145	0.1325	2	0.572941	0.345994	4.3	2.09658	1.59658	4.612	0.7
3.12193	0.1925	1.4	0.63	0.459589	6.2	1.87364	1.47095	7.194	0.6
3.23418	0.12875	0.95	0.625	0.724324	2.75	2.2198	1.35486	6.275	0.45
3.43418	0.10875	1.45	0.515	0.650643	4.35	2.28761	1.26114	10.4507	0.55
3.67193	0.09375	4.65	0.614729	0.259906	5.95	2.68974	1.68705	8.50725	1.15
3.68418	0.0925	1.8	0.301351	0.553634	3.9	1.31267	0.737186	29.1035	0.3
3.44644	0.1325	1.4	0.532941	0.390742	3.9	1.70503	1.12664	7.627	0.5
3.74644	0.0825	2.7	0.515882	0.524399	5.1	2.58205	1.65754	10.088	0.9
3.23935	0.1625	2.7	0.603846	0.482127	4.5	2.17497	1.29658	12.2	0.7
3.62193	0.0975	3	0.54	0.567325	4.9	2.68974	1.58778	10.989	1.1
2.74546	0.23875	0.95	0.625	0.394713	2.25	1.73108	1.35486	2.275	0.45
3.05161	0.16875	1.85	0.635	0.287441	1.75	2.26942	1.5493	3.68125	0.75
3.54644	0.0975	4.35	0.398846	0.171875	3.35	2.08761	1.54278	7.56075	1.15
3.74644	0.0825	2.7	0.515882	0.524399	5.1	2.58205	1.65754	10.088	0.9
4.02193	0.0675	16.95	0.514693	0.248652	9.15	2.77364	1.71267	32.8691	2.25
3.68418	0.0975	1.95	0.635	0.649485	6.35	2.72535	1.70712	9.81137	0.85
3.54145	0.1125	0.85	0.615	0.713203	5.45	2.47706	1.39658	8.007	0.45
3.09644	0.15875	0.9	0.69	0.41469	3.7	1.83876	1.23876	2.241	0.5
2.79546	0.2375	1.3	0.626923	0.612333	6.1	1.49888	0.874372	10.327	0.3
3.82193	0.0775	2.5	0.545882	0.500211	8.1	2.67364	1.64717	12.2485	0.9
3.48418	0.1075	1.8	0.55	0.608534	3.7	2.33589	1.64717	9.0565	0.8

3.24644	0.1175	0.8	0.54	0.553885	4.4	2.04986	0.964386	10.032	0.4
3.33418	0.11375	2.35	0.661923	0.385278	10.25	2.55199	1.48705	6.58125	0.75
3.74644	0.0825	3.4	0.458824	0.273508	5.7	1.95883	1.43932	6.812	1.1
3.52193	0.1125	3.25	0.468846	0.524606	4.65	2.18761	1.62535	12.9408	0.85
3.92193	0.07	0.9	0.49	0.410455	2.9	2.08761	1.32535	4.767	0.5
3.54145	0.1125	6.5	0.401538	0.492222	4.9	1.73932	1.19449	26.4855	0.9
3.3087	0.1425	0.65	0.555	0.725452	5.25	1.91212	1.12664	8.21875	0.35
3.42193	0.115	0.9	0.59	0.734823	5.3	2.35754	1.29658	9.192	0.5
2.77821	0.18375	0.25	0.775	0.619803	1.45	2.09602	0.903967	1.53725	0.25
3.73418	0.08375	0.8	0.58	0.554577	2.1	2.28205	1.39333	3.108	0.5
2.53418	0.22375	1.8	0.37	0.194658	1.5	1.53932	0.994486	2.7375	0.6
3.67193	0.09375	2.1	0.63	0.465032	4.4	2.75199	1.48705	6.404	0.8
3.82193	0.0875	0.75	0.505	0.684718	4.45	2.32535	1.34986	8.20675	0.45
2.89546	0.2325	0.45	0.735	0.636137	4.25	2.02552	1.15828	2.38125	0.35
3.74644	0.0875	6	0.512	0.547006	6.8	2.58205	1.65754	23.112	1.2
3.87193	0.07375	23.9	0.504742	0.570931	16.4	2.87364	1.84717	105.596	2.7
4.02193	0.0675	42.9	0.546491	0.476074	18	3.18974	1.92877	127.5	3.5
3.88418	0.0775	5.95	0.42061	0.517871	9.65	2.42535	1.54278	25.0908	1.15
3.88418	0.0775	15.8	0.535805	0.556135	9.3	3.05199	1.92877	56.461	2.3
4.02193	0.0675	13.95	0.417712	0.43609	13.15	2.52535	1.48761	47.3507	1.85
3.88418	0.0775	10.6	0.469252	0.421596	15	2.53589	1.64717	31.85	2
4.02193	0.0675	30.6	0.513505	0.53766	15	2.77364	1.51267	128.05	2.7
3.82193	0.0775	10.15	0.522538	0.175121	13.85	2.98974	1.45328	16.9453	1.95
3.88418	0.0775	19.65	0.412341	0.430688	12.05	2.14487	1.62535	58.2868	2.15
3.0537	0.14375	1.5	0.59	0.306954	2.2	2.03932	1.21711	3.292	0.6
4.02193	0.0675	10.2	0.544344	0.645485	11.2	3.18974	1.92877	50.016	1.8
3.82193	0.0875	2.75	0.528846	0.610037	4.05	2.44145	1.36096	12.8469	0.75
3.88418	0.0775	4.8	0.546787	0.639252	8.5	2.91425	1.79103	22.525	1.3
3.73418	0.08375	6.8	0.47108	0.534108	8.5	2.6198	1.73108	25.7	1.5
3.02193	0.1975	2	0.611351	0.704121	10.8	1.72535	0.874372	62.368	0.4
3.67193	0.08375	9.65	0.456405	0.397776	8.95	1.94986	1.19888	29.1167	1.55
3.72193	0.0925	17.65	0.526459	0.49114	9.65	2.18761	1.26439	64.9908	1.65
3.53418	0.09375	1.35	0.465	0.630802	4.65	1.95541	0.928946	22.6785	0.45
3.68418	0.0975	13.3	0.429421	0.183502	11.5	2.20157	1.85754	22.6	2.1
3.24644	0.1425	0.85	0.327941	0.482067	2.15	1.52877	0.953283	10.054	0.25
3.44644	0.1325	5.3	0.58267	0.707282	10.3	2.61425	1.5493	32.201	1.3
3.54644	0.1075	0.65	0.495	0.607654	2.45	2.08761	1.36229	3.44675	0.45
3.10161	0.1725	0.9	0.46	0.416589	3.4	1.19449	0.850594	6.738	0.3
3.72193	0.0925	2.25	0.567941	0.833318	9.55	2.65754	1.45883	27.607	0.75
3.34644	0.135	2.4	0.595882	0.665092	3.9	2.19815	1.27095	21.1085	0.8
3.49145	0.11375	1.7	0.35	0.493864	3.3	1.79316	1.31767	6.854	0.7

3.29644	0.13875	1.1	0.71	0.710487	3.9	2.51425	1.23876	6.769	0.5
3.78418	0.08	10.3	0.524703	0.722566	17.5	2.95199	1.62877	95.825	1.9
3.58418	0.1025	4.25	0.457703	0.454995	4.35	2.22535	1.48761	11.8507	0.95
3.58418	0.1025	1.3	0.72	0.742743	4.7	2.83034	1.45485	10.7055	0.6
3.88418	0.0775	2.4	0.4	0.591846	5.9	2.42535	1.40503	12.347	0.9
3.82193	0.0875	4.9	0.458688	0.585962	6.2	2.65754	1.75754	19.772	1.3
2.21997	0.3025	0.85	0.527941	0.00288	0.35	1.16669	0.932193	0.8785	0.25
3.19145	0.13875	0.85	0.575	0.628612	5.65	1.84487	1.02266	8.75075	0.35
3.62193	0.0975	0.9	0.63	0.754466	9	2.48974	1.45004	8.6	0.6
2.63418	0.21875	0.45	0.695	0.770383	1.65	1.8198	0.952257	4.383	0.25
2.80161	0.185	0.4	0.47	0.10424	0.4	0.994486	0.850594	0.568	0.2
3.82193	0.0775	4.75	0.540882	0.460657	5.25	3.10583	1.36229	15.2094	1.45
3.92193	0.07	1.9	0.47	0.700525	6.6	2.42535	1.32535	21.072	0.7
3.82193	0.0875	5.8	0.542703	0.31307	3.8	2.85199	1.62877	11.316	1.4
2.64644	0.19	0.1	0.65	0.821149	2.3	1.64986	0.774372	4.023	0.1
3.14644	0.1575	0.9	0.552941	0.573527	3.5	1.69602	1.04829	4.7625	0.3
4.02193	0.0675	4.55	0.458846	0.353906	8.85	2.7198	1.75754	12.163	1.25
3.88418	0.0775	2.4	0.492941	0.265226	4.3	2.15754	1.8198	4.612	0.9
2.98418	0.2025	2.05	0.650882	0.653296	5.75	2.03589	1.32266	12.6281	0.65
3.44644	0.1325	3.95	0.627805	0.720841	8.85	2.71425	1.53876	30.3953	1.05
3.82193	0.0875	7.5	0.558923	0.533742	7.5	2.71425	1.92877	25.425	1.5
3.68418	0.0875	1.5	0.63	0.839689	7.9	2.85199	1.62877	18.449	0.7
3.1587	0.14875	0.8	0.54	0.416598	1.4	1.64986	0.964386	3.452	0.4
3.82193	0.0875	4.95	0.460644	0.634095	11.75	2.18761	1.62535	40.8688	1.05
2.99644	0.16375	1.7	0.755882	0.477057	2.9	1.98974	1.02459	4.849	0.5
3.78418	0.08	3.3	0.461765	0.546413	6.9	2.28761	1.32535	30.207	0.9
3.44145	0.1175	1.4	0.52	0.477136	4.3	2.27706	1.6198	5.012	0.7
3.52193	0.1	1.1	0.61	0.395532	1.9	2.25754	1.29658	3.168	0.5
3.49145	0.11375	2.3	0.535882	0.073395	4.6	1.76383	1.59333	3.308	0.8
3.18418	0.1325	0.3	0.46	0.622099	2.4	1.63932	1.07706	3.948	0.2
3.72193	0.0925	6.25	0.515634	0.24784	5.65	2.5198	1.39658	11.543	1.35
3.68418	0.0875	5.1	0.42267	0.207272	3.4	2.00712	1.48761	8.472	1.2
3.53418	0.09375	2.5	0.465882	0.36397	2.8	2.07151	1.18279	8.916	0.7
3.67193	0.09375	4.25	0.588846	0.701253	8.75	2.68974	1.5493	33.2313	1.15
3.42193	0.1175	4.25	0.528846	0.342395	3.15	2.48974	1.86327	9.73525	1.25
3.48418	0.1075	2.65	0.395	0.138241	3.05	2.02535	1.36229	3.95675	0.95
2.41387	0.21875	0.2	0.46	0.615165	1.5	1.07839	0.734498	2.425	0.1
3.26596	0.1275	2.65	0.640882	0.356147	7.15	2.29103	1.40101	6.61525	0.85
3.12193	0.13	0.5	0.47	0.444787	0.9	1.59316	1.19316	1.366	0.3
3.33418	0.11375	0.3	0.7	0.837103	5.5	2.33589	0.995463	9.5125	0.3
3.88418	0.0775	2.55	0.570882	0.336283	3.55	2.55199	1.72552	5.28725	0.95

2.77095	0.2	0.5	0.47	0.647239	3.7	1.61767	1.19316	9.334	0.3
3.3087	0.1425	0.5	0.52	0.652042	3.1	1.53376	1.18279	3.5265	0.3
3.02193	0.1975	2.05	0.604864	0.581239	11.25	1.72535	0.874372	48.7187	0.45
3.68418	0.0875	3.05	0.464864	0.551598	7.85	2.38761	1.62535	25.3407	0.85
3.58418	0.1025	3.1	0.583846	0.560161	4.5	2.38205	1.45883	12.2	0.8
3.68418	0.0875	2.75	0.438846	0.3862	3.55	2.05541	1.29316	10.5065	0.65
2.78418	0.2125	3.35	0.668846	-0.03392	1.75	1.98761	1.45485	3.13438	0.95
2.31904	0.2625	0.85	0.375	0.482717	2.65	1.07839	1.07839	4.11625	0.35
2.99644	0.14375	1.2	0.61	0.263063	1.4	1.99815	1.37168	2.146	0.6
3.73418	0.08375	4.25	0.557703	0.39646	9.75	2.48205	1.53108	11.975	0.95
3.44644	0.1325	1.9	0.365882	0.684039	4.2	1.97706	1.40157	20.322	0.6
3.03935	0.1725	0.3	0.7	0.845891	4.8	1.99106	0.995463	17.204	0.3
3.82193	0.0775	4.05	0.465769	0.674604	8.75	2.38761	1.48761	54.3188	0.95
3.64145	0.1075	3	0.496	0.335338	10.7	2.00712	1.48761	19.563	0.7
3.88418	0.0775	14	0.51322	0.72005	19.8	2.73589	1.84717	139.154	2
3.74644	0.0875	6.65	0.429824	0.51641	11.05	2.58205	1.6198	29.927	1.55
3.54145	0.11	13.8	0.603693	0.508712	13.3	2.70925	1.62877	45.821	1.8
3.88418	0.0775	15.85	0.561625	0.592528	21.15	2.83034	1.84487	63.5614	2.35
3.82193	0.0775	3.25	0.468846	0.712422	18.35	2.52535	1.62535	166.111	0.85
3.82193	0.0875	2.75	0.476351	0.533277	8.15	2.18761	1.62535	24.8007	0.75
4.02193	0.0675	17.25	0.559417	0.83847	24.85	3.18974	1.92877	209.975	2.25
3.14644	0.1575	2.9	0.723846	0.861559	13.9	2.51425	1.02459	41.169	0.7
3.47193	0.10375	2.2	0.625882	0.609079	6	2.38974	1.62877	10.6	0.8
3.24644	0.1425	2	0.665882	0.753595	5.1	2.2765	1.48705	17.789	0.7
3.03935	0.1725	2.1	0.535882	0.346899	2.5	1.84278	1.26439	7.375	0.6
3.49145	0.11375	6.55	0.623703	0.497268	5.45	2.70925	1.68705	22.8772	1.25
3.72193	0.0925	1.9	0.712941	0.723194	5.1	3.10583	1.45485	25.3895	0.7
3.78418	0.08	7.3	0.471493	0.436944	9.6	2.73589	1.37168	22.716	1.7
3.82193	0.0775	4.3	0.509729	0.748538	15.1	2.65754	1.65754	81.888	1.1
3.52193	0.1	5.9	0.562	0.79055	13.5	2.45754	1.49658	99.2	1.1
2.51096	0.28375	0.05	0.675	0.257842	0.95	1.26439	0.620064	5.47675	0.05
2.82193	0.205	0.5	0.67	0.816054	4.3	1.85754	1.10656	7.912	0.3
4.02193	0.0675	1.95	0.585	0.7181	5.95	3.08974	1.72552	20.8072	0.85
3.02193	0.1975	1.15	0.645	0.573023	2.45	1.83108	1.20657	4.347	0.45
3.3087	0.1425	2.1	0.575882	0.267355	4.5	2.00157	1.49658	4.4	0.7
3.23418	0.12875	0.2	0.55	0.671887	1.5	1.87151	0.982787	1.7625	0.2
3.34145	0.1325	1.4	0.672941	0.457386	4.6	2.32877	1.48705	4.124	0.6
3.29145	0.13375	2.8	0.625882	0.470553	4.3	2.37151	1.68705	8.461	0.9
2.98418	0.2025	1.15	0.685	0.370156	4.35	1.89103	1.40101	2.73525	0.55
3.34644	0.135	1.4	0.63	0.520711	6	2.19815	1.47095	6.8	0.6
2.36096	0.29	0.1	0.25	0.481183	0.8	1.09658	0.796578	2.812	0.1

2.92821	0.15	0.7	0.57	0.359732	3.8	1.76383	1.38205	1.972	0.5
3.04644	0.1625	2.5	0.646923	0.691004	11.4	2.31425	1.33876	16.544	0.8
1.91664	0.4425	0.6	0.83	0.58106	3.5	1.50055	0.668087	2.9375	0.3
3.72193	0.0925	3.65	0.648846	0.666906	9.75	2.98974	1.53876	27.8813	0.95
2.26924	0.33375	0.2	0.66	0.577181	2.5	0.884918	0.620064	1.275	0.1
3.53418	0.10375	1.05	0.535	0.829495	8.55	2.08761	1.26114	40.6167	0.45
4.02193	0.0675	3.55	0.478846	0.707253	9.15	2.5198	1.57706	35.283	1.05
2.27095	0.3775	0.55	0.795	0.636488	2.75	1.75485	1.10294	3.60938	0.35
3.72193	0.0925	2.4	0.6	0.765574	5.3	2.75199	1.3493	19.901	0.9
2.9537	0.14875	0.55	0.645	0.322429	1.95	1.73722	1.21711	1.387	0.35
2.29644	0.26875	0.45	0.495	0.906333	3.15	1.61767	1.06669	9.1585	0.25
4.02193	0.0675	18.95	0.515344	0.759781	20.45	3.30583	1.90712	242.837	2.75
3.72193	0.0925	6.55	0.601549	0.796353	13.85	2.88974	1.68705	165.945	1.35
3.88418	0.0775	49.8	0.56428	0.352737	24.4	2.91425	1.79103	116.904	3.2
3.44644	0.1325	6.55	0.651549	0.841189	14.35	2.83034	1.65485	215.731	1.35
3.82193	0.0875	26.15	0.53463	0.687957	20.55	3.10583	2.04487	180.532	3.15
3.88418	0.0775	21.05	0.48564	0.42076	18.15	2.95199	2.06327	56.0852	2.85
3.47193	0.10375	18.35	0.464362	0.558204	13.05	2.35754	1.53108	73.387	2.35
3.44644	0.1325	5.3	0.626652	0.306483	9.7	2.41425	1.68705	11.001	1.1
3.87193	0.07375	5.5	0.618585	0.869661	16.6	3.08974	1.68705	89.584	1.2
3.82193	0.0875	18.95	0.465344	0.68552	23.05	2.88974	1.92552	167.517	2.75
4.02193	0.0675	136.2	0.501443	0.447374	32	3.05199	1.62877	397.2	7.2
4.02193	0.0675	119.7	0.501954	0.426449	26.9	3.16809	1.84487	320.51	7.2
4.02193	0.0675	134.25	0.503335	0.259124	18.85	3.10583	2.04487	233.361	7.15
4.02193	0.0675	104.15	0.504169	0.334381	16.45	2.91425	1.92877	210.887	5.65
4.02193	0.0675	102.05	0.50212	0.405742	30.75	2.98974	1.92877	260.731	6.15
3.29145	0.12375	32.55	0.460799	-0.12179	4.25	2.04487	1.39888	27.0688	2.45
3.17095	0.1475	1.5	0.69	0.860315	7.6	2.43876	1.26327	37.764	0.6
3.88418	0.0775	5.15	0.573941	0.739298	13.65	2.91425	1.72877	60.1953	1.25
3.88418	0.0775	8.6	0.543765	0.522044	9.9	2.91425	1.72877	32.989	1.7
4.02193	0.0675	102.05	0.50212	0.405742	30.75	2.98974	1.92877	260.731	6.15
3.15869	0.14875	0.9	0.702941	0.706859	8.9	2.14431	0.952257	10.648	0.3
3.13418	0.13375	0.8	0.352941	0.301715	3.4	1.09103	0.746197	11.904	0.2
3.34644	0.1175	1.3	0.56	0.343693	2.6	1.99106	1.37168	2.926	0.7
3.54644	0.1075	1.85	0.435	0.231626	4.05	2.08761	1.60503	4.12675	0.75
3.10161	0.1725	2.75	0.655	0.473159	8.95	2.48551	1.17937	8.04237	0.95
3.72193	0.0925	54.6	0.504668	0.641824	41.3	2.65754	1.59658	282.772	3.7
3.62193	0.0975	27.9	0.504342	0.13632	14.1	2.47364	1.64717	39.2685	2.9
2.77193	0.20875	0.25	0.775	0.827622	2.85	2.08974	0.903967	2.91525	0.25
2.83418	0.20875	0.3	0.31	0.563934	1	1.29103	1.04829	1.9	0.2
3.3087	0.1425	0.3	0.61	0.740566	1.4	1.81212	1.02266	2.952	0.2

Continue…..

mean SGLD	VAR SGLD	mean 1	variance 1	shkwness	kurtosis	energy 1	entropy 1	class
0.95	0.785493	11.52	1.84333	0.5829	-0.76874	134.48	40.7290	1
3.275	2.30502	12.56	6.84	0.464691	-0.9625	92.64	46.2235	1
2.85	2.64979	11.88	15.5267	1.3646	2.41546	94.6	43.2414	1
6.3	2.75518	15.76	15.8567	0.49688	0.240831	79.28	63.3856	1
1.575	1.02384	10.64	3.32333	0.517012	-0.43105	116.4	36.5099	1
1.725	1.05025	10.56	2.92333	0.478094	-0.18363	114.32	36.0985	1
1.4	1.82921	10.88	8.02667	0.581151	-1.1381	95.36	37.9602	1
4.475	3.0231	13.36	10.1567	-1.13125	1.22779	126.8	50.575	1
2.95	1.35176	11.6	2.16667	-0.75253	0.625051	136.64	41.1534	1
2.55	1.73118	10.56	4.25667	-0.62863	-1.02093	115.6	36.2051	1
1.575	1.08182	7.84	1.39	-0.14364	-1.23833	62.8	23.4161	1
1.825	0.909859	7.04	1.29	-0.07417	0.632893	50.8	19.9511	1
1.25	0.728869	6.52	0.76	-0.42077	-0.77865	43.24	17.7187	1
1.75	1.40535	7.72	3.04333	-0.30964	-1.36552	62.52	23.0473	1
2.725	1.76262	10.44	4.50667	-0.25881	-0.96875	113.32	35.6386	1
2.15	1.28569	14.36	4.40667	0.577754	-0.77135	149	55.4076	1
3.1	1.46578	10.92	5.91	0.556964	0.005683	104.44	38.0297	1
1.375	1.34397	9.2	3.25	0.286738	-1.35403	87.76	29.6975	1
2.175	1.72487	9.44	7.17333	-0.15486	-0.99522	96	31.1258	1
2.975	1.81365	10.8	4.33333	-0.43634	-1.00343	120.8	37.366	1
1.95	2.77955	16.92	6.66	-1.46532	1.42639	77.64	69.3449	1
1.95	1.50225	15.84	7.05667	0.280375	-1.26489	104.08	63.4363	1
2.55	1.78802	7.84	5.22333	-0.23363	-0.99129	66.48	23.7804	1
2.25	1.93003	9.68	7.56	0.621558	-1.41711	100.96	32.2202	1
2.45	1.87009	11.28	5.54333	0.339267	-0.66174	112.08	39.7691	1
1.125	0.897914	12.16	3.89	1.00666	-0.48331	110.64	44.0367	1
0.875	1.17593	12.4	2.83333	0.744778	-0.8674	136	45.1938	1
1.675	1.7256	11.36	5.07333	-0.34888	-1.31317	133.92	40.1476	1
2.55	1.78802	7.84	5.22333	-0.23363	-0.99129	66.48	23.7804	1
4.575	3.52913	13.4	17.6667	-0.15643	-1.47222	83.88	51.1284	1
3.175	1.71474	6.28	22.0433	3.31847	12.2721	40.12	18.2955	1
2.725	1.48804	12.04	4.04	-0.22973	-0.62883	148.84	43.4592	1
1.85	0.886143	18.16	1.64	0.400049	-0.19669	75.36	76.0197	1
2.65	1.5884	18.84	3.05667	-0.61889	-0.54347	122.36	79.9161	1
0.725	0.66844	18	0.833333	0.630976	-0.4656	68.8	75.0904	1
1.05	0.988433	12.92	2.91	0.602523	-0.8685	128.76	47.8472	1
0.75	1.06507	12.64	2.49	-0.64434	-1.31636	162.16	46.4024	1
2.2	1.45808	11.64	2.82333	-0.35964	-1.41194	138.2	41.3895	1

2.225	1.49639	12.72	2.87667	-0.46286	-0.45197	164.56	46.8314	1
2.125	0.841316	12.48	1.01	-0.77516	-0.2971	156.72	45.5039	1
3.4	2.69778	107.56	14.9233	0.122049	-0.90224	135.16	726.018	2
8.2	5.68982	104.36	54.9067	-0.04713	-0.63527	79.08	700.144	2
9	6.52687	112.68	54.81	-0.28019	-1.62681	103	768.376	2
4.825	2.78571	91.12	27.0267	0.323817	-1.00499	116.32	593.368	2
4.65	4.25032	92.4	40	0.804862	-0.20767	117.92	603.65	2
6.575	3.91474	102.84	16.0567	-0.36862	-0.57109	156.92	687.518	2
7.5	3.25768	83	13.4167	-1.04998	0.26343	123	529.242	2
7.5	6.29782	86.2	67.5	0.173455	-1.37146	142.92	554.773	2
6.925	2.60265	88.92	10.91	-0.07897	-0.44693	124.6	575.792	2
6.025	4.41409	95.96	23.7067	-0.27194	-1.27262	148.2	632.007	2
1.1	1.09453	75.76	2.27333	0.042344	-1.47877	120	473.018	2
5.6	3.87995	82.04	22.7067	0.00281	-1.08511	157.8	521.823	2
2.025	1.97464	66.76	8.69	0.225642	-1.62039	92.76	404.716	2
4.25	2.61367	77.08	9.32667	-0.19904	-0.91014	113.48	483.244	2
4.25	2.85044	76.24	14.7733	-0.12935	-1.07971	82.08	476.823	2
5.4	4.01148	86.68	21.31	-0.72305	-0.42943	140.6	558.186	2
4.475	3.11315	77.4	19.25	0.332468	-0.77693	80.28	485.799	2
4.825	4.54535	72.88	25.9433	-0.46338	-1.60206	134.48	451.191	2
2.325	2.45094	69.32	7.81	-0.87741	-0.63697	71.64	423.985	2
5.75	2.99583	75.36	13.3233	-0.95864	-0.52843	131.6	470.049	2
1.075	1.65106	72.48	3.76	-1.25478	0.26237	116.48	447.927	2
5.15	3.0619	71.6	16.9167	0.026906	-0.44736	145.68	441.355	2
1.225	1.01202	68.56	3.00667	0.202408	-1.44836	126.08	418.198	2
1.7	1.38185	77.76	3.52333	-0.53691	-0.53994	59.6	488.439	2
4.775	2.73208	77.6	8.25	-0.74746	-0.20798	100.72	487.246	2
1.95	2.42428	78.4	12.9167	0.648309	-0.90269	137.84	493.467	2
1.65	1.46236	77.76	4.35667	-0.32714	-1.3849	80.88	488.446	2
1.95	1.40259	73.44	2.50667	-0.22719	-1.25665	132.48	455.241	2
8.75	5.15085	71.8	31.6667	-0.27044	-1.2395	137.32	443.021	2
2.175	2.00629	70.92	9.24333	0.141277	-1.63798	154.04	436.115	2
2.35	1.73245	79.88	5.77667	0.895862	0.783384	109.24	504.872	2
2.95	1.92009	77.68	12.6433	0.364905	-1.25034	127.6	487.902	2
3.1	2.48355	74.24	15.5233	0.377633	-0.96379	150.48	461.481	2
0.175	0.657362	72.8	10.25	0.393464	-1.76106	56.56	450.428	2
2.825	1.54925	74.48	3.26	-0.29515	-0.61413	174.4	463.205	2
4.5	1.5411	73.12	3.52667	-0.74599	0.450792	148	452.807	2
0.7	1.03102	73.16	4.05667	0.289642	-1.57768	144.12	453.117	2
5.875	3.38448	67.96	10.8733	-1.15766	0.173649	92.68	413.759	2
1.45	1.27955	72.88	2.61	0.527385	-0.955	173.52	450.966	2

3.45	2.89426	76.88	14.36	-0.01682	-1.26968	138.72	481.747	2
2.15	1.2661	75.04	2.37333	-0.32642	-1.37217	124.16	467.49	2
0.95	1.03296	77.6	2.33333	0.323215	-1.47419	105.28	487.193	2
2.3	1.18406	72.36	4.15667	0.378037	-0.59768	150.68	447.016	2
1.2	1.03053	74.24	2.44	-0.32018	-0.84354	148.16	461.359	2
2.825	2.10909	76.76	12.3567	0.522943	-0.91978	118.36	480.804	2
1.7	1.84201	70.48	5.09333	-0.32986	-1.52643	128.8	432.737	2
1.4	1.68938	76.52	5.34333	-0.38398	-1.51532	126.04	478.893	2
4.375	3.0611	80.32	11.7267	-0.10658	-1.37813	144.48	508.341	2
1.575	1.86984	74.6	6.5	0.706744	-0.69554	93	464.154	2
1.525	1.28518	73.96	2.95667	-0.2241	-1.60094	137.88	459.221	2
0.75	0.810093	72.16	0.89	-1.1603	0.549572	118.64	445.461	2
2.1	2.35701	91.72	10.71	-0.50048	-1.10616	118.2	598.019	2
2.4	2.09189	91.48	6.76	0.008211	-1.37588	152.36	596.078	2
4.375	3.81997	160.56	29.5067	-0.03846	-1.02398	125.92	1176.55	3
4.8	2.73934	120.08	11.7433	-0.57815	-1.0435	74	829.563	3
7.55	4.64187	125.36	34.9067	-0.10414	-0.84037	40.48	873.944	3
6.75	5.12591	124.24	45.1067	-0.22338	-1.10523	57.44	864.589	3
0.475	1.17545	117.28	20.0433	0.876541	-1.02395	134.16	806.278	3
2.15	1.45017	113.12	2.77667	-0.8043	-0.70739	142.16	771.689	3
1.9	0.817313	120.6	1.08333	-0.89395	0.683668	55.8	833.845	3
5.7	2.18197	137.56	5.34	-1.65868	2.37895	96.52	977.242	3
1.75	0.940412	138.96	1.37333	0.37172	0.797922	121.44	989.197	3
4.875	2.80763	145.04	12.54	0.260223	-0.70154	118.08	1041.49	3
1.25	0.607248	138.92	0.493333	-0.59399	0.598963	119.72	988.851	3
4.275	3.22749	136.96	10.9567	-1.11775	-0.38427	90.8	972.145	3
4.575	3.11581	133.8	15.4167	-0.14194	-1.59196	48.44	945.234	3
1.375	1.01973	139.68	2.06	1.3567	1.12598	128.16	995.367	3
2.65	2.3612	142.48	9.76	0.577127	-0.81048	137.12	1019.44	3
0.975	0.695881	136.68	1.56	0.590471	-0.54191	76.84	969.706	3
1.575	1.54988	134.52	3.26	-0.92809	-0.74059	45.64	951.299	3
10.225	8.08992	176	86.4167	0.552398	-0.82994	82.96	1313.2	3
6.925	6.56687	173.88	81.0267	0.915492	-0.41889	83.56	1294.32	3
12.2	6.4557	166	64	-0.52125	-0.19336	112.8	1224.53	3
7.175	7.45455	172.92	76.2433	0.980879	-0.38839	83.96	1285.78	3
10.275	7.18823	181.88	67.5267	0.15689	-1.28179	110.92	1365.6	3
9.075	4.39133	190.32	29.8933	-0.76298	-0.63882	113.44	1441.27	3
6.525	4.78897	186.88	31.11	-0.45878	-1.4877	127.76	1410.31	3
4.85	2.01872	178.32	15.1433	1.28715	2.02897	140.24	1333.59	3
8.3	4.87555	173.92	31.91	-0.48158	-0.91382	122	1294.49	3
11.525	6.82765	178.24	77.2733	0.377836	-0.76438	99.68	1333.12	3

16	11.5477	194.08	198.993	0.044142	-1.54167	113.44	1475.82	3
13.45	10.4906	185.16	172.473	0.437759	-1.13245	135.56	1395.38	3
9.425	9.5866	180.16	152.307	0.742376	-0.96946	143.04	1350.54	3
8.225	8.87464	177.2	169.583	1.04349	-0.50118	146.32	1324.2	3
15.375	9.52341	178.2	181.75	0.526829	-0.58019	134.52	1333.16	3
2.125	3.86066	165.96	67.8733	0.499767	-1.53153	113.48	1224.18	3
3.8	3.13305	162.76	14.7733	-0.0228	-1.38603	85.8	1195.8	3
6.825	4.04182	158.36	21.3233	-0.1141	-1.22918	102.52	1157.24	3
4.95	3.22448	157.2	37.5	1.39084	1.8745	100.16	1147.17	3
15.375	9.52341	178.2	181.75	0.526829	-0.58019	134.52	1333.16	3
4.45	1.69912	112.92	3.32667	-1.27119	1.95622	138.44	770.04	3
1.7	1.78213	117.16	5.55667	-0.31184	-0.32761	112.6	805.196	3
1.3	1.02786	116.72	2.29333	0.458192	-0.60039	129.44	801.519	3
2.025	1.22237	117.72	4.96	0.164911	-0.9776	110.44	809.85	3
4.475	1.64259	119.92	4.41	-0.57266	0.479015	69.52	828.184	3
20.65	9.18384	111.8	108.25	-1.1262	0.287996	110.36	761.473	3
7.05	4.09782	112.8	22.9167	-0.55961	-1.41095	109.68	769.17	3
1.425	0.889558	111.8	1.33333	0.374115	-1.092	89.64	760.782	3
0.5	0.74162	113	1.41667	-0.71167	-1.1265	154.68	770.689	3
0.7	0.901665	113	3.91667	0.526363	-1.34684	105.88	770.704	3

Table 5.2: classification coefficient generated using selected feature of calculated texture by 5x5 window:

Classification Function Coefficients	Class		
	CSF	Gray and White	TUMOR
IDM	65.396	59.654	65.248
IMC2	16.326	22.609	27.512
VARSGLD	3.157	1.748	.216
mean1	.060	.511	.886
variance1	-.173	-.255	-.274
energy1	.111	.123	.102
(Constant)	-33.333	-52.863	-93.203

Table 5.3: classification result (accuracy) generated using selected feature of calculated texture by 5x5 window:

Classification Results		Class	Predicted Group Membership			Total
			CSF	GW	TUMOR	
Original	Count	CSF	50	0	0	50
		GW	0	80	0	80
		TUMOR	0	3	66	69
	%	CSF	100.0	.0	.0	100.0
		GW	.0	100.0	.0	100.0
		TUMOR	.0	4.3	95.7	100.0
a. 98.5% of original grouped cases correctly classified.						

Table 5.4: classification result (accuracy) generated using selected feature of calculated texture by 10x10 window:

Classification Results						
		Class	Predicted Group Membership			Total
			CSF	TUMO	GW	
Original	Count	CSF	75	0	0	75
		TUMO	0	69	1	70
		GW	0	1	79	80
	%	CSF	100.0	.0	.0	100.0
		TUMO	.0	98.6	1.4	100.0
		GW	.0	1.3	98.8	100.0
a. 99.1% of original grouped cases correctly classified.						

Table 5.5: classification coefficient generated using selected feature of calculated texture by 10x10 window:

Classification Function Coefficients			
	Class		
	CSF	TUMO	GW
Sum entropy	20.846	2.543	7.939
mean1	14.667	47.996	43.363
energy1	.422	.503	.565
entropy1	-1.754	-5.567	-5.064
(Constant)	-114.902	-602.564	-501.084
Fisher's linear discriminant functions			

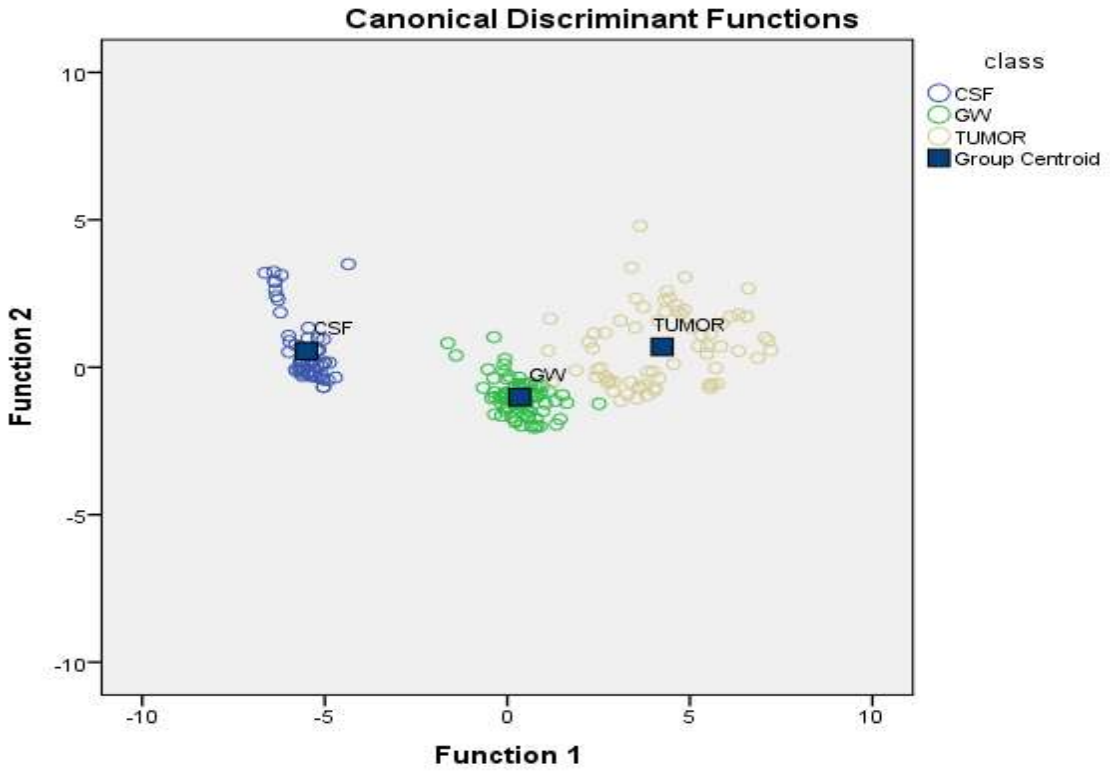

Fig. 5.1: Classification map generated by using of selected texture from 15x15 window size

Table (5.6) Classification result and accuracy of 20x20 window size

Classification Results						
		class	Predicted Group Membership			Total
			CSF	GW	TUMOR	
Original	Count	CSF	60	0	0	60
		GW	0	80	0	80
		TUMOR	0	4	66	70
	%	CSF	100.0	.0	.0	100.0
		GW	.0	100.0	.0	100.0
		TUMOR	.0	5.7	94.3	100.0
a. 98.1% of original grouped cases correctly classified.						
b. Cross validation is done only for those cases in the analysis. In cross validation, each case is classified by the functions derived from all cases other than that case.						
c. 98.1% of cross-validated grouped cases correctly classified.						

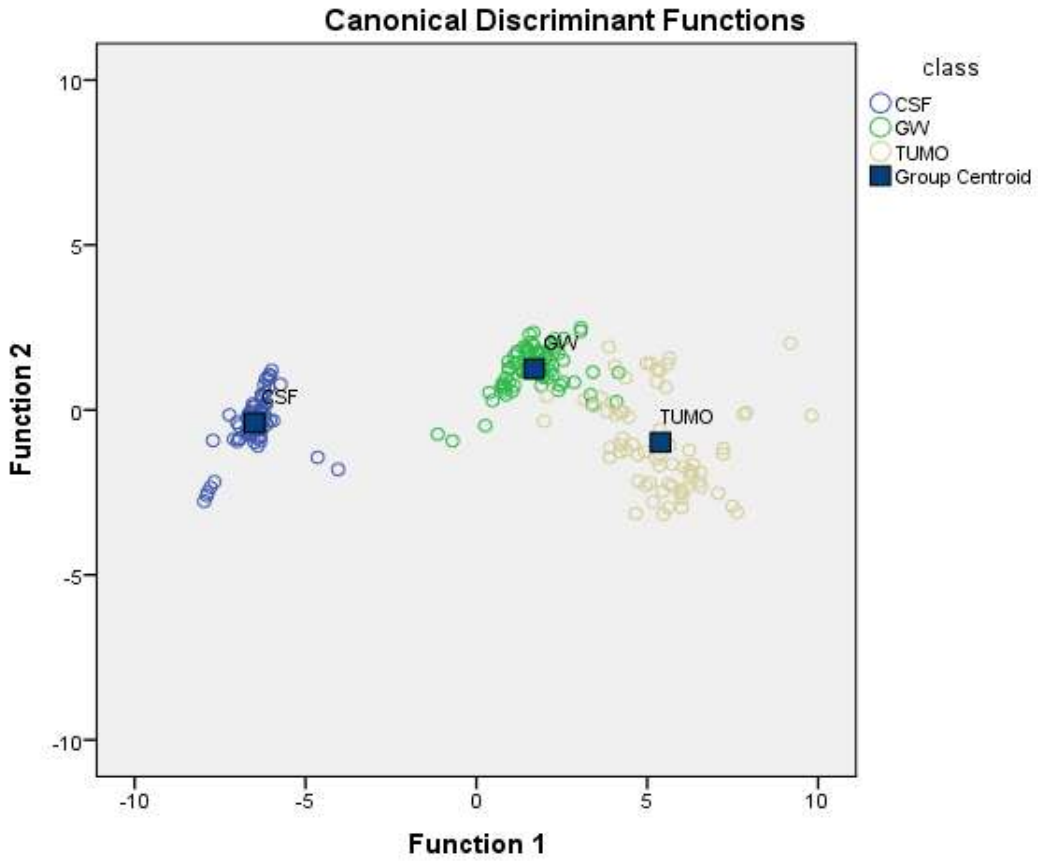

Fig. 5.2: Classification map generated by using of selected texture from 20x20 window size

Table (5.7) Classification result and accuracy of 20x20 window size

Classification Result						
		class	Predicted Group Membership			Total
			CSF	GW	TUMO	
Original	Count	CSF	79	0	0	79
		GW	0	78	2	80
		TUMO	0	7	63	70
	%	CSF	100.0	.0	.0	100.0
		GW	.0	97.5	2.5	100.0
		TUMO	.0	10.0	90.0	100.0
a. 96.1% of original grouped cases correctly classified.						

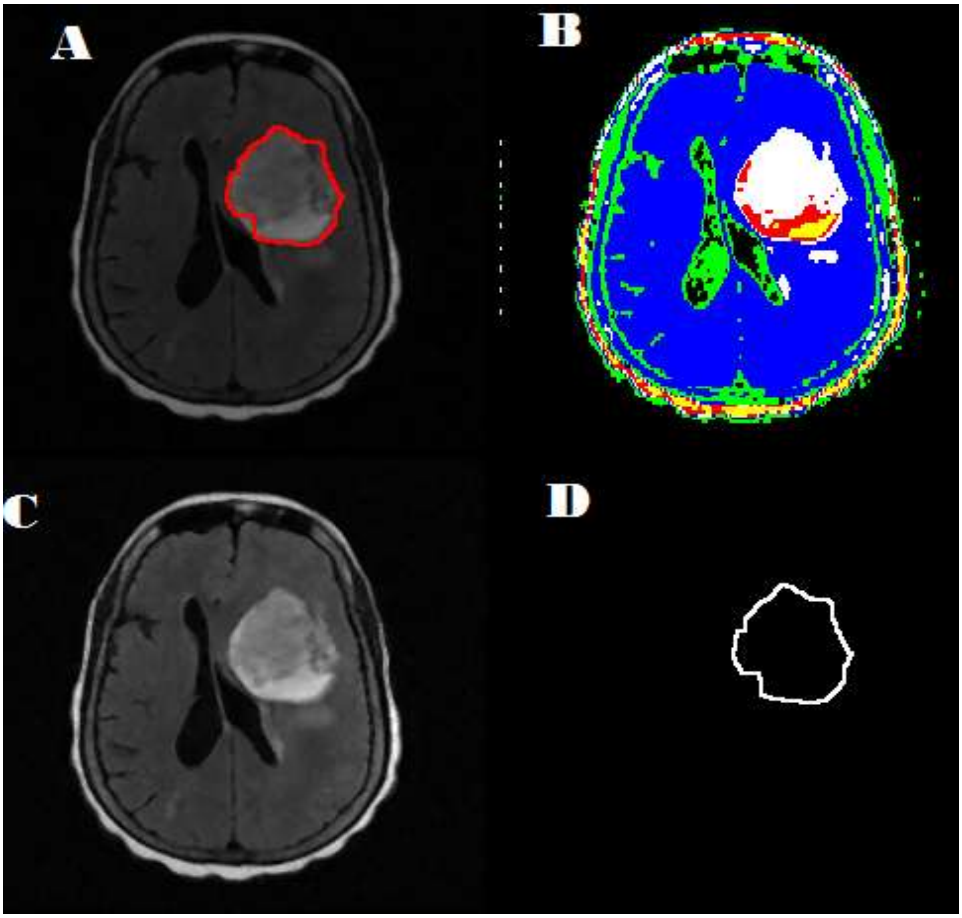

Fig. 5.3. Demonstrate a heterogeneous brain mass [A] GTV definition based on tumor intensity profile, [B] Classification map based on intensity of brain tissue, [C] the original FLAIR image, [D] tumor margin drown by algorithm generated IDL program that can be used as radiotherapy GTV.

Appendix (B)

Published Paper Attached Here: